March 2016

Applications in Low-Power Phased Array Weather Radars

Robert A. Palumbo Jr
University of Massachusetts Amherst

APPLICATIONS IN LOW-POWER PHASED ARRAY WEATHER RADARS

A Dissertation Presented

by

ROBERT A. PALUMBO

Submitted to the Graduate School of the
University of Massachusetts Amherst in partial fulfillment
of the requirements for the degree of

DOCTOR OF PHILOSOPHY

February 2016

Electrical and Computer Engineering

APPLICATIONS IN LOW-POWER PHASED ARRAY WEATHER RADARS

A Dissertation Presented

by

ROBERT A. PALUMBO

Approved as to style and content by:

Stephen J. Frasier, Chair

Paul Siqueira, Member

Michael Zink, Member

Gopal Narayanan, Member

Christopher V. Hollot, Department Head
Electrical and Computer Engineering

DEDICATION

This is dedicated to my family, who has stuck by me for so long. And to Mikey, who is one of the few friends who hasn't given up on me.

Two roads diverged in a wood, and I took the one less traveled by, and that has made all the difference

—Robert Frost

ACKNOWLEDGMENTS

First and foremost, I'd like to thank Raytheon for giving me the opportunity to work with a radar system for so long as I have. It's a luxury that's not often afforded in large companies, and I'm grateful to have been given the chance to prove myself. I'm very thankful to both Paul Ferraro and Christopher McCarroll from Raytheon, who got me started on my graduate career in Amherst and have done everything possible to keep me going. I'd also like to thank Ilene Hill and everyone in SRSI/SVTAD at Raytheon for being patient with me through my endeavors.

The radar system wouldn't nearly be this capable if it weren't for the efforts of Ken Wood from Raytheon and Eric Knapp from the University of Massachusetts at Amherst. Thanks for the long days we spent trying to build and calibrate the first system and the months trying to commercialize and sell it internationally. I'd also like to thank the rest of the staff and students at the Microwave Remote Sensing Laboratory (MIRSL), who have provided a great learning environment with all the lab equipment and tools needed to get the job done. And special thanks to my advisor, Steve Frasier, for taking me on as a student and keeping me through the sometimes long months without contact.

I appreciate all the support and effort from the engineers at FIRST RF Corporation (Boulder, CO), specifically Luke Sankey, who have built an extremely capable, affordable, and commercialized phased array system.

Thanks to Professor Douglas Gray and Waddah Al-Ashwal from the University of Adelaide (South Australia, AU), for the whirlwind of field experiments and trips we made in such a short time in Australia. That was one of the culminating experiences of my graduate career, and I'm grateful for all the help.

Last, but not least, thanks to Richard Moro, Terry Kirn, and David Payne from AT and SED in Raytheon, who have done a great job in educating me in the finer points of radar program capture and marketing. It's an often overlooked and under-appreciated task, but I'm grateful to be a part of it (and look forward to more future wins).

ABSTRACT

APPLICATIONS IN LOW-POWER PHASED ARRAY WEATHER RADARS

FEBRUARY 2016

ROBERT A. PALUMBO

B.Sc., RENSSELAER POLYTECHNIC INSTITUTE

M.Sc., UNIVERSITY OF MASSACHUSETTS AMHERST

Ph.D., UNIVERSITY OF MASSACHUSETTS AMHERST

Directed by: Professor Stephen J. Frasier

Low-cost X-band radars are an emerging technology that offer significant advantages over traditional systems for weather remote sensing applications. X-band radars provide enhanced angular resolution at a fraction of the aperture size compared to larger, lower frequency systems. Because of their low cost and small form factor, these radars can now be integrated into more research and commercial applications. This work presents research and development activities using a low-cost, X-band (9410 MHz) Phase-Tilt Radar. The *phase-tilt* design is a novel phased array architecture that allows for rapid electronic scanning in azimuth and mechanical tilting in elevation, as a compromise between cost and performance.

This work focuses on field studies and experiments in three meteorological applications. The first stage of research focuses on the real-world application of phased array radars in forest fire monitoring and observation. From April to May 2013, a

phase-tilt radar was deployed to South Australia and underwent a field campaign to make polarimetric observations of prescribed burns within and around the Adelaide Hills region. Measurements show the real-time evolution of the smoke plume dynamics at a spatial and temporal resolution that has never before been observed with an X-band radar. This dissertation will perform data analysis on results from this field campaign. Results are compared against existing work, theories, and approaches.

In the second stage of research, field experiments are performed to assess the data quality of X-band phased array radars. Specifically, this research focuses on the measurement of and techniques to improve the variance of weather product estimators for dual-polarized systems. Variability in the radar products is a complicated relationship between the radar system specifications, scanning strategy, and the physics governing precipitation. Here, the variance of the radar product estimators is measured using standard radar scanning strategies employed in traditional mechanical antenna systems. Results are compared against adaptive scan strategies such as beam multiplexing and frequency diversity. This work investigates the improvement that complex scanning strategies offer in dual-polarized, X-band phased array radar systems.

In the third stage of research, simulations and field experiments are conducted to investigate the performance benefits of adaptive scanning to optimize the data quality of radar returns. This research focuses on the development and implementation of a waveform agile and adaptive scanning strategy to improve the quality of weather product estimators. Active phased array radars allow radar systems to quickly vary both scan pointing angles and waveform parameters in response to real-time observations of the atmosphere. As an evolution of the previous research effort, this work develops techniques to adaptively change the scan pointing angles, transmit and matched filter waveform parameters to achieve a desired level of data quality. Strategies and techniques are developed to minimize the error between observed and

desired data quality measures. Simulation and field experiments are performed to assess the quality of the developed strategies.

PREFACE

After all I've experienced, through all the meetings and gate reviews. All the late nights and plane flights to conferences and trade shows. Spending hours pouring over software code looking for that one bug, or analyzing and re-analyzing data to unravel some artifact. Writing white papers and bids and proposals, and giving demonstrations or walkthroughs. Volunteering for museum visits and side projects in what little free time there was. After pushing through late nights, long road trips to short field tests, and early morning international conference calls. After traveling thousands of miles Down Under observing birds, bushfires, planes, waves, rain, and ships. Through dozens of talks to crowds of tens to hundreds. Through success and failure, good times and bad, little victories and huge failures. From array analysis to receiver development to system integration and test to (so much) software development, and the always-exciting Ts and Cs and licensing issues. Through all this and more, I've learned one immutable, resolute fact: this is what I was destined to do with my life.

This dissertation is the culmination of the experiences I've undertaken over the past few years, in trying to build an idea into reality. I've always been more of a engineer than a research scientist, so the context of much of this work is towards the practical application of phased array radar system design and analysis. In short, this work summarizes the collaborative efforts of Raytheon Company and the University of Massachusetts Amherst to build a commercialized phased array weather radar. The focus of this work is almost entirely on radar backend design and signal processing algorithm development, specifically from the Digital Receiver/Exciter (DREX) to the radar software package. Wherever possible and permissible, I've tried to either

derive the equations explicitly or describe the algorithm in detail for most of the algorithms here. This is as much for my benefit as yours; that re-stating a complicated algorithm in another (equivalent) way might somehow get the concept across better for some readers than others. As always though, I recommend falling back on the cited references for all standard algorithms, or contacting me directly for questions on the novel ones proposed here.

TABLE OF CONTENTS

LIST OF TABLES

Table **Page**

LIST OF FIGURES

Figure **Page**

LIST OF ABBREVIATIONS

ADAPTS	Adaptive DSP Algorithm for Phased-Array Radar Timely Scans
ADC	Analog/Digital Converter
AGL	Above Ground Level
ARSR	Air Route Surveillance Radar
ASL	Above Sea Level
ASR	Airport Surveillance Radar
ATAR	Alternate Transmit/Alternate Receive
AWC	Adaptive Waveform Control
AWGN	Additive White Gaussian Noise
BDM	Bushfire Detection and Monitoring
BLOS	Beyond Line-Of-Sight
BMX	Beam Multiplexing
CASA	Collaborative Adaptive Sensing of the Atmosphere
CentOS	Community Enterprise Operating System
CFAR	Constant False Alarm Rate
CFS	South Australian County Fire Services
CIC	Cascaded Integrator-Comb
CORDIC	COordinate Rotation DIgital Computer
COTS	Commercial Off-The-Shelf
CP	Conservation Park
CPI	Coherent Processing Interval
CPS	Contiguous Pair Sampling
CUT	Cell-Under-Test
CW	Continuous Wave

DAC	Digital/Analog Converter
DBF	Digital Beam Forming
DCAS	Distributed Collaborative Adaptive Sensing
DDC	Digital Down-Converter
DEWNR	Australian Department of Environmental, Water and Natural Resource
DFT	Discrete Fourier Transform
DFW	Dallas Fort-Worth
DHS	Department of Homeland Security
DoD	Department of Defense
DREX	Digital Receiver/Exciter
DSP	Digital Signal Processing
DUC	Digital Up-Converter
ECEF	Earth-Centered, Earth-Fixed
EIRP	Effective Isotropic Radiated Power
ENU	East-North-Up
FAA	Federal Aviation Administration
FFT	Fast Fourier Transform
FIFO	First-In, First-Out
FIR	Finite Impulse Response
FMX	Frequency Multiplexing
ForestrySA	South Australian Forestry Corporation
FPGA	Field Programmable Gate Array
FSM	Finite State Machine
GCC	GNU Compiler Collection
GMAP	Gaussian Model Adaptive Processing
GPIO	General Purpose Input/Output
GPL	GNU General Purpose License
HCA	Hydrometeor Classification Algorithm
HDD	Hard Disk Drive

HTML	Hyper Text Markup Language
ICPR	Integrated Cross Polarization Ratio
IEEE	Institute of Electrical and Electronics Engineers
IF	Intermediate Frequency
IP	Intellectual Property
IP1	Integrated Project-1
IPS	Independent Pair Sampling
IQ	In-phase and Quadrature
IR	Infra-Red
LFM	Linear Frequency Modulated
LLA	Latitude-Longitude-Height
LPAR	Low-power Phased Array Radar
LPR	Low-power Radar
LRU	Line Replaceable Unit
LUT	Look-Up Table
MAE	Mount Azimuth/Elevation
MAP	Mission Application Processor
MAUT	Multi-Attribute Utility Theory
MCMF	Mount-Centered, Mount-Fixed
MDS	Minimum Detectable Signal
MPAR	Multifunction Phased Array Radar
NCTCG	North Central Texas Council of Governments
NetCDF	Network Common Data Format
NEXRAD	Next-Generation Radar
NOAA	National Oceanic and Atmospheric Administration
NRC	National Research Council
NSF	National Science Foundation
NSWRC	NextGen Surveillance and Weather Radar Capability
NWRT	National Weather Radar Testbed
NWS	National Weather Service

PC	Pulse Compression
PHP	Hypertext Preprocessor
PLFM	Piecewise-Linear Frequency Modulated
PNG	Portable Network Graphics
PPI	Planned Position Indicator
PRF	Pulse Repetition Frequency
PRI	Pulse Repetition Interval
PRT	Pulse Repetition Time
PSD	Power Spectral Density
PTWR	Phase-Tilt Weather Radar
QPE	Quantitative Precipitation Estimation
QPF	Quantitative Precipitation Forecasting
RAE	Radar Azimuth/Elevation
RAM	Random Access Memory
RAR	Radar Action Request
RCRF	Radar-Centered, Radar-Fixed
RCS	Radar Cross Section
RF	Radio Frequency
RHEL	Red Hat Enterprise Linux
RHI	Range-Height Indicator
RMS	Root Mean Square
rOS	Radar Operating System
SCIT	Storm Cell Identification and Tracking
SDR	Software-Defined Radio
SFDR	Spurious-Free Dynamic Range
SMA	Subminiature Version-A
SNR	Signal to Noise Ratio
SQL	Structured Query Language
SSD	Solid State Drive
SSE	Streaming Single-instruction, multiple data Extension

STSR	Simultaneous Transmit/Simultaneous Receive
sUAS	Small Unmanned Aircraft System
T/R	Transmit/Receive
TDWR	Terminal Doppler Weather Radar
UAS	Unmanned Aircraft System
UAV	Unmanned Aerial Vehicle
UDP	User Datagram Protocol
USB	Universal Serial Bus
USRP	Universal Software Radio Peripheral
UTC	Coordinated Universal Time
WSR-88D	Weather Surveillance Radar
XML	Extensible Markup Language

LIST OF SYMBOLS

(A_m, E_m)	Pedestal Mount Azimuth and Elevation Pointing Angles (deg)
arg	Complex Argument
c	Speed of Light in a Vacuum ($299\,792\,458\,\mathrm{m\,s^{-1}}$)
CPA	Clutter Phase Alignment
$\Delta\Phi_s(\theta, \phi)$	System Differential Phase Offset (deg)
$\Delta Z_{dr}(\theta, \phi)$	System Differential Reflectivity Bias (dB)
exp	Natural Exponential Function (e^x)
G_c	Pulse Compression Gain (dB, $\approx \tau/\tau_c$)
G_r	Array Receive Gain (dBi)
G_t	Array Transmit (dBi)
h	height (AGL, m)
k	Boltzmann Constant ($1.38\text{E}{-23}\,\mathrm{W\,s\,K^{-1}}$)
K_{DP}	Specific Differential Phase (deg/km)
K_w	Dielectric Factor of Water ($\lvert K_w\rvert^2 \approx 0.9$)
λ	Radar Wavelength (m)
l_f	System Noise Figure (dB)
ln	Natural Logarithm
$\log_{10}$	Base-10 Logarithm
M	Number of (Incoherently) Integrated Pulses
$\mathrm{MR}_{m,n}$	Median-Range Texture Field (dBZ)
NCP	Normalized Coherent Power (dB)
N_p	Noise Power (dB)
P_d	Probability of Detection
P_{fa}	Probability of False Alarm
P_{fire}	Probability of Fire

p^s_{fire}	Single-Scan Probability of Fire
Φ_{DP}	Differential Phase (deg)
Φ_{DS}	Backscatter Differential Phase (deg)
P_t	Peak Transmit Power (W)
r	Range (m)
r_d	Down Range (m)
R^n_{hh}	H-pol. Lag-n Copolar Correlation (W)
R^n_{hv}	H/V-pol. Lag-n Cross-polar Correlation (W)
R^n_{vh}	V/H-pol. Lag-n Cross-polar Correlation (W)
R^n_{vv}	V-pol. Lag-n Copolar Correlation (W)
ρ_{hv}	Copolar Correlation Coefficient
$\lfloor \cdot \rfloor$	Round Towards Negative Infinity
$\lceil \cdot \rceil$	Round Towards Positive Infinity
$SD(\cdot)$	Standard Deviation
$\mathrm{SD}(\Phi_{DP})$	Texture of Differential Phase (deg)
$\mathrm{SD}(Z_h)$	Texture of Reflectivity (dBZ)
$\mathrm{SD}(Z_{dr})$	Texture of Differential Reflectivity (dB)
sgn	Signum function
S_h	H-pol. Noise-Removed Power (W)
S_v	V-pol. Noise-Removed Power (W)
$\mathrm{SPIN}_{m,n}$	SPIN Value
SQI	Signal Quality Index (dB)
T	Absolute Temperature (K)
τ	Waveform (Uncompressed) Pulsewidth (µs)
τ_c	Waveform (Compressed) Pulsewidth (µs)
$\mathrm{TDBZ}_{m,n}$	Spatial Texture of Reflectivity (dBZ)
(θ, ϕ)	Radar-local Azimuth and Elevation Pointing Angles (deg, rel. to array boresight)
THR	SNR Threshold Level (dB)
T_s	Pulse Repetition Time (s)

v	Radial Velocity ($\mathrm{m\,s^{-1}}$)
v_a	Unambiguous Velocity ($\mathrm{m\,s^{-1}}$)
v_p	Radial Velocity from Differential Phase ($\mathrm{m\,s^{-1}}$)
σ_v	Spectral Width ($\mathrm{m\,s^{-1}}$)
σ_{vn}	Normalized Spectral Width ($= 2\sigma_v T_s/\lambda$)
Z_{dr}	Differential Reflectivity (dB)
Z_e	Equivalent Reflectivity factor (dBZ)
Z_h	H-pol. Reflectivity (dBZ)
Z_v	V-pol. Reflectivity (dBZ)

CHAPTER 1

INTRODUCTION

Operational civil infrastructure radars deployed around the world today are physically large, high-power, mechanically-rotating systems. Designed for long-range (hundreds of kilometers) coverage through heavy precipitation, these radars must operate at radar wavelengths not subject to substantial attenuation. This necessitates the use of large antennae to achieve the narrow beam width needed for kilometer-scale spatial resolution throughout the coverage region. The radars use high-power transmitters to meet minimum sensitivity requirements and large mechanically scanned antennae that require dedicated land, towers, and other support infrastructure. The large physical size of these systems combined with potential environmental impacts limits the availability of potential sites. The strategy for deploying national radar networks such as this is to judiciously attempt to site radars where low-altitude coverage is most needed, while simultaneously minimizing the number of radars in the network as a means of controlling the life cycle costs of the overall system. The resulting infrastructure provides good coverage aloft and some coverage close to the ground in specific regions, while leaving large expanses below 2 km to 3 km altitude without radar coverage.

While this concept of operations is sufficient for contiguous coverage over a large area, the lack of low-altitude surveillance results in a number of practical issues. Certain weather phenomena, such as hurricanes, supercells, mesocyclones, tornadoes, microbursts, and snow, often build and evolve at low altitudes below 1 km [80]. As the current infrastructure cannot directly observe these phenomena, this results in de-

graded performance in tornado early warning systems and deficiencies in severe storm emergency preparedness [73]. In addition, the recent growth in affordable Unmanned Aerial Vehicles (UAVs) (also known as *drones*) for both personal and commercial use has led to a re-evaluation of the scope and extent of the national airspace. While current regulations limit UAVs to altitudes below 500 ft and prevent Beyond Line-Of-Sight (BLOS) operation [67], many companies are pushing for widespread deployment for a variety of applications from package delivery to emergency and hydrologic monitoring [34, 36]. Recently, several companies have proposed the use of dividing the lower atmosphere into dedicated traffic zones for Unmanned Aircraft Systems (UASs) and Small Unmanned Aircraft Systems (sUASs), combined with cooperative target surveillance systems [3, 50]. While such systems may be a possible far-term solution, they do not address the issue of non-cooperative target recognition. They also do not address the need for localized weather forecasting in UAS traffic lanes.

The past decade has seen a great influx in new technology designed to combat this low-altitude *coverage gap*. Since its inception in 2002, the goal of the National Science Foundation (NSF) Engineering Research Center for the Collaborative Adaptive Sensing of the Atmosphere (CASA) is to investigate and develop technologies for improving low-altitude weather forecasting. CASA has been the forerunner for the development of a network of small-scale radars to combat this coverage gap issue. In particular, the focus in the past few years has been towards the integration of phased array technology into the small-scale radar network design methodology. Small phased array antennae are a desirable technology for such an application because they permit flexible beam positioning, have lower recurring costs than mechanical antennae, and can be installed on the sides of existing towers and rooftops.

This research is an evolution of this work and focuses on the applications of phased array radars for meteorological and hazard detection and observation. While these applications have been studied and investigated with traditional mechanical radar

systems, little research has been performed using phased array technology. The objectives of this research are to investigate the data quality of X-band phased array radars and assess their performance in several real-world applications.

1.1 Existing US Operational Weather Radars

Before investigating and researching a new weather radar technology, it is important to review the current system to provide an adequate baseline. Primary weather surveillance in the US is served by a network of over 160 Weather Surveillance Radars (WSR-88Ds), commonly known as the Next-Generation Radar (NEXRAD). Each WSR-88D [37] is an S-band (2700 MHz to 3000 MHz) center-fed, parabolic dish, mechanically-steered radar. At a diameter of 8.5 m, the radar outputs a peak transmit power of 475 kW. Each radar in the network operates independently and is manually placed in different radar modes of operation to observe different precipitation types, from clear air to precipitation and severe weather. The refresh rate, or time to complete each volume scan, varies by radar mode from 5 min (precipitation) to 10 min (clear air and snowfall). The system uses either a short (1.57 µs) or long pulse (4.57 µs), and a Pulse Repetition Frequency (PRF) from 320 Hz to 1300 Hz. See [37, p. 47] for a more detailed description of the radar system technical and performance specifications.

In addition to the NEXRAD network, the Terminal Doppler Weather Radar (TDWR) [7] was established in the early 1990s to provide higher quality weather and airport surveillance near major airports in the United States. Operating at C-band (5600 MHz to 5650 MHz), each TDWR system operates at twice the range resolution of NEXRAD at an update rate of 1 min.

1.2 Motivation

The weather surveillance mission in the United States has seen great improvements since the deployment of the NEXRAD network. With the recent upgrade to dual-polarization [120], the system has lead to advancements in both Quantitative Precipitation Estimation (QPE) and Quantitative Precipitation Forecasting (QPF). With these advancements, however, must come goals for future capability systems. The National Research Council (NRC) has previously reported [80] that there is a need for atmospheric monitoring beyond our current capabilities, specifically noting the need for Distributed Collaborative Adaptive Sensing (DCAS) for the integration and cooperation of multiple-sensor networks. In a 2002 report on the next generation weather technology [30], it was recommended that augmented infrastructure or specialized surveillance is required in areas such as complex terrain, urban, or coastal regions. The same report emphasized the development of phased arrays to provide rapid scanning and to allow for adaptive waveform and scan pattern selection. More recently, the US Committee on Commerce, Science, and Transportation proposed a bill to Congress, known as the Weather Research and Forecasting Innovation Act [95]. If signed into law, the bill would invest in technologies to advance observing and forecasting capabilities and provide commercial opportunities for weather data processing and systems.

The current weather and airport surveillance missions within the United States are currently split among several distinct radar systems across multiple frequency bands; the Airport Surveillance Radar (ASR, S-band) for aircraft surveillance and monitoring [111], the Terminal Doppler Weather Radar (TDWR, C-band) for detecting wind shear and gust fronts near airports [7], the Next-Generation Radar (NEXRAD, S-band) for primary weather observations and hazard monitoring [59], and the Air Route Surveillance Radar (ARSR, L-band) [115]. In 2012, the Federal Aviation Administration (FAA) and the National Oceanic and Atmospheric Administration

(NOAA) began solicitations for research into replacing these aging and antiquated systems with a single, multi-function phased array radar. Known as the NextGen Surveillance and Weather Radar Capability (NSWRC), research began on the initial requirements that a phased array radar would need to meet to enhance or replace the current systems. A phased array radar would have to support the aircraft surveillance and airport surveillance missions, while simultaneously interrogating the atmosphere for severe weather, including wind shear, gust fronts, severe thunderstorms, and QPE [110, 38]. Table 1.1 lists the set of notional requirements put forth by the NSWRC that a future capability system would need.

These requirements highlight several key technical challenges for future systems. Small data bias places stringent requirements on initial system calibration and built-in test and recalibration in the field. Migrating to phased array radars is even more difficult, since calibration constants are required at every beam position, and re-calibration must be performed at multiple beam positions. Meeting these data quality requirements must be considered in early system integration and test planning, since calibration and characterization efforts often represent a significant portion of the cost of a phased array system.

1.3 Dissertation Structure

This dissertation is organized as follows. Chapter 1 presents an overview of the background, problem statement, and motivation for this research, as well as a brief description of the current operational solutions. Chapter 2 describes the system and components of the X-band phased array radar developed and deployed for this

[1]Here, Δ_{max} and σ_{max} denote the requirements on bias and standard deviation, respectively, for each of the listed weather products. Maximum bias and standard deviation depend on the measured Signal to Noise Ratio (SNR), copolar correlation coefficient (ρ_{hv}), and spectral width (σ_v). Blank cells denote requirements which do not depend on the measured parameter.

Table 1.1: Multifunction Phased Array Radar (MPAR) notional requirements for weather observation[1]. Note that differential reflectivity (Z_{dr}), copolar correlation coefficient (ρ_{hv}), and differential phase (Φ_{DP}) are only specified at true elevation angles (ϕ) lower than 20°. These requirements are in the context of the S-band radars currently operated by the National Weather Service (NWS).

Product	σ_{max}				Δ_{max}			
		SNR (dB)	σ_v ($\mathrm{m\,s^{-1}}$)	ρ_{hv}		SNR (dB)	σ_v ($\mathrm{m\,s^{-1}}$)	ρ_{hv}
Reflectivity (Z_h)	1.8 dBZ	10	4		1.0 dBZ			
Radial Velocity (v)	$1\,\mathrm{m\,s^{-1}}$	8	4		$0\,\mathrm{m\,s^{-1}}$			
Spectral Width (σ_v)	$1\,\mathrm{m\,s^{-1}}$	10	4		$0.2\,\mathrm{m\,s^{-1}}$	10	12	
Differential Reflectivity (Z_{dr})	0.3 dB, $\phi < 20°$	20	2	0.99	0.1 dB ($Z_{dr} < 1$ dB), else $0.1 Z_{dr}$			
Copolar Corr. Coefficient (ρ_{hv})	6E−3, $\phi < 20°$	20	2	0.99	1E−3	20	2	0.99
Differential Phase (Φ_{DP})	2.5°, $\phi < 20°$	20	2	0.99	0°			
Signal to Noise Ratio (SNR)	2.0 dB	0	4		1.0 dB			

research. In Chapter 3, the radar signal processing algorithms used to generate the weather products are derived and presented.

The results of proposed research into novel applications and field work are presented in Chapters 4 to 6. Chapter 4 presents research and analysis on the use of X-band phased array radars for Bushfire Detection and Monitoring (BDM). This chapter analyzes the results of a field campaign performed in South Australia from April to May 2013. During this campaign, an X-band phased array radar made polarimetric observations on the backscattered radar echoes from several controlled and uncontrolled forest fires. Based on the data, an algorithm is proposed which uses fuzzy logic and storm cell tracking techniques to identify smoke plume echoes and characterize the likelihood that areas in the plume are located above active fire sources.

Chapter 5 presents a comparative analysis of traditional versus complex phased array scanning strategies. The complex scanning strategies are designed to make use of the electronic and rapid scanning capabilities of phased array radars to improve data quality. Building on these results, Chapter 6 describes a novel scanning algorithm

designed specifically for phased array radars that uses waveform agility to optimize the scan time to achieve a desired level of data quality. Chapter 7 summarizes the research to be performed and presents concluding remarks.

CHAPTER 2

SYSTEM DESCRIPTION

2.1 Historical Overview

Since its inception, the National Science Foundation (NSF) Engineering Research Center for the Collaborative Adaptive Sensing of the Atmosphere (CASA) has advocated for the deployment of distributed networks of low-cost, small-scale X-band radars to improve the weather forecasting in the lower atmosphere, where current operational radars cannot observe due to the curvature of the Earth and terrain blockage [74]. By using small-scale ($1\,m^2$, 10 W to 100 W peak power), coherent-on-receive, X-band (9300 MHz to 9500 MHz) radars, the systems can be more easily deployed in urban areas and inhospitable terrain. In addition, smart scanning techniques can be used to adaptively control where the radar network scans to improve the refresh rate and situational awareness of the network over the current operational infrastructure.

As a proof-of-concept, in 2006 CASA implemented and deployed a 4-radar network of X-band, magnetron-transmitter mechanical radars in Southwestern Oklahoma. Known as the Integrated Project-1 (IP1) network, the goal of the testbed was to evaluate the concept of Distributed Collaborative Adaptive Sensing (DCAS) using small-scale X-band radars [19, 20]. Comparison of data between the CASA IP1 testbed and the nearby Weather Surveillance Radars (WSR-88Ds) in Frederick (KFDR) and Twin Lakes (KTLX) show that the testbed provided increased resolution on supercell mesocyclones and provided higher quality data to forecasters, consistent with current operational storm prediction models [17]. Furthermore, an analysis of re-

sults from the system demonstrated that the network could provide high quality radar returns and improved resolution and tracking of mesoscale weather events [22, 21].

As an evolution of the IP1 network and continuation of the NSF research center, CASA and the North Central Texas Council of Governments (NCTCG) began a 5-year project in 2012 to deploy an 8-radar node in the Dallas Fort-Worth (DFW) area [92]. The goals of the project are to provide high-resolution mapping of atmospheric conditions, support neighborhood-scale warnings for flash floods and other high-impact weather events, and demonstrate the value of distributed, collaborative-adaptive X-band radar networks to the National Weather Service (NWS). The project aims to demonstrate the capability of such networks to support urban flash flood monitoring by providing high-resolution rainfall mapping through algorithms for X-band Quantitative Precipitation Estimation (QPE) [25, 26].

In parallel to the IP1 network development, in 2007 CASA began development of an electronically-scanned phased array radar envisioned to become the next-generation radar technology for use in X-band radar networks. Known as the *phase-tilt* architecture, the radar antenna electronically scans in the azimuthal direction and mechanically tilts in elevation [101, 56]. The lab prototype antenna developed out of the University of Massachusetts Amherst (Amherst, MA) was a dual-polarized, linear phased array using solid-state Transmit/Receive (T/R) modules and four Line Replaceable Units (LRUs). Each LRU contained 18 center-fed columns of 32 dual-polarized patch-array elements, which allowed the system to scan electronically in the azimuthal direction from -45° to 45° off boresight. From 2009 to 2013, another iteration of this prototype, weatherized for field testing, was calibrated and participated in field testing in and around Western Massachusetts at the University of Massachusetts Amherst [82, 83]. In 2014, this system was deployed to the DFW area to participate in a field study in conjunction with the CASA-NCTCG radar network [81].

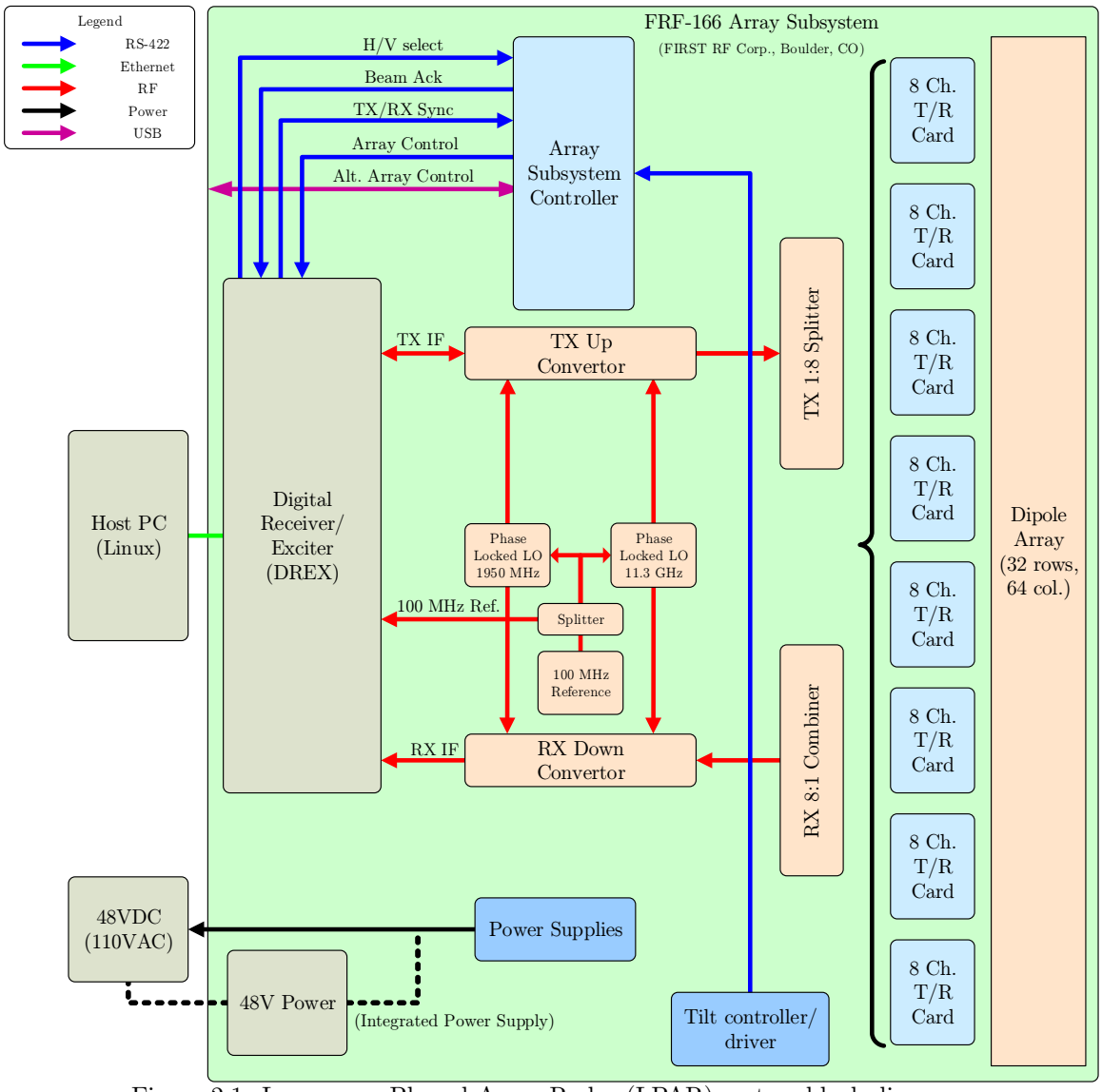

Figure 2.1: Low-power Phased Array Radar (LPAR) system block diagram.

As development of the phase-tilt prototype system progressed, Raytheon Company began development in 2011 of a commercialized phase-tilt radar system, suitable for long-term field study and evaluation. The array front-end, from the frequency converter to the array elements, was designed and built by FIRST RF Corporation (Boulder, Colorado) [102], and the backend was developed at the University of Massachusetts Amherst [85]. The first version of this system (denoted *REV1*) underwent field testing and calibration at the University of Massachusetts in 2012 [84]. From

January to June 2013, the system deployed to South Australia in cooperation with the University of Adelaide (South Australia, AU) to perform field measurements of forest fires and other natural phenomena [86, 87]. Following a 12-month deployment from December 2013 at a Raytheon facility (Portsmouth, RI) overlooking the Narragansett Bay, this system is currently being setup at the University of Massachusetts Lowell (Lowell, MA). In 2012, a second version of this system (*REV2*) was developed and deployed at the University of Massachusetts Amherst.

While the phase-tilt architecture is a simplified, low-cost system suitable for university-driven development and research, any multi-mission capable system for both volumetric weather observation, hazard monitoring, and target surveillance requires a full 2D phased array to meet top-level requirements for simultaneous weather, airport, and aircraft surveillance [38]. To that end, since 2012 Raytheon Company has been developing a 2D phased array radar for weather and target surveillance. The system has successfully performed in demonstrations for wind turbine mitigation, weather radar/urban meteorology, and precision approach applications [57]. Additional revisions of the systems are currently being tested in and around New England.

2.2 System Overview

As mentioned previously, there are two versions of the phase-tilt radar system currently operational, REV1 and REV2. The system overview presented in this section applies to both systems, since the performance and system architecture is similar. Formerly known as the Phase-Tilt Weather Radar (PTWR), the LPAR is a commercialized phased array combined with an integrated Digital Receiver/Exciter (DREX) and software suite. The system is comprised of three main components: the array, the DREX, and the software suite. System parameters for the LPAR are shown in Table 2.1. A block diagram of the system is shown in Figure 2.1.

Table 2.1: LPAR system parameters.

Parameter	Units	Value
Center Frequency	MHz	9410
Transmit Power (Peak)	W	70
Pulsewidth	µs	0.5 to 55
Pulse Compression Gain	dB	Up to 21
Duty Cycle (max)		30 %
Unambiguous range @ Max PRF	km	31
Unambiguous Velocity @ Single PRF	$\mathrm{m\,s^{-1}}$	Up to 38
Unambiguous Velocity @ Dual PRF	$\mathrm{m\,s^{-1}}$	57 (@ 2:3)
Sensitivity @ 35 km	dBZ	16
Elevation Beamwidth	deg	2.8
Azimuth Beamwidth	deg	1.8 to 2.4
Polarization Mode		Alt. Transmit, Alt. Receive (ATAR)
Integrated Cross Pol. Ratio (Max)	dB	−20

The following sections describe the main components of the LPAR system in detail. Section 2.2.1 describes the array front-end performance and specifications. The integrated DREX, detailed in Section 2.2.2, provides coherent transmission and reception of radar signals to the array front-end. The DREX design incorporates a customized control mechanism, which allows for flexible waveform and pulse sequence design. The system supports arbitrary transmit and matched filter waveforms, real-time pulse compression, and complete waveform, PRF, and frequency diversity within the radar instantaneous bandwidth. Section 2.2.3 summarizes the main capabilities and architecture of the radar software which acts as the main point of control to the system and the radar operator.

Table 2.2: LPAR array parameters.

Parameter	Units	Value
Frequency Range	MHz	9300 to 9500
Antenna Type		1-D Phased Array
Polarization		Linear Dual-polarized
Integrated Cross Pol. Ratio	dB	27 dB (peak), 25 dB (all scan angles)
Scan Type		Azimuth over Elevation (AZ/EL)
Scan Range (Azimuth)	deg	−45 to 45
Scan Range (Elevation)	deg	−10 to 90
Azimuth Scan Type		Programmable, discrete positioning
Azimuth Scan Speed		1 µs position switching
Elevation Scan Type		Mechanical
Elevation Scan Speed	deg/s	8
Peak Sidelobe Level	dB	-22 (Taylor Weighting)
Scan Loss		$\cos(\text{azimuth})^{1.5}$
Size (Array Only)	(w x h x d)	1.20 m x 0.75 m x 0.50 m
Weight (Array Only)	kg	125

2.2.1 Array Component

2.2.1.1 Overview

Operating at X-band from 9300 MHz to 9500 MHz, the array subsystem supports switched, dual-linear polarization diversity using the Alternate Transmit/Alternate Receive (ATAR) polarization pulsing scheme. Comprised of 64 center-fed columns of 32 dipole radiating elements each, for a total aperture size of 1.5 m^2, the elevation and azimuth beamwidths at boresight are 2.8° and 1.8°, respectively. Each group of 8 columns are fed by a single 8-channel T/R assembly circuit card, providing over 1 W peak power to each column for a total peak transmit power over 70 W, at a maximum 30 % duty cycle. The system supports a maximum instantaneous bandwidth of 12 MHz. Array parameters for the REV2 system are shown in Table 2.2.

2.2.1.2 Calibration Data

Calibrated reflectivity and differential reflectivity measurements require accurate estimation of both the gain and beamwidth of the array component. Since the array subsystem is a Commercial Off-The-Shelf (COTS) component, a test manual is provided by the manufacturer that contains a subset of calibration measurements made on the array. Near field measurements of the phase and amplitude (known as the *golden* calibration data) for each T/R module are made in the factory[1], but calibrated weather products require accurate far-field measurements. While it is possible to estimate the far-field pattern from near-field measurements [64], far-field measurements are useful for verifying expected array performance.

To this end, far-field measurements at a subset of frequencies and azimuth beam pointing angles were performed by the manufacturer. On the REV1 system, one-way gain and beamwidth (along the principal H- and V-planes) were measured for each polarization in 5° increments at 3 frequencies from 9300 MHz to 9500 MHz, while for the REV2 system only gain was measured in 15° increments at 7 frequencies. The reason for the sparsity in azimuth measurements in the REV2 system is two-fold. First, far-field measurements take significant time and effort to setup and perform. For 91 beam pointing angles in both polarizations across 7 frequencies, this equates to $(91)(7)(2) = 1274$ different measurements that need to be taken. If each measurement takes just 5 min, the far-field measurement procedure would take over 106 h. Taking measurements at a single frequency would still take over two days. So, far-field measurements for a commercial phased array must be carefully chosen to keep the overall component cost low. The second reason for the sparse measurements is due to measurement repeatability. With no significant design changes between the two

[1]These are accessible via the Universal Serial Bus (USB) alternate array controller interface (see Figure 2.1) through a hyperterminal window (115 200/8/N), but use of this interface is not recommended without guidance from the manufacturer or qualified radar operator.

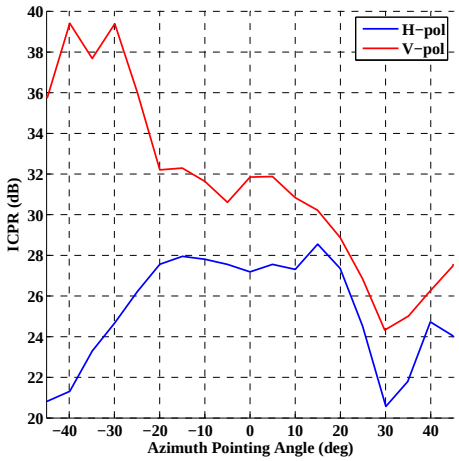

Figure 2.2: LPAR Integrated Cross Polarization Ratio (ICPR).

array systems, the only differences are in the manufacturing tolerances. With strict factory controls and processes, it's assumed that these errors are negligible.

In addition to one-way gain and beamwidth, Integrated Cross Polarization Ratio (ICPR) measurements were also performed during far-field calibration of the REV1 and REV2 systems. ICPR is a figure-of-merit of dual-polarized antennae that characterizes the amount of cross-coupling in the received radar echoes from the principal H-polarization (V-polarization) plane to the cross-coupled V-polarization (H-polarization) plane [71]. ICPR is the amount of measured cross-polarization integrated over the width of the main beam [18]. For polarimetric radars employing the ATAR polarization pulsing scheme, Wang and Chandrasekar [117] showed that ICPR contributes bias errors in reflectivity, differential reflectivity, co-polar correlation coefficient, and specific differential phase estimates. To keep the bias in differential reflectivity below 0.2 dB (0.3 dB), ICPR should be better than 20 dB (18 dB). By comparison, for radars implementing the Simultaneous Transmit/Simultaneous Receive (STSR) dual-polarization scheme, ICPR should be better than 44 dB (42 dB). Figure 2.2 shows the measured cross-polarization ratio for the REV2 system. The ICPR is better than 20 dB for pointing angles from -45° to 45°, and is less than 25 dB

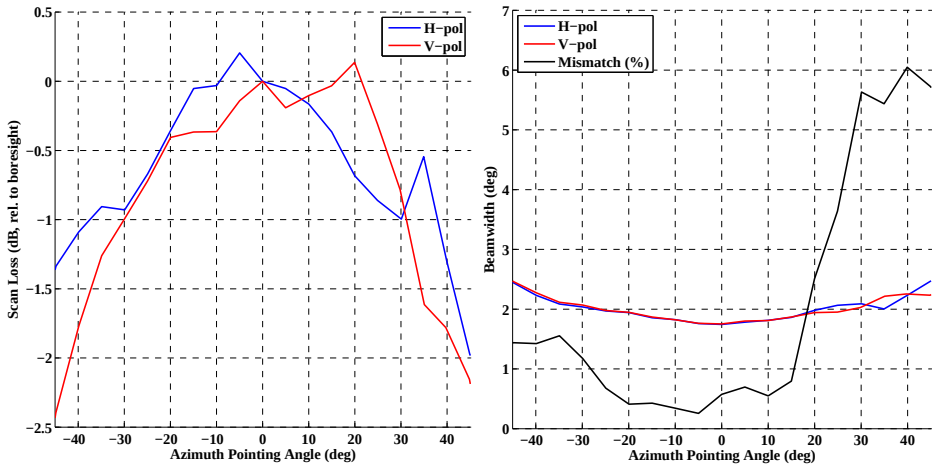

(a) (b)

Figure 2.3: Plots of the (a) scan loss and (b) beamwidth for the LPAR system.

for angles less than 25°. Cross-polarization degrades at angles above 45° (not shown), but the ICPR is still less than 18 dB out to ±55°.

Figure 2.3 shows the array scan loss[2] and principal H-plane (azimuthal) beamwidth in each polarization for the REV1 array. Analysis of the peak gain at each pointing angle (not shown) confirm a beam pointing accuracy over all scan angles and polarizations of ±0.15° and a peak scan loss of −2.5 dB at ±45°. To generate the radar calibration data for weather product estimation from the results of Figure 2.3 at non-characterized pointing angles, the data is interpolated to the desired angle using a cubic spline interpolation technique [93, pp. 113–116].

2.2.1.3 Validation Tests

To validate the far-field measurements and array performance of the system, the REV1 system underwent a second far-field measurement at the University of Massachusetts in the Spring of 2011. Two separate tests were performed to measure both the transmit and receive characteristics of the array. During the receive test, an X-

[2]Scan loss here is taken as the one-way gain versus scan angle relative to the gain at boresight.

band horn was mounted in the far-field towards the array, and a Continuous Wave (CW) tone was injected through the array receive chain. The purpose of this test was to validate receiver linearity and dynamic range, measure array and downconverter gain, and characterize the receive gain and Minimum Detectable Signal (MDS). The receive test confirmed the receive scan loss measurements performed by the manufacturer in Figure 2.3a, and the Spurious-Free Dynamic Range (SFDR) was measured to be better than 86 dB.

In the second test, an X-band corner reflector was setup at a down range of 350 m from the array. The purpose of this test was to measure the Effective Isotropic Radiated Power (EIRP) for the system and compare against the factory estimates of 56 dBW. The EIRP was successfully measured in the H-polarization at 52.5 dBW and V-polarization at 55.5 dBW[3].

2.2.2 Digital Receiver/Exciter Component

The DREX is a Field Programmable Gate Array (FPGA) Intellectual Property (IP) core developed to generate pulsed transmission and reception of arbitrary waveforms on an existing hardware platform containing necessary Analog/Digital Converter (ADC) and Digital/Analog Converter (DAC) components. The IP core is currently used as the underlying Digital Signal Processing (DSP) functionality on an existing COTS hardware platform, the Ettus Research™ Universal Software Radio Peripheral (USRP)[4] model# N210 [39]. The DREX also serves as the communica-

[3]The H-polarization receive gain for the REV1 system is 3 dB lower than in V-polarization, due to a design flaw in the element configuration. This has subsequently been fixed in the REV2 and all later revisions of the system, which have equalized gain in each polarization. Calibrated reflectivity estimates for the REV1 system reflect these gain measurements.

[4]An additional version of the DREX has also been developed to integrate with the USRP model# X310, which provides a larger and updated FPGA, a faster clock speed, and improved filter performance.

tions and signal link between the host computer and the array. Functionally, the DREX provides the following capabilities.

- Coherent transmission and reception of baseband (60 MHz) signals to and from the array
- Communications relay between the host computer and the array
- Logic controls for transmit/receive actions within a pulse period
- Logic controls for selection of polarization to the array for a pulse period

In its default configuration, shown in Figure 2.1, the host controller communicates with the DREX via standard Gigabit Ethernet (GigE)[5]. The DREX is then connected to the array via dual Ethernet lines for logic and data communication signals. The DREX transmits and receives signals from the array at baseband (60 MHz), coherently locked to a 100 MHz reference clock provided by the array.

The USRP N210 is a COTS platform that is marketed as a Software-Defined Radio (SDR). The base COTS hardware supports live-only streaming of 16-bit samples to and from a connected host computer. Existing DSP functionality within the device contains only Digital Up-Converter (DUC) and Digital Down-Converter (DDC) functionality for Intermediate Frequency (IF) waveforms (0 MHz to 250 MHz) within the FPGA. The COTS FPGA code contains a working softcore processor, network interface, and all other FPGA cores required for communicating with peripheral devices mounted on the hardware. Waveforms are transmitted and received from the device through Subminiature Version-A (SMA) connections on a daughterboard circuit card, which is mounted on top of the motherboard of the device. A custom daughtercard

[5]Under nominal conditions, the wire bandwidth over the Ethernet line varies from 50 MHz to 200 MHz, depending on waveform parameters selected.

Table 2.3: DREX digital transmit subsystem parameters.

Parameter	Units	Value	
No. of IF Outputs	Channels	Up to 2	
IF Range	MHz	0 to 250	
Digital Attenuation	dB	0 to 31	
Output Phase Nose	dBc/Hz	@ 10 Hz offset	-93
		@ 100 Hz offset	-103
		@ 1 kHz offset	-118
		@ 10 kHz offset	-133
		@ 100 kHz offset	-145
		@ 1 MHz offset	-141
Clock Jitter	ps RMS	0.62	

was developed to interface the DREX to the array subsystem. The purpose of using a COTS platform for the DREX is to reduce the development cost of the radar system; whereas an internally-developed DREX would take months for hardware and software development to even get basic functionality, the USRP N210 only requires slight modifications before DSP development can begin.

The following sections detail the main functionality and capabilities of the DREX. Section 2.2.2.1 describes the transmit control processing module responsible for building complicated pulse sequences and managing synchronous returns. Section 2.2.2.2 describes the receive chain used to process incoming samples. Tables 2.3 to 2.5 list the DREX specifications for the digital transmit subsystem, waveform generator, and digital receive subsystem, respectively.

2.2.2.1 Control Interface

The DREX builds up a pulse sequence for a radar scan by constructing one or more *dwells* containing one or more Coherent Processing Intervals (CPIs). A CPI is defined as a contiguous series of pulses where the waveform parameters are static for each

Table 2.4: DREX digital waveform generator parameters.

Parameter	Units	Value
PRF (per channel)	Hz	PC disabled 400 to CW PC, 512-pt 400 to 24 800 PC, 1024-pt 400 to 12 400 PC, 2048-pt 400 to 6200
Transmit pulsewidth	µs	0 to 81.92
No. transmit waveforms		Up to 16
Total pulsewidth	µs	120
No. matched filter waveforms		Up to 16
No. samples per matched filter waveform	IQ Samples	2048
Total matched filter samples	IQ Samples	6144
No. phase codes		64
No. center frequencies		64
No. range masks		16
No. of GPIO lines		Up to 32

pulse in the CPI. Here, *waveform parameters* encompass the following parameters for each pulse

- Transmit waveform
- Matched filter waveform
- Waveform center frequency
- PRF
- Range mask (receive window, sampling frequency)
- Starting phase code

The transmit waveform defines the actual 100 MHz waveform samples which are fed to the DAC and output to the array, and the matched filter waveform is the actual

Table 2.5: DREX receiver parameters.

Parameter	Units	Value
No of IF Inputs	Channels	Up to 2
Input sensitivity	dBm	< -70
Input P-1 dB	dBm	8
Input SFDR	dB	87
Max sampling rate	MHz	50
Max pulse compression sample size	points	2048
Data output format		IEEE-754 half or single precision
Data output format options		Pulse compressed IQ data Raw IQ data FFT of received data FFT of matched filter waveform

filter used in the pulse compression block on receive samples from the ADC, if pulse compression is enabled for this CPI. The transmit and matched filter waveforms are loaded at baseband, which allows the center frequency to be arbitrarily set for each CPI.

A phase code can also be applied to each pulse in the CPI. Phase coding is a weather signal processing technique to mitigate second-trip echoes by shifting the phase of transmitted waveforms [37]. The phase code for each pulse is judiciously chosen such that the returns from second-trip echoes are orthogonal to first-trip echoes in a pulse. Typically, phase codes are randomized from pulse-to-pulse, as is the case with a magnetron or klystron radar transmitter, or set to specific code sequences having known performance [43]. Phase coding works by shifting the starting phase of transmitted waveforms (before samples are sent to the DAC) and *unwrapping* the starting phase on receive (after digital downconversion to baseband).

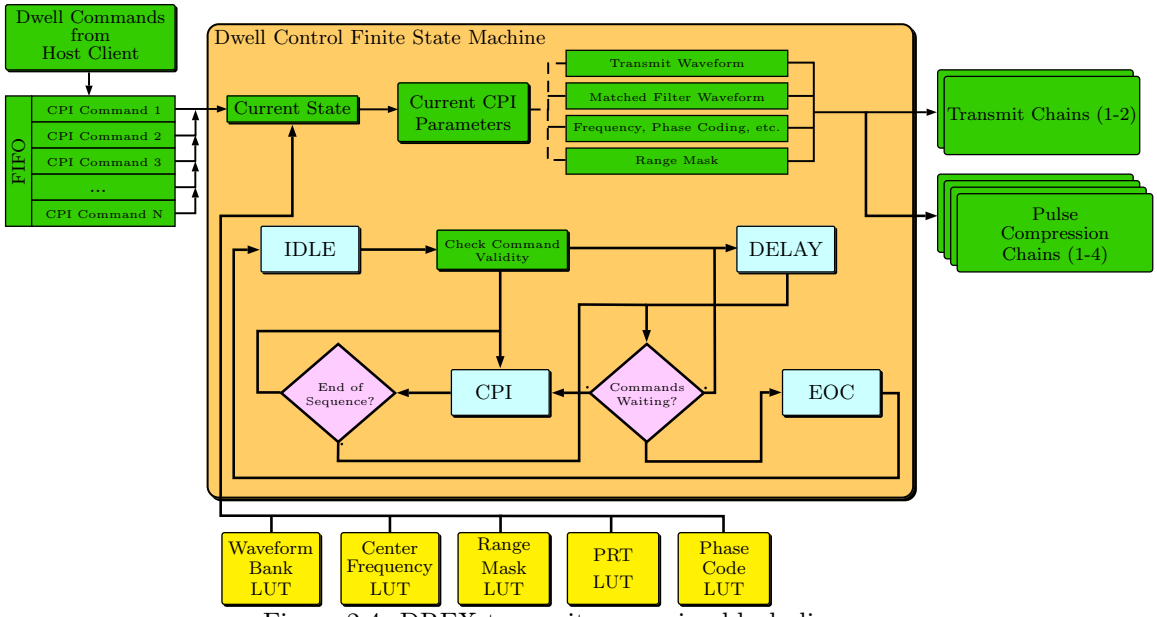

Figure 2.4: DREX transmit processing block diagram.

For each radar scan, the radar software builds up the pulse sequences for the radial by feeding the DREX CPI commands in succession. Within the DREX, a First-In, First-Out (FIFO) queue iteratively processes and executes each CPI command received. Since the radar software communicates to the DREX via User Datagram Protocol (UDP) packets, there is an inherent delay between when the radar software commands a CPI and when it is actually executed. This delay is caused by kernel latencies in the socket protocol, delays in the UDP stack in the DREX, and setup delays in the control processing module. This delay is nominally between 10 ms to 100 ms and varies depending on the frame size chosen (typ. 8192 B). Control logic within the DREX injects the CPI commands as inputs to a synchronous, Mealy Finite State Machine (FSM). The state machine is used to drive logic signals for setup of waveform parameters on each pulse. Figure 2.4 shows a diagram of the transmit control interface logic, including a simplified flow diagram for the FSM used in CPI processing. By constructing radial pulse sequences from multiple CPI commands, the DREX is able to support switching of any combination of waveform parameters on a

pulse-to-pulse basis. Thus, the DREX can support simultaneous waveform, frequency, and PRF diversity.

2.2.2.2 Receive Signal Processing Overview

This section summarizes the fundamentals of the digital pulse compression technique, specifically pertaining to implementation details on an FPGA. For a more complete derivation and description of pulse compression and correlation details, refer to [108, 97, 62].

The pulse compression implementation processes received In-phase and Quadrature (IQ) samples within each receive window of the pulse interval through a digital filter. For received voltage samples $s_r(t)$ and filter coefficients $h(t)$, the output of the filter in the time domain is given by

$$s_f(t) = \int_{-\infty}^{\infty} s(\tau)h(t-\tau)d\tau \tag{2.2.1}$$

From inspection of (2.2.1), it is evident that the filtering of received radar waveform samples is equivalent to convolution of the received signal with time-reversed filter samples. We can rewrite the time-domain expression in (2.2.1) in the Fourier domain by recognizing that convolution in the time domain is equivalent multiplication in the Fourier domain, which transforms (2.2.1) to

$$s_f(t) = \int_{-\infty}^{\infty} S(f)H(f)\exp\left[i2\pi ft\right]df \tag{2.2.2}$$

The purpose of *matched filtering* is to choose $h(t)$ such that the output Signal to Noise Ratio (SNR) is optimized in the presence of white noise. From Schwarz's Inequality, it can be shown [62, pp. 59–63] that the maximum SNR is achieved when the filter's transform function equals the complex conjugate of the received signal itself, $S^*(f)$. This is known as the *matched filter* for $s(t)$. If the filtered signal is the received echoes

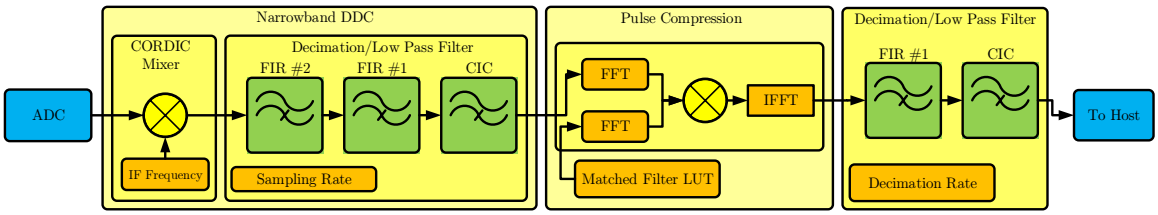

Figure 2.5: DREX receive DDC and pulse compression block diagram.

from a pulsed waveform, then the matched filter will produce maximum SNR aligned with the presence of received waveform echoes.

The DREX implements the pulse compression technique in the Fourier domain using Fast Fourier Transform (FFT) correlation. This technique performs the filtering technique given by (2.2.2), which is simply the Inverse FFT of the product of the FFT of the received, baseband IQ samples ($s(t)$) at the output of the DDC and the conjugate of the matched filter waveform ($h(t)$) for a given pulse,

$$s_0(t) = \text{IFFT}\left\{\text{FFT}\left[s(t)\right]\text{FFT}\left[h(t)\right]^*\right\} \tag{2.2.3}$$

The block diagram of the DREX DDC and pulse compression chain is shown in Figure 2.5. The DDC implements a three stage cascade of Finite Impulse Response (FIR) filter blocks [31]. The input stage stage is a Cascaded Integrator-Comb (CIC) filter, which is an efficient filter design for decimating high-rate samples. CIC filters trade performance for efficiency by cascading a comb filter, a downsampling block, and an integrator. Using only addition and subtraction operations, the CIC filter is able to decimate by an integer amount with minimal resources at the expense of a poor passband respond. The final two stages in the DDC utilize a traditional FIR block structure, as either half-band or decimation filters. Down-mixing is implemented by means of a COordinate Rotation DIgital Computer (CORDIC) algorithm.

2.2.3 Radar Software Overview

The radar software package, known as the Radar Operating System (*rOS*), encompasses the command and control, signal processing, data archiving, and data display functionality for the LPAR system. The software is designed to be fully integrated with the DREX as the main focal point for communication to and from the array subsystem. All software components, with the exception of the user interface, are written in the C++ programming language. The software was developed for the Red Hat Enterprise Linux (RHEL) or Community Enterprise Operating System (CentOS)[6] using the GNU Compiler Collection (GCC) compiler with `C++0x` functionality enabled (RHEL v2.6, GCC v4.4.7). Due to the use of Streaming Single-instruction, multiple data Extension (SSE) intrinsics to optimize high-throughput calculations, the system requires an Intel processor with at least 8 GB of Random Access Memory (RAM). The software package has successfully been deployed on a Dell desktop with an Intel i7-3960XM processor (4 cores, 8 threads) with 8 GB RAM and 1 TB Hard Disk Drive (HDD) storage. The web-based user interface uses a combination of HTML, javascript, PHP, and SQL (HTML v5, PHP v5.5, SQL v5.6). Figure 2.6 shows a block diagram of the major software components.

In addition, a Matlab software simulation of the radar software was developed[7] that allows recorded timeseries data to be post-processed. This Matlab suite performs equivalent processing to the pulse-pair signal processing algorithm implemented in software and is a useful verification and development tool.

The functionality of the software can be broken down into four different parts: command and control, signal processing, data archiving, data display, and user inter-

[6]The CentOS operating system is derived from the source code RHEL, and contains much of the same capabilities and functionality. As the Linux operating is open-source software under the GNU General Purpose License (GPL) license, the major difference from RHEL to CentOS is the help and support offerings.

[7]The Matlab software package is available upon request.

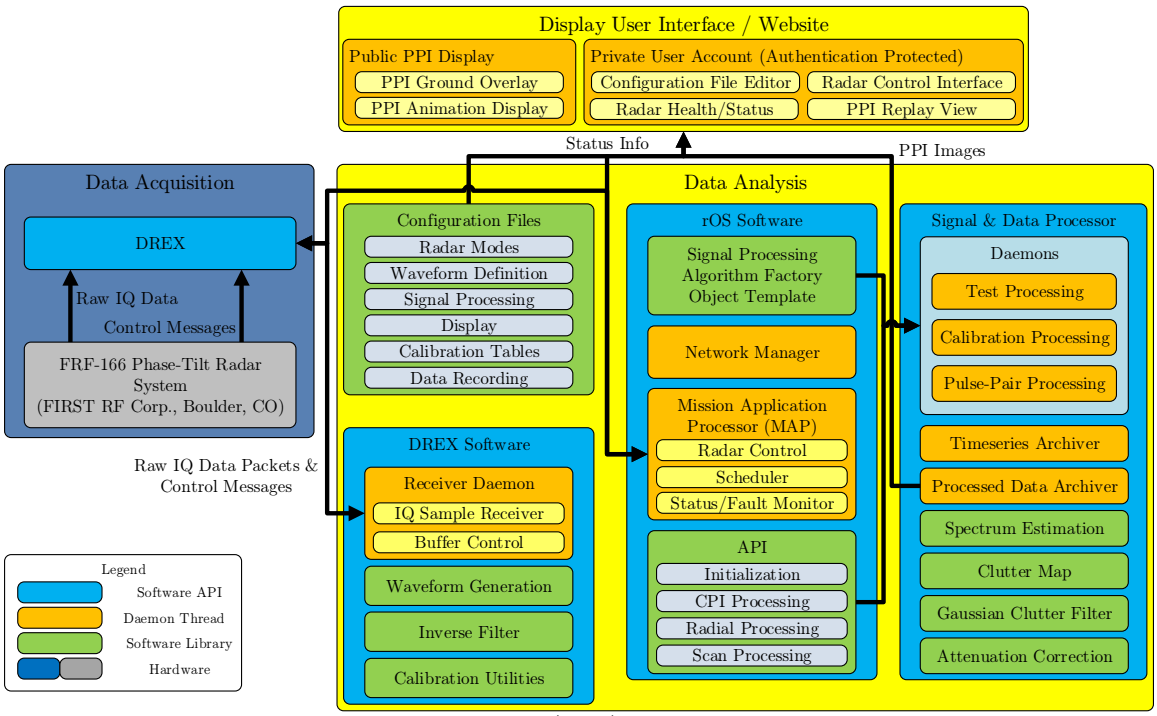

Figure 2.6: LPAR Radar Operating System (*rOS*) radar software architecture block diagram.

face. The following sections describe each component in detail. The documentation for all software components is available online at the University of Massachusetts Amherst LPAR system website (`http://casa-ptwr-node.ecs.umass.edu/html/doc/rOS/doxygen/html/index.html`).

2.2.3.1 Command and Control

The radar is controlled and setup up for operation via external Extensible Markup Language (XML) configuration files. These configuration files must be setup prior to start of radar operations. Configuration files control the radar scanning actions, waveform configuration to the DREX, signal processing options, data display options, radar and array calibration tables, and timeseries recording capability.

Within the software, a Mission Application Processor (MAP) daemon thread is responsible for the main control loop of the radar. The MAP makes use of a two-tiered, priority-based radar scheduler that sets up radar scanning actions based upon user input in the configuration file. An external *network manager* daemon allows

radar scanning actions to be requested on-the-fly via a UDP communication protocol external to the radar software. The MAP communicates with the Network Manager and downstream *signal processing* daemons via UDP connections for data throughput, status and fault reporting, and acknowledge messages.

Radar scanning actions, known as Radar Action Requests (RARs), are defined in an external configuration file and setup within the MAP during live operation. A RARs defines the timing, scanning geometry, waveform parameters, and signal processing parameters for each radar mode to be executed. The software is multi-mission capable, so multiple radar modes can be scheduled concurrently. Internally, a set of rules within the radar scheduler decides the order in which radar modes are executed.

To facilitate recurring calibration actions, such as noise estimation measurements, the MAP autonomously schedules and executes a pre-defined set of *nominal* radar modes. At this time, nominal radar modes are defined for (1) noise estimation every 5 min and (2) zero range delay calibration every 24 h. Noise estimation is periodically performed to update internal Look-Up Tables (LUTs) of noise estimates at each beam position, used by the signal processing algorithms for accurate SNR estimation. Zero-range delay measurements feed a pilot pulse through the array subsystem to measure the inherent system delay and calibrate zero range for the radar at the plane of the array face.

2.2.3.2 Signal Processing

The processing flow of received IQ data in the software is as follows. A background receiver daemon autonomously receives samples from the DREX using a zero-copy

MAP socket interface into a set of circular buffers[8]. Each circular buffer is tied to a specific signal processing daemon thread, which then processes the data.

Currently, three signal processing daemons are instantiated. A pulse-pair weather signal processing algorithm (see Chapter 3) processes received IQ samples and computes the polarimetric weather products. A calibration algorithm processes noise and zero-range calibration data from nominal radar modes. A test algorithm is also used to process data from array subsystem tests.

All signal processing threads are constructed from a common factory object[9] template. Each signal processing daemon processes receives IQ data at distinct processing points in time:

1. When a single block of pulses arrives (typ. 32)
2. When data from an entire radial is received
3. At the completion of all radials for a radar mode
4. At the completion of all radials across all radar modes executed at the current elevation tilt

These four processing points describe the actions of a signal processing algorithm.

2.2.3.3 Data Archiving

Processed data from the signal processing daemons are fed to a *data archiver* daemon, which archives the data in Network Common Data Format (NetCDF) files

[8]A zero-copy socket implementation exposes an external buffer that the kernel uses to copy received data packets into. This buffer is then accessed from user-space directly. As traditional sockets copy the data first into a kernel buffer and then into a user-space buffer, zero-copy sockets increase data throughput by eliminating the redundant copy into the second buffer in user-space.

[9]The *factory object* software paradigm uses a base software class to encapsulate common functionality, but allows specific instantiations of the base class to modify or add new capabilities and processing. The factory object paradigm allows additional software processing daemons to be quickly instantiated for research purposes.

[96]. Each signal processing daemon feeds data to a different data archiver daemon, and a new NetCDF file is created for each radar action request executed. Data archiving can be enabled or disabled in the radar action request.

Raw timeseries data recording can be enabled via a flag in an external configuration file. Raw timeseries data is recorded in binary format to disk, and an external executable is provided to post-process the binary data into NetCDF files for useability. Currently, the system supports up to 4 h of continuous timeseries recording to the local host computer, assuming sufficient disk space is available.

2.2.3.4 Data Display

After the completion of each radar mode, processed weather products are fed to a common Planned Position Indicator (PPI) Generator daemon. The PPI generator generates a Portable Network Graphics (PNG) file for each weather product. A nearest-neighbor interpolation algorithm is implemented that generates PNG files for each azimuth scan. Using a binary search algorithm, the PPI generator can generate the PNGs for all weather products and ancillary variables (currently 27 images) in less than 1.5 s.

2.2.3.5 User Interface

While the software is primarily accessed via command-line executables, a web-based user interface (see `http://casa-ptwr-node.ecs.umass.edu/` was developed to interface to the radar remotely. The website uses a mobile-first, responsive design[10] to increase useability across multiple platforms from desktops to smartphones

[10]The term *mobile-first* is a website design paradigm that focuses on optimal viewing primarily from mobile devices having small screen sizes. The term *responsive* describes a website designed to be loaded, viewed, and accessed with negligible delay and a minimal amount of scrolling, resizing, or panning. Together, these terms represent a paradigm shift for web development in recent years to a more user-friendly internet experience.

and tablets. Figure 2.7 shows a preview of the main website and PPI map overlay (inset) of the user interface.

The user interface uses an online login account system to support multiple, independent radar operators for different research purposes. To begin, each new user must first register a user account from the registration page on the radar website. Once registered, the site administrator or radar project manager must then activate the account before the user can operate the radar. Associated with each new user is a distinct set of configuration files for the radar software, stored in a protected directory on the radar host computer. Since the radar software can be setup at run-time to point to a specific directory for configuration files, this allows each registered user to maintain their own independent radar configuration. Thus, different users can be registered for the system to perform research on separate, disjoint research endeavors. For example, a user performing research on weather phenomena will have a different configuration than one interested in target surveillance.

Each user must login to the website to view and modify their configuration files, start and stop radar live operation, and view radar health and status messages. Live PPI images generated from the radar are overlaid on a Google Maps display in real-time. Different weather products can be selected for display from the most-recent radar scan, or an animation loop of the previous 50 scans.

This user account system represents a new paradigm for phased array research and education. Traditional phased array radars are closed systems that are complicated to operate safely and require significant training. Starting or stopping radar execution can be convoluted, and is normally left to an experienced radar operator. By exposing the radar interface through a user-friendly web interface, multiple, geographically-separated research groups or academic institutions can experience the advantages of rapid, phased array scanning. Research centers unable to afford the cost of purchasing or maintaining a phased array can perform independent experiments

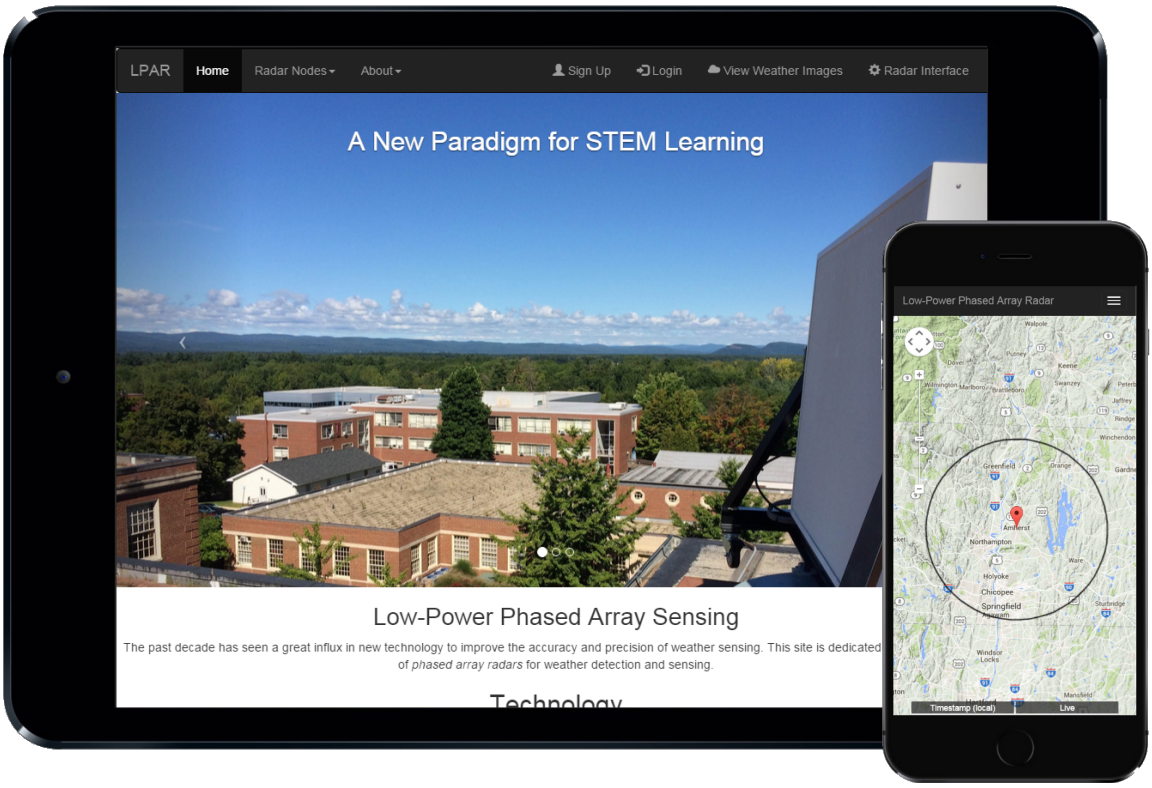

Figure 2.7: Preview of the *rOS* user interface main page and PPI display (inset).

remotely. Upper-level undergraduate and graduate students can perform hands-on projects or assignments. Testing has shown that the account system should scale well to 15 to 20 simultaneous users, which allows support for professor to use the radar in the curriculum for a course.

2.3 Scanning Geometry

The scanning geometry for the phase-tilt array architecture is a specific case of the generalized coordinate system for a mechanically-tilted 2D phased array radar scanning along its principal azimuthal axis. This formulation makes use of both *Radar-local*, *Mount*, and *Earth* coordinate systems.

2.3.1 Radar Coordinates

The *radar*-local coordinate defines a Cartesian (x, y, z) coordinate system with the array centered at the origin. The plane of the array lies along the $y-z$ plane. The central row of elements in the array (assuming a centered rectangular lattice) is alone the y-axis, and the central column of elements is along the z-axis. The scanned beam is at a direction (θ, ϕ), where θ is the azimuth angle as measured from the x-axis and ϕ is the elevation angle measured from the xy-plane. A beam scanned at direction [0°,0°] is aligned with the x-axis and referred to as *boresight*.

For a target at an absolute range r from the radar center and the array scanned to angle (θ, ϕ), the Cartesian coordinates of the target in the radar-local reference frame can be derived from the spherical coordinates (r, θ, ϕ) as

$$\overrightarrow{a_x^r} = \cos\theta \sin\phi \tag{2.3.1a}$$

$$\overrightarrow{a_y^r} = \sin\theta \sin\phi \tag{2.3.1b}$$

$$\overrightarrow{a_z^r} = \cos\phi. \tag{2.3.1c}$$

The spherical and Cartesian coordinates in the radar-local reference frame are often referred to as Radar Azimuth/Elevation (RAE) and Radar-Centered, Radar-Fixed (RCRF) coordinates, respectively. In a similar fashion, spherical (r, θ, ϕ) coordinates can be derived from Cartesian (a_x^r, a_y^r, a_z^r) coordinates via

$$\overrightarrow{a_r} = \overrightarrow{a_x} \cos\theta \sin\phi + \overrightarrow{a_y} \sin\theta \sin\phi + \overrightarrow{a_z} \cos\phi \tag{2.3.2a}$$

$$\overrightarrow{a_\theta} = -\overrightarrow{a_x} \sin\theta + \overrightarrow{a_y} \cos\theta \tag{2.3.2b}$$

$$\overrightarrow{a_\phi} = \overrightarrow{a_x} \cos\theta \cos\phi + \overrightarrow{a_y} \sin\theta \cos\phi - \overrightarrow{a_z} \sin\phi. \tag{2.3.2c}$$

2.3.2 Mount Coordinates

For the phase-tilt architecture, the mechanical tilt transforms the normal radar-local reference frame, and the radar scans in an arc across a single elevation tilt. To account for this mechanical tilt, the problem is generalized to that of the array mounted on a pedestal. In the *mount* coordinate system, the pedestal is centered at the origin, the array center is displaced from the mount axis of rotation by a coordinate translation $\overrightarrow{d} = (d_x, d_y, d_z)$, and the pedestal is pointing at an angle (A_m, E_m). Here, A_m is measured from the x-axis and E_m is measured from the yz-plane. It should be noted that A_m and E_m correspond to *pitch* and *yaw* in the *pitch-roll-yaw* convention.

2.3.3 Earth Coordinates

There are two reference frames used to specify the location of the radar with respect to the Earth; geographic and local. Geographic reference frames, including Latitude-Longitude-Height (LLA) and Earth-Centered, Earth-Fixed (ECEF), allow every location on Earth to be specified in a single coordinate system. LLA defines latitude as the angle between the equatorial plane and the straight line that passes through a location on the Earth and through the center of the Earth. Longitude is the angle East or West of a reference *meridian*, which is a half-arc connecting between the North and South poles of the Earth. The international *prime meridian* is located at the British Royal Observatory (Greenwich, England). Altitude is the height above sea-level. Unless otherwise specified, positive longitude lie to the west of the prime meridian.

The ECEF reference frame is a Cartesian coordinate system with the origin located at the center of the Earth. The x-axis passes through the (latitude, longitude) point (0°, 0°), the y-axis passes through the point point (0°, 90°E), and the z-axis passes through the north pole.

In contrast, the East-North-Up (ENU) is a local reference frame relative to the location of a point on the surface of the Earth. Here, the x-axis points East, y-axis points North, and the z-axis points upwards perpendicular to the surface of the Earth. The radar *heading* is defined as the angle between the projection of array boresight onto the surface of the Earth and true North (y-axis). Heading angles run clockwise when looking down on the xy-plane.

2.3.4 Radar to Mount Coordinate Transformation

For a resolution cell at range $\overrightarrow{r}$ sufficiently larger than the array displacement $\overrightarrow{d}$ ($|\overrightarrow{r}| \gg \left|\overrightarrow{d}\right|$) and array boresight aligned perpendicular to the pedestal axis of rotation, the mount displacement can be ignored and the pointing angle in the Mount coordinate system can be expressed as a coordinate rotation

$$\overrightarrow{a_m} = \mathbf{A} \begin{pmatrix} \cos\theta \sin\phi \\ \sin\theta \sin\phi \\ \cos\phi \end{pmatrix} \tag{2.3.3}$$

Where $\mathbf{A}$ is a coordinate rotation matrix in the ZYX (*pitch-roll-yaw*) convention

$$\mathbf{A} = \begin{bmatrix} \cos A_m \cos E_m & \sin A_m \cos E_m & -\sin E_m \\ -\sin A_m & \cos A_m & 0 \\ \cos A_m \sin E_m & \sin A_m \sin E_m & \cos E_m \end{bmatrix} \tag{2.3.4}$$

Cartesian coordinates in the mount reference frame from those in the radar frame are found by expanding (2.3.3)

$$\overrightarrow{a_x^m} = \cos A_m \cos E_m \cos\theta \sin\phi - \cos\phi \sin E_m + \cos E_m \sin A_m \sin\phi \sin\theta \tag{2.3.5a}$$

$$\overrightarrow{a_y^m} = -\sin\left(A_m - \theta\right) \sin\phi \tag{2.3.5b}$$

$$\overrightarrow{a_z^m} = \cos E_m \cos\phi + \cos A_m \sin E_m \cos\theta \sin\phi + \sin A_m \sin E_m \sin\phi \sin\theta. \tag{2.3.5c}$$

Mount spherical coordinates can be found by geometric manipulation of (2.3.5). As before, spherical and Cartesian coordinates in the mount reference frame are often referred to as Mount Azimuth/Elevation (MAE) and Mount-Centered, Mount-Fixed (MCMF). For the simple case of $A_m = 0$ (no pedestal azimuth positioning), (2.3.5) can be transformed to

$$\overrightarrow{a_\theta} = -\arctan\left[\frac{\sin\phi \sin\theta}{\cos\phi \sin E_m - \cos E_m \cos\theta \sin\phi}\right] \tag{2.3.6a}$$

$$\overrightarrow{a_\phi} = \arctan\left[\frac{\cos E_m \cos\phi + \sin E_m \cos\theta \sin\phi}{\sqrt{\left(\cos\phi \sin E_m - \cos E_m \cos\theta \sin\phi\right)^2 + \sin^2\phi \sin^2\theta}}\right]. \tag{2.3.6b}$$

For a phase-tilt architecture and no pedestal azimuth positioning, substituting $\phi = \pi/2$ into 2.3.6 gives the equations for the true azimuth and elevation of the LPAR system (after simplification)

$$\overrightarrow{a_\theta} = \arctan\left[\tan\theta \sec E_m\right] \tag{2.3.7a}$$

$$\overrightarrow{a_\phi} = \arccos\left[\cos\theta \in E_m\right] \tag{2.3.7b}$$

The formulas in (2.3.7) for the true azimuth and elevation of a 1D phase-tilt array agree with the formulation given by Orzel [81].

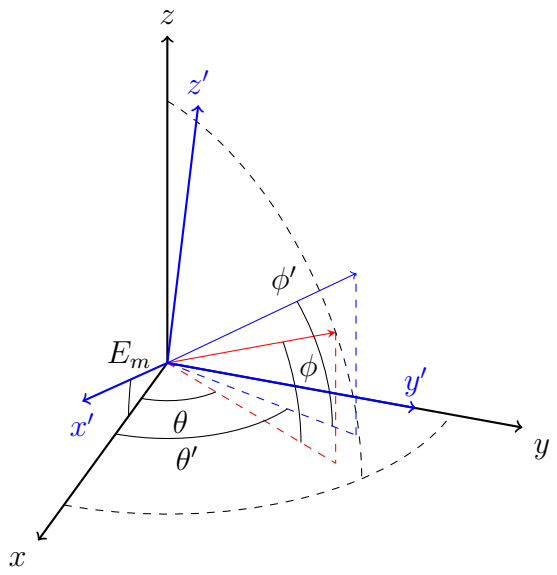

Figure 2.8: Spherical coordinate system for a tilted 2D phased array radar scanning at beam pointing angle (θ, ϕ) with mechanical tilt E_m. The tilted coordinate system and beam pointing angle (θ', ϕ') is shown in blue.

For this work, the mount reference frame will henceforth be used when discussing azimuth and elevation angles with respect to the radar location. Figure 2.8 shows a diagram of the spherical coordinate systems in the mount reference frame. The black $x-y-z$ axis depicts the mount reference frame, and the blue $x-y-z$ axis shows the rotated radar-local frame with a pedestal tilt of E_m ($A_m = 0$). The blue and red vectors show the difference in pointing angles from the radar-local to the mount reference frame, respectively.

2.4 Azimuth Sequencing

The LPAR system supports three methods of sequencing azimuth radials within a scan: (1) sequential, (2) random, and (3) multiplexed. A traditional, sequential azimuth sequence will mimic the behavior of a mechanically-rotated radar by incrementing the azimuth position in fixed, discrete amounts. For a desired azimuth sector from [θ_{start}:θ_{step}:θ_{stop}], the total number of radial positions is

$$N_r = 1 + \left\lfloor \frac{|\theta_{stop} - \theta_{start}|}{\theta_{step}} \right\rfloor . \tag{2.4.1}$$

Each of the r radial positions in the sequence ($\theta^{seq}[r]$) are then computed as

$$\theta^{seq}[r] = \theta_{start} + \sum_{r=0}^{N_r} \frac{|\theta_{stop} - \theta_{start}|}{N_r - 1}. \tag{2.4.2}$$

In this manner, the azimuth sector covers from θ_{start} to θ_{stop} in θ_{step} increments, inclusive. This algorithm assumes that the azimuth limits are in strict ascending order and relative to array boresight.

Once the sequential azimuth sequence is generated, the random and multiplexed types are derived from these radial positions. The random sequence type randomly shuffles the radial positions in $\theta^{seq}[r]$, with replacement

$$\theta^{rand}[r] = \text{random}\left[\theta^{seq}[r]\right]. \tag{2.4.3}$$

The randomized azimuth sequence method places no restrictions on the placement of radials. That is, it does not guarantee that two sequential radial positions, $\theta^{sec}[1]$ and $\theta^{sec}[2]$, won't still be executed sequentially. To overcome this restriction, the multiplexed sequencer should be used.

The multiplex sequencer works by spacing radials from $\theta^{seq}[r]$ maximally far away from one another. The psuedocode for this technique is shown in Algorithm 1. The multiplex sequence orders radials such that two sequential radials, $\theta^{seq}[1]$ and $\theta^{seq}[2]$, are maximally far away ($\geq \lfloor\sqrt{N_r}\rfloor$) from one another. Thus, for an azimuth sequence from [−45°:1°:45°], the multiplex sequence will be

$$\theta_{mx}[-45:1:45] = [-45, -36, -27, \dots]$$

The use of multiplexed radial sequences guarantees that radials from closely-separated azimuth positions will be not be executed sequentially. Thus, any round-trip echoes

Algorithm 1 Pseudocode for the generation of multiplexed radial positions (θ^{mx}) from sequential radial positions (θ^{seq}). For N_r total radials in a sequence, a multiplexed sequence (θ^{mx}) is one in which two sequential radials, $\theta^{seq}[1]$ and $\theta^{seq}[2]$, are ordered such that $\theta^{seq}[2]$ is maximally far away ($\geq \lfloor\sqrt{N_r}\rfloor$) from $\theta^{seq}[1]$. This condition holds for any two beam positions from θ^{mx}.

```
1: procedure GENERATEMULTIPLEXSEQUENCE(θ^seq[r], N_r)
2:     Δ_θ ← ⌊√N_r⌋                          ▷ Compute the radial spacing
3:
4:     i ← 0
5:     s ← 0
6:     for r in 0 to N_r do                   ▷ Set the ith beam position
7:         θ^mx[r] ← θ^seq[i]
8:         i ← i + Δ_az
9:         if i > N_r then
10:            i ← s
11:            s ← s + 1
12:        end if
13:    end for
14:
15:    return θ^mx[r]                         ▷ Multiplexed beam positions
16: end procedure
```

from the last pulse in the first radial will not appear in the first pulse on the next radial.

2.5 Waveform Generation

As described in Section 2.2.2, the DREX acts as an arbitrary waveform generator. As such, the LPAR software includes built-in support for advanced waveform generation algorithms. The system supports three types of waveforms: Linear Frequency Modulated (LFM), Non-Linear Frequency Modulated (LFM), and Piecewise-Linear Frequency Modulated (PLFM). The LFM waveform is the generic swept-frequency waveform whose complex envelope is expressed as

$$s_{LFM}(t) = w(t) \exp\left[j\pi Bt\right], 0 \leq t \leq \tau \tag{2.5.1}$$

Where B is the total swept bandwidth of the waveform (Hz), t is the time within the pulse, τ is the uncompressed pulsewidth (s), and $w(t)$ is an amplitude weighting function. Currently supported weighting functions include the Hamming, Hann, and Blackman [97]. The instantaneous frequency of (2.5.1) is

$$f_{LFM}(t) = -\frac{B}{2} + \left(\frac{1}{2\pi}\right)\frac{d\psi}{dt} = -\frac{B}{2} + Bt. \tag{2.5.2}$$

Here, $\psi(t)$ is the time-varying phase of the waveform. From (2.5.2), it is evident that the frequency sweeps linearly throughout the duration of the pulse[11]. Practically, the software generates the LFM waveform as 16-bit IQ samples and loads them to the DREX. The LFM waveform generates waveform samples from a non-linear instantaneous frequency, given by [4]

$$f_{NLFM}(t) = B\left\{\frac{\tan\left(2\beta t/\tau\right)}{2\alpha}\right\} \tag{2.5.3}$$

Where $\beta = \tan^{-1}(\alpha)$. The PLFM waveform is a custom waveform definition that sweeps the frequency over the width of the pulse in discrete, linear segments. The piecewise segments define the points $[x_i, y_i]$ that the instantaneous frequency should pass through, normalized to the total pulsewidth and bandwidth of the waveform. In this manner, the slope within each segment is normalized such that after all points are passed through, the waveform will sweep over the specified pulsewidth and bandwidth. The list of points must include the endpoints of the waveform at $[-1, -1]$ and $[1, 1]$; if they are not specified, the software will append them automatically. As an example, specifying the point $[0, 0]$ will generate a LFM waveform.

It should be noted that the PLFM can be used to generate either the LFM or LFM waveforms directly. Care should be taken when designing either the LFM or

[11]Some implementations of the LFM waveform sweep linearly from 0 to B over the pulse. Both forms of the LFM are equivalent representations. The form mentioned here straddles the swept bandwidth over the width of the pulse, so that the transmit frequency at X-band is located at $\tau/2$.

PLFM waveforms, as achieving low range-sidelobes with pulse compression is not a trivial task. External, Matlab-based generation routines are available to support the offline designing of waveforms.

2.6 Overview of Available Data Sets

2.6.1 Forest Fire Data Sets

From April to May 2013, the LPAR REV1 system was deployed to South Australia in cooperation with the University of Massachusetts Amherst (Amherst, MA) and the University of Adelaide (South Australia, AU). During this time, the system made polarimetric observations at over one dozen prescribed burns and one uncontrolled bushfire. From the fires observed, seven data sets were collected and determined to contain valid smoke plume returns. Valid data sets are those that measured a prolonged period (>15 min) of positive SNR (>10 dB) that corresponded with visual observations of the smoke plume during the burn. Table 2.6 lists the valid data sets collected during the field campaign. One of the bushfires attended was an uncontrolled bushfire in Cherryville, while the rest were prescribed burns conducted by South Australian County Fire Services (CFS), Australian Department of Environmental, Water and Natural Resource (DEWNR), and South Australian Forestry Corporation (ForestrySA) personnel.

2.6.2 Precipitation Data Sets

All precipitation data sets were collected in the Winter to Summer 2015 at the University of Massachusetts Amherst. Amherst is situated in Western Massachusetts in Hampshire County, which is located in the southern half of the Connecticut River Valley, colloquially known as the Pioneer Valley. The topography of Amherst and the surrounding areas predominantly includes the Berkshire Mountains to the west and the nearby steeply rolling hills of the Mount Tom and Holyoke Ranges. The climate in

Table 2.6: Prescribed burns and uncontrolled bushfire dates and locations.

Burn Site	Date	Area Burned (ha) (acres)	Ignition
Belair CP	4-April-2013	9.0 (22.2)	strip head
	5-April-2013	16.9 (41.8)	strip head
South Para Reservoir	10-April-2013	26.0 (64.2)	strip head
Barossa Reservoir	17-April-2013	47.6 (117.6)	aerial
Cleland CP	28-April-2013	10.0 (24.7)	strip head
Cox Scrub CP	1-May-2013	40.0 (98.8)	strip head
Kyeema CP	2-May-2013	39.6 (97.8)	strip head
Cherryville	9-May-2013	650 (1600)	uncontrolled
	10-May-2013	650 (1600)	uncontrolled

western Massachusetts is primarily affected by two types of air masses: cold, dry air from North America moving to the south and warm, moist air flowing from the Gulf of Mexico to the south and the waters of the Gulf Stream from the east. Amherst averages 133 days of precipitation with annual precipitation totals between 40 and 50 inches.

For testing, the radar in Amherst was installed on a roof platform at the University of Massachusetts Amherst ([42.394 070,−72.529 244]) on a mechanical pedestal that allowed for manual azimuthal positioning of the 90° radar field-of-view. The tilt motor actuator on the array was not functional, so data sets were constrained to a fixed elevation tilt. The elevation tilt was set from 3° to 4° for all tests, to minimize clutter contamination and beam blockage from the nearby Mount Tom Range. The radar heading was set at either a southwestern (≈245°) or northwestern (≈325°) direction. Beam blockage from academic buildings prevented scanning to the direct south or east.

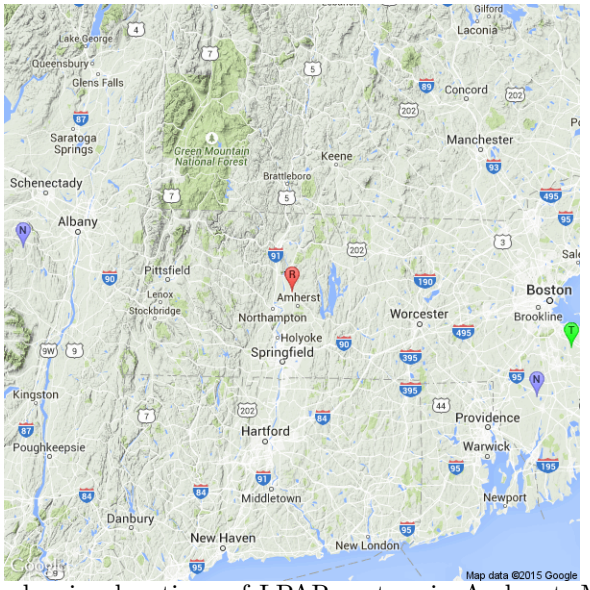

Figure 2.9: Terrain map showing locations of LPAR system in Amherst, MA (red marker), Next-Generation Radar (NEXRAD) stations in Albany, NY and Taunton, MA (purple markers), and the Terminal Doppler Weather Radar (TDWR) station in Boston, MA (green marker).

Figure 2.9 shows a terrain map of the LPAR and nearby NEXRAD and TDWR locations in New England. The red marker signifies the location of the LPAR radar, the purple markers signify the nearby NEXRAD stations, KENX (Albany, NY) and Taunton, MA (KBOX), and the green marker signifies the TDWR station in Boston, MA (BOS).

Table 2.7 shows a listing of the LPAR and nearby NEXRAD and TDWR radar locations. The table also shows the distance from each NEXRAD and TDWR station to Amherst, and the elevation (Above Sea Level, ASL) of the lowest elevation tilt at Amherst[12]. As Amherst is located almost directly between two NEXRAD stations, the lower atmosphere below 1 km altitude is unobserved, which limits the ability of weather forecasters to detect and predict surface weather conditions in the area. This data does not take into account the blockage of the NEXRAD stations due to the

[12]The lowest elevation tilt is taken to be 0.5° for NEXRAD [37] and 0.6° for TDWR [60]

Table 2.7: Locations of LPAR used for weather precipitation collections and nearby NEXRAD and TDWR stations.

Radar	Location	Elevation (ASL, m)	Distance to LPAR (km)	Elevation of Lowest Tilt at Amherst, MA (km)
LPAR	Amherst, MA (42.394070, −72.529244)	79.8	-	-
NEXRAD (KENX)	Albany, NY (42.5800018, −74.0699997)	576.4	130	1.14
NEXRAD (KBOX)	Taunton, MA (41.9500008, −71.12999737)	65.8	122	1.16
TDWR (BOS)	Boston, MA (42.15806, −70.93389)	75.6	133	1.43

Berkshire mountains and hills surrounding Amherst, which further limit NEXRAD visibility in the Pioneer Valley.

Table 2.8: Available precipitation data sets.

Date	Time (UTC)	Precipitation Type	Precipitation Event
25-March-2015	2100 – 2330	moderate rain, freezing rain, snow	
26-March-2015	1620 – 2350	light to moderate rain	
27-March-2015	0152 – 0360	moderate rain, snow	
3-April-2015	0004 – 1806	light rain	
7-April-2015	1813 – 2043	moderate rain	
17-April-2015	0615 – 1319	heavy rain	
20-April-2015	1107 – 1846	heavy rain	
22-April-2015	1557 – 2229	heavy rain, squall line	
19-May-2015	1013 – 1129	heavy rain	Severe Thunderstorm Warning
27-May-2015	1931 – 2359	heavy rain, squall line	Severe Thunderstorm Warning
28-May-2015	0000 – 0116	heavy rain	Severe Thunderstorm Warning
28-May-2015	1200 – 1239	heavy rain, isolated thunderstorms	Severe Thunderstorm Warning
31-May-2015	1716 – 2252	moderate rain	
1-June-2015	0145 – 1227	moderate rain	

CHAPTER 3

SIGNAL PROCESSING ALGORITHM DESCRIPTION

This chapter details the signal processing algorithms used in the Low-power Phased Array Radar (LPAR) system. The chapter begins with a brief review of the fundamentals of random processes for radar In-phase and Quadrature (IQ) data and autocovariance processing techniques. These concepts will then be extended to describe the *pulse-pair processing* algorithm used to estimate the weather signal moments and polarimetric products. For the remainder of this document, the term *moments* refers to the principal moments of received voltage samples, namely power (as reflectivity), velocity, and spectral width. Polarimetric products are the set of estimates, including the moments, which are derived from dual-polarized received voltage samples. This chapter also describes the different methods of statistical estimation and analysis used frequently in the radar software, as well as a novel method for noise estimation for phased array weather radars having adaptive waveform or scan patterns. Most of these algorithms are adapted from textbook algorithms [37, 15] or from publicly-available system descriptions [40, 28] and adapted for use in a phased array radar.

3.1 Covariance and Correlation of Random Processes

3.1.1 Theoretical Formulation

A *random process* (also known as a *stochastic process*) is defined [69] as a collection of random variables that are indexed by time or space. For a time-varying

random process, $x_i(t)$, the following equations define the mean, autocovariance, and autocorrelation. The *mean* is given by

$$m_i(t) = \mathrm{E}\left[x_i(t)\right] \tag{3.1.1}$$

Where $\mathrm{E}\left[x_i(t)\right]$ is the Expected Value of $x_i(t)$. The *covariance* describes the joint moment between two time samples, $x_i(t)$ and $x_j(t+v)$, as [89]

$$\mathrm{Cov}\left[x_i(t), x_j(t+v)\right] = C_{ij}(v) = \mathrm{E}\left[\left(x_i(t) - m_i(t)\right)\left(x_j(t+v) - m_j(t+v)\right)^*\right] \tag{3.1.2}$$

Where $*$ denotes the complex conjugate. The covariance function measures the extent to which two random variables, in this case samples of $x_i(t)$ and $x_j(t)$ at two time instances t and $(t+v)$, co-vary in time. Two other terms can be derived from the mean and covariance, the *variance* and *correlation*. The *variance* of $x_i(t)$ is equal to the covariance when $t_1 = t_2$,

$$\mathrm{Var}\left[x_i(t)\right] = \sigma^2(x) = \mathrm{E}\left[\left(x_i(t) - m_i(t)\right)^2\right] = C_{ii}(0). \tag{3.1.3}$$

The *correlation* is simply the covariance normalized by the standard deviation of the time series,

$$R_{ij}(v) = \mathrm{E}\left[x_i(t)x_j(t+v)^*\right] = \frac{C_{ij}(v)}{\sqrt{C_{ii}(0)C_{jj}(0)}}. \tag{3.1.4}$$

Together, the mean, covariance, variance, and correlation coefficient terms are used to characterize the random process $x(t)$. In the case where the timeseries $x_i(t)$ and $x_j(t)$ are identical $(i = j)$, the terms in (3.1.2) and (3.1.4) are referred to as the auto-covariance and auto-correlation, respectively. Otherwise, they are known as the cross-covariance and cross-correlation. Two timeseries, $x_i(t)$ and $x_j(t)$ are said to be *uncorrelated* if their covariance, $C_{ij}(v)$, equals zero for all v.

3.1.2 Sample Covariance and Correlation Functions

Extending the previous discussion to a practical application, this section presents the necessary equations for calculating the covariance and correlation of a set of discrete time samples. For a timeseries x_i made up of M scalar observations, the sample mean is computed as

$$\hat{\mu}_i = \sum_{m=0}^{M-1} x_i\,[m] \tag{3.1.5}$$

Where the *hat* accent denotes that $\hat{\mu}_i$ is an estimate of the sample mean. Similarly, the sample variance of x_i is defined as

$$\hat{\sigma}_{ij}(v) = \frac{1}{M-1} \sum_{m=0}^{M-1} \left| x_i\,[m] - \mu_i \right|^2 \tag{3.1.6}$$

The sample correlation between two timeseries x_i and x_j is given as

$$\hat{R}_i j(v) = \frac{1}{M} \sum_{m=0}^{M-1} x_i\,[m]^*\, x_j\,[m+v] \tag{3.1.7}$$

The sample covariance can be calculated by first subtracting the means from x_i and x_j in (3.1.7). Note that the choice of normalization factors in 3.1.6 and (3.1.7) must be carefully considered. Normalization by $(M-1)$ for a lag-0 estimate (or $(M-|m|)$ for a lag-m estimate) is known as an *unbiased* estimator, while normalization by M results in a *biased* estimator. Traditionally, the variance is defined using the unbiased estimator, unless otherwise stated. When computing the sample covariance, the variance of the biased estimator can be shown to be *positive definite* and have a smaller mean square error than the unbiased estimator [89]. However, the biased estimator is, on average, too small by a factor $M/(M-v)$ [103], which becomes significant only at large lags ($v \approx M$). In this work, the variance is calculated using the unbiased estimator, and the sample covariance or correlation is computed from the biased estimators.

3.2 Statistical Properties of Received Voltage Samples

At the output of the Digital Down-Converter (DDC), the voltage samples from weather signals in a single resolution cell are a composite of radar echoes from each scatterer in the volume, expressed as

$$V(nT_s) = \frac{1}{\sqrt{2}} \sum_i A_i W_i e^{\gamma_i} \tag{3.2.1}$$

Where T_s is the radar Pulse Repetition Time (PRT), A_i is the scattering amplitude from the ith scatter, and W_i is a weighting factor resulting from array pattern or receiver filtering. Here, γ_i is the received phase from the ith scatterer

$$\gamma_i = \frac{4\pi r_i}{\lambda} + \frac{4\pi v_i n T_s}{\lambda} - (\psi_s + \beta_i) \tag{3.2.2}$$

Where r_i and v_i are the scatterer true range and radial velocity, respectively, ψ_s is the phase shift upon scattering, and β_i is any phase shift resulting from the weighting factor, W_i. The collective phase shift, $\psi_s + \beta_i$, from all scatterers in a resolution volume, gives rise to a differential phase shift in backscattered echoes received at the radar. The received phase of signals will undergo a phase shift from both the two-way propagation and phase shift upon scattering at each radar resolution cell, which is expressed as

$$\Phi_{DP} = 2 \int_0^{r_0} [k_h(r) - k_v(r)] dr + \Phi_{DS}. \tag{3.2.3}$$

Here, $k_h(r)$ and $k_v(r)$ are the free-space propagation constants in both H- and V-polarization, respectively. It's evident from 3.2.3 that estimation of differential phase from radar measurements will inherently estimate both the propagation and backscatter phase shift terms.

The output voltage samples are traditionally expressed as the real and imaginary components of (3.2.1)

$$V(nT_s) = |V(nT_s)| \cos(\theta(nT_s)) + j\,|V(nT_s)| \sin(\theta(nT_s)) \tag{3.2.4a}$$

$$V(nT_s) = I(nT_s) + jQ(nT_s). \tag{3.2.4b}$$

These are known as the radar In-phase and Quadrature (IQ) samples. The composite amplitude and phase of (3.2.1) have been expressed in $|V(nT_s)|$ and $\theta(nT_s)$, respectively. These voltage samples can be simplified by applying the Central Limit Theorem to the collection of precipitation scatterers in the resolution volume. The Central Limit Theorem states [69, 37] that the arithmetic sum of a large number of independent random variables, each with well-known expected value and variance, will approach a normal distribution. Since the resolution volume is large compared to each raindrop, and the range to the center of the resolution volume is large compared to the relative distance between drops, the received composite phase will have a uniform distribution in the interval $[-\pi, \pi]$. Power estimates ($\hat{S}$), proportional to $I^2 + Q^2$, will have an exponential probability density function of the form

$$p(\hat{S}) = \frac{1}{2\sigma^2} \exp\left(-\frac{\hat{S}}{2\sigma^2}\right) \tag{3.2.5}$$

Where the mean power ($\overline{S}$) is equal to $2\sigma^2$, and σ is the standard deviation. In addition, we also assume that the voltage samples have a Gaussian-shaped Doppler spectrum, modeled as [37, p. 96]

$$S(v) = \frac{\overline{S}}{\sigma_v\sqrt{2\pi}} \exp\left[-\frac{(v-\overline{v})^2}{2\sigma_v^2}\right] \tag{3.2.6}$$

where $S(v)$ is the Doppler velocity spectrum at velocity v, $\overline{v}$ is the mean velocity, and σ_v is the spectral width. Since the power spectrum is the Discrete Fourier Transform

(DFT) of the autocorrelation, the autocorrelation function for (3.2.6) is given directly as [15, p. 253]

$$R(\tau) = \overline{S} \exp\left[\frac{-8\pi^2\sigma_v^2\tau^2}{\lambda^2}\right] \exp\left[-j\frac{4\pi\overline{v}\tau}{\lambda}\right] \tag{3.2.7}$$

where $R(\tau)$ is the value of the correlation at lag τ. For radar data having a uniform PRT of T_s seconds, $R(\tau)$ represents the signal correlation at discrete time intervals, $R[mT_s]$, where m is the received pulse index. The co-polor correlation terms ($\hat{R}_h^n$) from (3.4.2) can therefore be approximated by

$$R_h^n[mT_s] = S_h \exp\left[\frac{-8\pi^2\sigma_v^2\left(mT_s\right)^2}{\lambda^2}\right] \exp\left[-j\frac{4\pi\overline{v}mT_s}{\lambda}\right] \tag{3.2.8}$$

Using (3.2.8), the correlation coefficient can be expressed as

$$\rho[mT_s] = \exp\left[\frac{-8\pi^2\sigma_v^2\left(mT_s\right)^2}{\lambda^2}\right] \exp\left[-j\frac{4\pi\overline{v}mT_s}{\lambda}\right]. \tag{3.2.9}$$

To model Additive White Gaussian Noise (AWGN) in the channels, Bringi and Chandrasekar [15] suggest multiplying (3.2.9) by an additional factor to estimate the noise-contaminated correlation coefficient

$$\rho_{S+N}[mT_s] = \rho[mT_s]\left[(1+\mathrm{SNR}_h^{-1})(1+Z_{dr})\right]^{-1/2}. \tag{3.2.10}$$

Where SNR_h and Z_{dr} are the (linear) H-polarization Signal to Noise Ratio and differential reflectivity, respectively. Equation (3.2.10) is valid for both single- and dual-polarization modes of operation, provided that the PRT properly represents the time lag between co-polar estimates.

3.3 Radar Range Equation for Volume Targets

As received weather signals can be approximated by volumetric targets, the radar range equation for weather signals is given by [37]

$$\mathrm{SNR} = \frac{P_t G_t G_r c\tau\pi^3\theta\phi\,|K_w|^2\,Z_e}{1024\ln 2\lambda^2 N_p r^2} \tag{3.3.1}$$

Where P_t is the transmitted peak power, G_t and G_r are the transmit and receive antenna gains, c is the speed of light, τ is the (uncompressed) pulsewidth, θ and ϕ are the half-power beamwidths in azimuth and elevation, K_w is the dielectric factor of water ($|K_w|^2 \approx 0.9$), Z_e is the equivalent reflectivity factor, λ is the wavelength, N_p is the noise power out of the receiver, r is the range to the center of the resolution volume, and the Signal to Noise Ratio (SNR) is referenced to the receiver output. The output noise power is equal to the system gain multiplied by the noise at the input to the system, $kTBl_f$, where kT is the noise spectral density at the receiver input ($\approx$4E$-$21 W Hz^{-1} at 290 K), B is the receiver bandwidth, and l_f is the system noise figure.

To account for pulse compression, (3.3.1) can be modified by introducing a pulse-compression gain term (G_c) and replacing the uncompressed pulsewidth with the compressed pulsewidth (τ_c). Because $G_c = \tau/\tau_c$ and $\tau_c = 1/B$, this form of the equation is identical to (3.3.1) for an ideal matched filter. However, in practice, the matched filter used in pulse compression is modified to reduce the range-sidelobes of the compressed waveform at the cost of decreased pulse compression gain. To account for loss in pulse compression gain due to non-ideal matched filters, an additional loss term, l_c, can be added. Replacing N_p with its derivation, the radar range equation referenced to the output of the pulse compression filter is given by

$$\mathrm{SNR} = \frac{P_t G_t G_r c\tau\pi^3\theta\phi\,|K_w|^2\,Z_e}{1024\ln 2\lambda^2 R^2 kTBl_f l_c}. \tag{3.3.2}$$

Since (3.3.2) takes pulse compression into account, the SNR is taken at the output of the pulse compression filter.

Equation (3.3.2) assumes that the transmit/receive gains and beamwidths are all constant over the entire scan volume. Since phased array radars experience a beam broadening affect and resulting scan loss at angles away from boresight, scan dependence must be added to the gain (G_r and G_r) and beamwidth (θ and ϕ) terms in (3.3.2). For phased arrays employing different amplitude tapers during both transmit and receive, the two-way beamwidth can be approximated as the geometric mean of the beamwidths in both transmit and receive. In the azimuthal dimension, the two-way azimuth beamwidth can be approximated by

$$f_\theta(\theta,\phi) \approx \sqrt{\theta_t(\theta,\phi)\theta_r(\theta,\phi)} \tag{3.3.3}$$

Where θ_t and θ_r are the transmit and receive beamwidths at the array pointing angle (θ,ϕ). A similar expression for the elevation beamwidth, $f_\phi(\theta,\phi)$ can also be derived (not shown). The radar range equation for phased array radars, taken at the output of the pulse compression filter, is now given by

$$\mathrm{SNR} = \frac{P_t G_t(\theta,\phi) G_r(\theta,\phi) c\tau\pi^3 f_\theta(\theta,\phi) f_\phi(\theta,\phi) \left|K_w\right|^2 Z_e}{1024 \ln 2 \lambda^2 R^2 k T B l_f l_c}. \tag{3.3.4}$$

To get estimate the received weather reflectivity, (3.3.4) can be solved for Z_e to get an estimate for the radar reflectivity,

$$Z_e = \frac{\mathrm{SNR} 1024 \ln 2 \lambda^2 R^2 k T B l_f l_c}{P_t G_t(\theta,\phi) G_r(\theta,\phi) c\tau\pi^3 f_\theta(\theta,\phi) f_\phi(\theta,\phi) \left|K_w\right|^2}. \tag{3.3.5}$$

.

The weather radar sensitivity is taken as the reflectivity range profile for 0 dB SNR, which can be found by setting SNR = 1 in (3.3.5).

3.4 Pulse Pair Processing Technique

Dual-polarization is a radar system architecture and scanning strategy that observes radar returns in two orthogonal polarizations. In the Alternate Transmit/Alternate Receive (ATAR) polarization pulsing scheme, the transmit and receive polarization state is changed from H-polarization to V-polarization after a single transmit or receive action [100]. For a series of M consecutive pulses in a radial, the received voltage can be written as

$$V[m] = \{V_{hh}[0], V_{vv}[1], V_{hh}[2], ..., V_{hh}[M-2], V_{vv}[M-1]\} \tag{3.4.1}$$

Where the subscript hh denotes transmission in H-polarization and reception in H-polarization. Weather moments and polarimetric products are calculated using algorithms for alternating polarized pulses as described by Bringi and Chandrasekar [15] or Doviak and Zrnić [37]. Assuming a uniform PRT between voltage samples in (3.4.1), the co-polar correlation terms for the signal powers (or autocorrelation at lag-0) and higher order time lags are estimated from the complex voltage timeseries via

$$\hat{S}_h = \hat{R}^0_{hh} = \frac{1}{M}\sum_{m=0}^{M-1} |V_{hh}[2m]|^2 - \hat{N}^h_p \tag{3.4.2a}$$

$$\hat{S}_v = \hat{R}^0_{vv} = \frac{1}{M}\sum_{m=0}^{M-1} |V_{vv}[2m+1]|^2 - \hat{N}^v_p \tag{3.4.2b}$$

$$\hat{R}^n_{hh} = \frac{\sum_{m=0}^{M-1} V_{hh}[2m]^* V_{hh}[2m+2n]}{\sum_{m=0}^{M-1} w[2m]^* w[2m+2n]} \tag{3.4.2c}$$

$$\hat{R}^n_{vv} = \frac{\sum_{m=0}^{M-1} V_{vv}[2m+1]^* V_{vv}[2m+1+2n]}{\sum_{m=0}^{M-1} w[2m+1]^* w[2m+1+2n]}. \tag{3.4.2d}$$

Where $\hat{N}_p^{h,v}$ are the noise estimates in the H- and V-channels, respectively, $\hat{R}_{h,v}^n$ represents the lag-n co-polar correlation, and the asterisk denotes the complex conjugate. These equations are generalized for the use of an arbitrary window, w, applied to the data [28]. Data windowing is useful for reducing spectral leakage in the covariance estimators and in computing the DFT, especially for small time intervals. For the purposes here, a uniform rectangular window is used and the denominators in (3.4.2c) and (3.4.2c) reduce to M. In a similar fashion, the cross-polar covariance terms can be computed from

$$\hat{R}_{hv}^n = \frac{\sum_{m=0}^{M-1} V_{hh}[2m]^* V_{vv}[2m+n]}{\sum_{m=0}^{M-1} w[2m]^* w[2m+n]} \tag{3.4.3a}$$

$$\hat{R}_{vh}^n = \frac{\sum_{m=0}^{M-1} V_{vv}[2m+1]^* V_{hh}[2m+1+n]}{\sum_{m=0}^{M-1} w[2m+1]^* w[2m+1+n]}. \tag{3.4.3b}$$

To visualize the covariance terms from a pulse sequence, Figures 3.1a and 3.1b show diagrams of the ATAR polarization scheme for both a uniform and staggered Pulse Repetition Frequency (PRF), respectively. Additionally, Figure 3.1c demonstrates the single-polarization, staggered PRF case. Since the effective PRF per polarization is half that in polarimetric ATAR as compared to a single-polarization sequence, the unambiguous velocity is therefore reduced as well. To overcome this deficiency, operational radars typically vary the PRT on successive pulses, which allows the unambiguous velocity to be extended. Where applicable, the pulse-pair processing equations below detail both the uniform and staggered PRF forms.

Reflectivity in the ATAR mode is similarly defined as in single-polarization or polarimetric Simultaneous Transmit/Simultaneous Receive (STSR) [77] radars as the

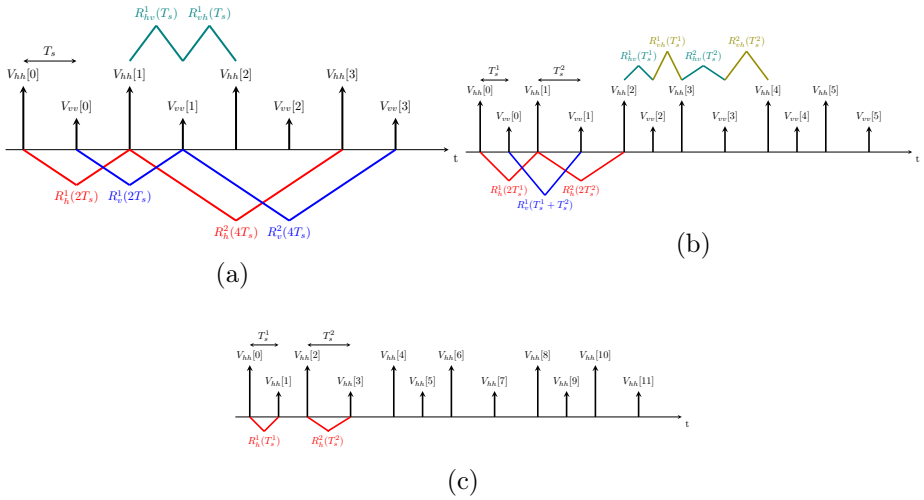

Figure 3.1: Pulsing schemes for the LPAR system, showing correlation terms gathered for dual-polarized (a) uniform PRF and (b) dual-polarized staggered PRF modes of operation. Also shown is the single-polarization scheme for (c) staggered PRF.

equivalent reflectivity in H-polarization. Simplifying from (3.3.5), reflectivity is calculated as

$$\hat{Z}_h = \hat{Z}_e = C_h(\theta, \phi) + \mathrm{SNR}_h \tag{3.4.4}$$

Where $C_h(\theta, \phi)$ is the system calibration constant, which includes the array calibration and range dependence terms in (3.3.5), and SNR_h is the Signal to Noise Ratio in the H-channel.

$$\mathrm{SNR}_h = 10 \log_{10} \left[\frac{\hat{S}_h}{\hat{N}_h} \right]. \tag{3.4.5}$$

The Signal to Noise Ratio in the V-channel (SNR_v) is defined in a similar fashion. Radial velocity ($\hat{v}$) is computed from the H-channel data at a uniform PRF as

$$\hat{v} = \hat{v}_h = -\frac{\lambda}{4\pi T_s} \arg \left[\hat{R}_h^1 \right]. \tag{3.4.6}$$

Velocity (v) can also be estimated from staggered PRF samples (see Figures 3.1b and 3.1c) in either single- or dual-polarization as

$$\hat{v} = \hat{v}_h = -\frac{\lambda}{4\pi \left| T_s^2 - T_s^1 \right|} \arg \left[\frac{\hat{R}_h^1}{\hat{R}_h^2} \right]. \tag{3.4.7}$$

In the staggered PRF case, care must be taken when choosing the ratio between PRTs. Typically, a ratio of 2:3 is recommended [37]. For example, with a uniform PRF of 3 kHz, the unambiguous velocity is just 12.0 m s^{-1}. With a staggered PRF at 2.4 kHz and 3.2 kHz, the Nyquist velocity is improved to 18 m s^{-1}. In addition, whereas radial velocity is traditionally taken in H-polarization, it can also be computed from the average across both the H- and V-channel velocities

$$\hat{v} = \frac{1}{2} \left(\hat{v}_h + \hat{v}_v \right). \tag{3.4.8}$$

Spectral width (σ_v) is calculated from the co-polar correlation terms for uniform PRF via

$$\hat{\sigma}_v = \frac{\lambda}{2\pi T_s \sqrt{2}} \left| \ln \left(\frac{\hat{S}_h}{\left| \hat{R}_h^1 \right|} \right) \right|^{1/2} \operatorname{sgn} \left[\ln \left(\frac{\hat{S}_h}{\left| \hat{R}_h^1 \right|} \right) \right] \tag{3.4.9}$$

Here, spectral width is estimated from H-channel data. Similar to (3.4.7), spectral width can also be estimated for a staggered PRF sequence as

$$\hat{\sigma}_v = \frac{\lambda}{2\pi \sqrt{2 \left| \left(T_s^2 \right)^2 - \left(T_s^1 \right)^2 \right|}} \left[\ln \frac{\left| \hat{R}_h^1 \right|}{\left| \hat{R}_h^2 \right|} \right]^{1/2} \tag{3.4.10}$$

The spectral width can also be approximated from the lag-1 and lag-2 correlation terms at a uniform PRF via

$$\hat{\sigma}_v = \frac{\lambda}{2\pi T_s \sqrt{6}} \left| \ln \left(\frac{\hat{R}_h^1}{\left| \hat{R}_h^2 \right|} \right) \right|^{1/2} \operatorname{sgn} \left[\ln \left(\frac{\hat{R}_h^1}{\left| \hat{R}_h^2 \right|} \right) \right]. \tag{3.4.11}$$

Equation (3.4.11) assumes a Gaussian Doppler spectrum shape and contiguous pair samples. Practically, 3.4.11 is useful in certain applications because it does not depend on the received power, $\hat{S}_h$, which may be contaminated by external interference or second trip echoes.

Differential reflectivity (Z_{dr}) is calculated from the ratio of power measurements between the H- and V-channels. However, a polarimetric phased array employing separate channels for H-polarized and V-polarized signals will inherently have different calibration constants for each polarization and scan pointing angle. So, differential reflectivity is calculated from the ratio of calibrated power measurements for each channel. In this implementation, differential reflectivity is calculated from the difference between measured reflectivities in each polarization, minus a bias term

$$\hat{Z}_{dr} = \hat{Z}_h - \hat{Z}_v - \Delta Z_{dr}(\theta, \phi). \tag{3.4.12}$$

To further reduce bias errors in $\hat{Z}_{dr}$, measurements of precipitation types having low space-time variability of differential reflectivity is used to estimate the bias correction term ($\Delta Z_{dr}(\theta, \phi)$). Radar data at high SNR (>20 dB) from dry, aggregated snow or light rain below the bright band are used to estimate the bias [47] at each scan pointing angle.

Differential phase (Φ_{DP}), which includes the effect of differential propagation phase shift through the rain medium (ψ_s) and backscatter differential phase from the scatterers in the resolution volume (β_i), is computed from the cross-polar correlation terms as

$$\hat{\Phi}_{DP} = \frac{90}{\pi} \arg\left[\hat{R}^1_{hv}(\hat{R}^1_{vh})^*\right] - \Delta\Phi_s(\theta, \phi). \tag{3.4.13}$$

Here, $\Delta\Phi_s(\theta, \phi)$ is the system phase offset estimated and manually updated from differential phase measurements in light rain at high SNR (>20 dB), where differential propagation and backscatter phase are negligible. To account for phase wrapping, the procedure described by Wang and Chandrasekar [116] is used to unfold and correct $\hat{\Phi}_{DP}$ estimates. At each radial, the unfolding algorithm searches for the first area of *valid* Φ_{DP}, defined as an upper limit on the standard deviation of differential phase (SD(Φ_{DP})) and lower limit on the mean ρ_{hv} within a moving range bin kernel.

Variations in the estimation of this valid area can cause minute changes in the starting differential phase between radials. Copolar correlation coefficient is calculated using a lag-0 estimator as

$$\hat{\rho}_{hv} = \frac{1}{2} \frac{\left|\hat{R}^1_{hv}\right| + \left|\hat{R}^1_{vh}\right|}{\sqrt{\hat{S}_h \hat{S}_v} \left[\left|\hat{R}^1_h\right| / \hat{S}_h\right]^{0.25}}. \tag{3.4.14}$$

Due to the use of ATAR, the effective co-polar PRF is half of that compared to a similar STSR system. This results in a lower unambiguous velocity interval (v_a) which can cause severe aliasing in the presence of fast-moving weather. For an X-band radar (9410 MHz) pulsing at a PRF of 3 kHz, the co-polar unambiguous velocity is just $12\,\mathrm{m\,s^{-1}}$. Techniques to increase the unambiguous velocity include the use of staggered PRT pulse sequences [113, 49] (as described previously), batches of pulse sequences at different PRFs [9], or velocity retrieval from cross-polar estimates [37]. Staggered PRT techniques can impose difficulties in ground clutter filtering and reduce the number of pulse-pair estimates for cross-correlation terms in the ATAR mode. For this implementation, a uniform PRF pulsing scheme is used, and $\hat{\Phi}_{DP}$-based velocity is computed via

$$\hat{v}_p = \frac{\lambda}{4\pi T_s} \arg\left[\hat{R}^1_{hv} \exp(-j\hat{\Phi}_{DP})\right]. \tag{3.4.15}$$

Equation (3.4.15) can also be calculated from the summation of the cross-polar covariance terms

$$\hat{v}_p = \frac{\lambda}{4\pi T_s} \arg\left[\hat{R}^1_{hv} \hat{R}^1_{vh})\right]. \tag{3.4.16}$$

In either form of the cross-polar velocity, the covariance terms must be unfolded and unwrapped beforehand. The disadvantage with this technique, however, is that it requires accurate calibration of the system phase offset. As the phase offset is traditionally determined at run-time from radial estimates [116], the cross-polar velocity

estimate is prone to errors if low SNR or poor co-polar correlation coefficient is present at the leading edge of storms.

3.4.1 Ancillary Variables

Beyond the standard set of weather moments and polarimetric products, the radar system also computes several variables which are useful in specialized classification and estimation algorithms. Spatial texture fields have recently been used in Hydrometeor Classification Algorithms (HCAs) as an effective means to distinguish between meteorological, biological, and clutter echoes [23]. The Weather Surveillance Radar (WSR-88D) HCA [88] use the spatial textures of reflectivity and differential phase in the fuzzy logic classification scheme. Here, the spatial texture of reflectivity ($\mathrm{SD}(\hat{Z}_h)$) is computed from the difference between raw and smoothed estimates within a rolling range window,

$$\mathrm{SD}(\hat{Z}_h) = \sqrt{\frac{\sum\limits_{1\,\mathrm{km}} \left(\bar{Z}_h - \hat{Z}_h\right)}{n_z}} \tag{3.4.17}$$

Where $\bar{Z}_h$ is the mean value of $\hat{Z}_h$ in a 1 km moving range window and n_z is the number of estimates within the range window kernel. Texture of differential phase ($\mathrm{SD}(\hat{\Phi}_{DP})$) is similarly computed using a 2 km moving range window. Gourley et al. [52] uses an alternate definition for the spatial texture of reflectivity as the Root Mean Square (RMS) difference between a Cell-Under-Test (CUT) and a window of neighboring cells

$$\mathrm{TDBZ}_{m,n}(r,g) = \sqrt{\frac{\sum\limits_{i=-(m-1)/2}^{(m-1)/2} \sum\limits_{j=-(n-1)/2}^{(n-1)/2} (x[r,g] - x[r+i, g+j])^2}{mn}} \tag{3.4.18}$$

Where $x[r,g]$ is the CUT at radial r and range gate g centered in a two-dimensional window of $[m,n]$ neighboring resolution cells.

The spatial texture in (3.4.18) is a sub-class of image processing texture analysis methods known as *rank filters* [5]. Rank filters are a broad class of nonlinear image filters which select the value of a cell based on the rank, or ordering, of a neighborhood of cells. *Range filters* are a rank filtering technique which compute the rank of the difference between the CUT and neighborhood cells. For the ith neighborhood cell (f_i) about the CUT (f_0) the range filter computes the difference

$$\text{range}(i) = f_0 - f_i. \tag{3.4.19}$$

The value taken at the CUT is taken as a specific rank value of the computed neighborhood range, typically the median. Ranks above or below the median have the effect of shifting the edges of features in the scene [55]. With the range filter in mind, a new feature field can be defined, known as the Median-Range texture field (MR)

$$\text{MR}_{m,n}^{l,k}(r,g) = \text{median}\left\{x[r,g] - x[r+i, g+j]\right\} \tag{3.4.20}$$

Where m and n define the neighborhood of cells, and l and k are the guard cells about the CUT in the radial and gate dimensions, respectively,

$$\begin{aligned} i &= -\frac{(m-1)}{2} \ldots \frac{(m-1)}{2},\ |i| > \frac{(l-1)}{2} \\ j &= -\frac{(n-1)}{2} \ldots \frac{(n-1)}{2},\ |j| > \frac{(k-1)}{2}. \end{aligned}$$

Hubbert et al. [58] uses (3.4.18) as a feature field for clutter identification, along with the Clutter Phase Alignment (CPA). CPA is a measure of the temporal phase variability of radar echoes, and is computed from the ratio of coherent to non-coherent received signal power

$$\mathrm{CPA} = \frac{\left|\sum_{m=0}^{M-1} V_{hh}[m]\right|}{\sum_{m=0}^{M-1} |V_{hh}[m]|} \tag{3.4.22}$$

CPA and TDBZ are useful in the classification of clutter from meteorological echoes. In the presence of clutter, values of CPA and TDBZ generally exceed 0.6 and 20 dBZ, respectively. For weather, these values tend to be much lower [58]. Another useful feature field for clutter identification is the SPIN value, which is a measure of how often the reflectivity gradient changes sign along a radial. The SPIN at each range cell is first computed by assigning a positive unary value if the following two conditions are met for three consecutive range cells in a radial at positions $(g-1)$, g, and $(g+1)$, respectively,

$$\mathrm{sign}\left(Z_h\left[g\right] - Z_h\left[g-1\right]\right\} = -\mathrm{sign}\left\{Z_h\left[g+1\right] - Z_h\left[g\right]\right) \tag{3.4.23a}$$

$$\frac{\left|Z_h\left[g\right] - Z_h\left[g-1\right]\right| + \left|Z_h\left[g+1\right] - Z_h\left[g\right]\right|}{2} > spin_{thres}. \tag{3.4.23b}$$

Where $spin_{thres}$ is a reflectivity threshold. The SPIN value is then taken as the average SPIN number within a window of m radials and n gates, normalized by the total kernel size (mn).

Another variable computed is the Signal Quality Index (dB) (SQI), also known as the Normalized Coherent Power (dB) (NCP). SQI has been used in quality control algorithms to help threshold regions of poor quality data and identify presence of clear air speckle or other artifacts [27, 118]. SQI is defined as the magnitude of the H-polarization lag-1 correlation coefficient

$$SQI_h = \frac{\left|\hat{R}_{hh}^1\right|}{\hat{S}_h} \tag{3.4.24}$$

When running in dual-polarization modes, SQI is taken as the average of the H- and V-polarization SQI values.

Table 3.1: Overview of pulse pair processing estimators and computed variables in the LPAR signal processor.

Product	Symbol	Uniform PRT	Staggered PRT
Reflectivity (H-pol.)	Z_h	$\hat{Z}_h = C_h(\theta,\phi) + \mathrm{SNR}_h$	
Co-polar Radial Velocity	v	$-\frac{\lambda}{4\pi T_s}\arg\left[\hat{R}_h^1\right]$	$-\frac{\lambda}{4\pi\lvert T_s^2 - T_s^1\rvert}\arg\left[\frac{\hat{R}_h^1}{\hat{R}_h^2}\right]$
Cross-polar Radial Velocity	v_p	$\frac{\lambda}{4\pi T_s}\arg\left[\hat{R}_{hv}^1\exp(-j\hat{\Phi}_{DP})\right]$	
Spectral Width	σ_v	$\frac{\lambda}{2\pi T_s\sqrt{6}}\left\lvert\ln\left(\frac{\hat{R}_h^1}{\lvert\hat{R}_h^2\rvert}\right)\right\rvert^{1/2}\mathrm{sgn}\left[\ln\left(\frac{\hat{R}_h^1}{\lvert\hat{R}_h^2\rvert}\right)\right]$	$\frac{\lambda}{2\pi\sqrt{2\lvert(T_s^2)^2-(T_s^1)^2\rvert}}\left[\ln\frac{\lvert\hat{R}_h^1\rvert}{\lvert\hat{R}_h^2\rvert}\right]^{1/2}$
Signal Quality Index	SQI	$\frac{1}{2}\left(\frac{\lvert\hat{R}_{hh}^1\rvert}{\hat{S}_h} + \frac{\lvert\hat{R}_{vv}^1\rvert}{\hat{S}_v}\right)$	
Differential Reflectivity	Z_{dr}	$\hat{Z}_h - \hat{Z}_v - \Delta Z_{dr}(\theta,\phi)$	
Copolar Correlation Coefficient	ρ_{hv}	$\frac{1}{2}\frac{\lvert\hat{R}_{hv}^1\rvert+\lvert\hat{R}_{vh}^1\rvert}{\sqrt{\hat{S}_h\hat{S}_v}\left[\lvert\hat{R}_h^1\rvert/\hat{S}_h\right]^{0.25}}$	
Differential Phase	Φ_{DP}	$\frac{90}{\pi}\arg\left[\hat{R}_{hv}^1(\hat{R}_{vh}^1)^*\right] - \Delta\Phi_s$	
Spatial Texture of Reflectivity	$\mathrm{TDBZ}_{m,n}$	$\sqrt{\frac{\sum_{i=-(m-1)/2}^{(m-1)/2}\sum_{j=-(n-1)/2}^{(n-1)/2}(x[r,g]-x[r+i,g+j])^2}{mn}}$	
SPIN	$\mathrm{SPIN}_{m,n}$	$\sum_m\sum_n\left(\begin{array}{c}\{\mathrm{sign}\left(Z_h[g]-Z_h[g-1]\right)=-\mathrm{sign}\left(Z_h[g+1]-Z_h[g]\right)\}\,\& \\ \left\{\frac{\lvert Z_h[g]-Z_h[g-1]\rvert+\lvert Z_h[g+1]-Z_h[g]\rvert}{2} > spin_{thres}\right\}\end{array}\right)\Big/mn$	
Clutter Phase Alignment	CPA	$\frac{1}{2}\left(\frac{\left\lvert\sum_{m=0}^{M-1}V_{hh}[m]\right\rvert}{\sum_{m=0}^{M-1}\lvert V_{hh}[m]\rvert} + \frac{\left\lvert\sum_{m=0}^{M-1}V_{vv}[m]\right\rvert}{\sum_{m=0}^{M-1}\lvert V_{vv}[m]\rvert}\right)$	
Texture of Reflectivity	$\mathrm{SD}(Z_h)$	$\sqrt{\frac{\sum_{1\,\mathrm{km}}\left(\bar{Z}_h-\hat{Z}_h\right)}{n_z}}$	
Texture of Differential Phase	$\mathrm{SD}(\Phi_{DP})$	$\sqrt{\frac{\sum_{2\,\mathrm{km}}\left(\bar{\Phi}_{DP}-\hat{\Phi}_{DP}\right)}{n_\Phi}}$	

3.5 On the Use of Threshold Detection

The LPAR uses a simple SNR threshold detection for both weather surveillance and display operation. In this section, useful formulae are presented which derive the probability of detection (P_d) and probability of false alarm (P_{fa}) for a set threshold level. Note that the LPAR also allows for a threshold detection from the copolar correlation coefficient (ρ_{hv}) as a lower limit, but this case is not handled here. For the incoherent integration of power estimates, each having an exponential probability density function as in (3.2.5), weather signals can be modeled as the Swirling II target model. The Swirling models classify a target type in terms of its fluctuation time (*scan-to-scan* or *pulse-to-pulse*) and Radar Cross Section (RCS) model (*exponential* density function as a collection of similar scatterers or *chi-squared* with one dominant scatterer). As the ensemble average of drops within the resolution volume approach an exponential density function and the decorrelation time on successive pulses is short relative to a Coherent Processing Interval (CPI), weather echoes can be approximated with a Swirling II target model. For a given SNR threshold (THR), the probability of detection is given by [99]

$$P_d = 1 - I\left[1 + \frac{10^{\mathrm{THR}/10}}{(1+10^{\mathrm{SNR}/10})\sqrt{M}}, M\right] \tag{3.5.1}$$

Where $I(u,p)$ is Pearson's form of the incomplete Gamma function

$$I(u,p) = \frac{1}{\Gamma(p+1)} \int_0^{u\sqrt{p+1}} t^p \exp[-t]dt. \tag{3.5.2}$$

Here, $\Gamma(a)$ is the complete gamma function, the threshold (THR) and SNR are relative to the estimated noise power (N_p), and the SNR is the single-pulse Signal to Noise Ratio. Curtis [33] derived an alternate form for this (3.5.1),

$$P_d = \Gamma_{inc}\left[\frac{M}{(1+10^{\mathrm{SNR}/10})}\left(1+10^{\mathrm{THR}/10}\right), M\right] \tag{3.5.3}$$

Equation (3.5.3) assumes the use of the *noise-removed* SNR, as in (3.4.5), whereas (3.5.1) does not. The threshold parameter can be set according to a desired probability of false alarm. For the incoherent integration of power estimates, Ivic et al. [61] derived the following relationship between THR and P_{fa}

$$P_{fa} = \Gamma_{inc}\left[M(1+10^{THR/10}), M\right] \tag{3.5.4}$$

Where $\Gamma_{inc}[u,p]$ is the incomplete Gamma function. Together, (3.5.1) and (3.5.4) express the radar probability of detection for a given threshold parameter for a measured single-pulse SNR. For example, a typical 0 dB threshold for 32 incoherently integrated pulses ($M = 32$) will yield a P_{fa} of 3.6E−6. Achieving a minimum P_d above 0.95 requires a minimum 4.7 dB SNR.

The previous analysis holds for the probability of detection and false alarm for a single range bin. If active weather is only declared for a feature if the SNR exceeds the threshold for M gates out of a possible N, the cumulative probability of detection ($P_d^{M/N}$) for the feature can be found from the formula for the binomial distribution [69]

$$P_d^{M/N} = \sum_{k=M}^{N} \frac{N!}{k!\,(N-k)!} P_d^k \left(1-P_d\right)^{(N-k)} \tag{3.5.5}$$

As an example, consider the following. The WSR-88D Storm Cell Identification and Tracking (SCIT) algorithm declares active weather in a radial weather if the reflectivity exceeds a given threshold (typ. 30 dBZ) within a range extent with no more than n_d dropouts [63]. If the minimum range extent is 1.7 km with a range resolution of 50 m (≈34 range bins) with no more than 2 dropouts, the probability of detection for the feature is just 48.7 % if the single-bin P_d is 95 %. If the range resolution is degraded to 250 m (≈7 range bins), this probability increases to 95.5 %. As the LPAR operates with a typical 50 m range resolution compared to the nominal 250 m

resolution on the WSR-88D, this demonstrates the importance of proper systems engineering when translating algorithms developed for one radar to another.

3.6 On the Generation of Radar Data with Gaussian Doppler Spectra

The goal of radar data simulation is to generate radar signals as IQ data samples that have a pre-determined Doppler spectrum shape, which can be approximated as a Gaussian model described by (3.2.6). To generate polarimetric IQ data having this Doppler power spectrum, a Finite Impulse Response (FIR) filter is used to scale and shape white noise. The procedure begins by generating complex AWGN for each polarization as

$$w_h = \mathcal{N}(0,1) \tag{3.6.1a}$$

$$w_v = \mathcal{N}(0,1)\,. \tag{3.6.1b}$$

Where N_p is the desired noise power level (W). To synthetically generate a pair of timeseries having a desired copolar correlation coefficient (ρ_{hv}), the V-polarization noise timeseries is synthetically correlated to the H-polarization timeseries via [29]

$$x_h = w_h \tag{3.6.2a}$$

$$x_v = \rho_{hv} w_h - \sqrt{(1-\rho_{hv}^2)}\, w_v. \tag{3.6.2b}$$

Next, the correlated noise sequences (x_h and x_v) are passed through a filter that has an Gaussian amplitude response with desired amplitude, velocity, and spectral width.

For a series of M consecutive pulses and a PRT of T_s seconds, the filter time-domain response is given by

$$h[mT_s] = \exp\left[\frac{-8\pi^2\sigma_v^2\left(mT_s\right)^2}{\lambda^2}\right]\exp\left[-j\frac{4\pi\overline{v}mT_s}{\lambda}\right] \tag{3.6.3}$$

Where m is the pulse index. Weather IQ data are then generated by passing the correlated noise samples through the filter

$$y_h = \mathcal{F}^-1\left[\mathcal{F}\left(x_h\right)\mathcal{F}\left(h\right)^*\right] \tag{3.6.4a}$$

$$y_v = \mathcal{F}^-1\left[\mathcal{F}\left(x_y\right)\mathcal{F}\left(h\right)^*\right] \tag{3.6.4b}$$

Where $\mathcal{F}$ and $\mathcal{F}^-1$ represent the DFT operations, respectively (commonly implemented using the Fast Fourier Transform (FFT)). To generate timeseries data with a desired SNR in each channel and differential power between channels, the output from (3.6.4) must be scaled appropriately by the desired SNR and noise power (N_p)

$$y_h = \sqrt{\frac{\mathrm{SNR}_h + N_p}{2}}y_h + \sqrt{\frac{N_p}{2}}\mathcal{N}\left(0,1\right) \tag{3.6.5a}$$

$$y_v = \sqrt{\frac{\mathrm{SNR}_h + N_p - Z_{dr}}{2}}y_v + \sqrt{\frac{N_p}{2}}\mathcal{N}\left(0,1\right) \tag{3.6.5b}$$

Where the desired SNR_h, noise power (N_p), and differential reflectivity (Z_{dr}) are linear. To generate timeseries with a specific reflectivity, the terms in (3.6.5) should be multiplied by the radar constant term from (3.3.5) for a particular set of waveform and radar parameters. A desired differential phase (Φ_{DP}) can be synthetically generated by shifting the phase of the H-polarization filter output

$$y_h = y_h\exp\left(j\Phi_{DP}\right). \tag{3.6.6}$$

The timeseries y_h and y_v now contain the correlated IQ samples for weather spectra having mean SNR, velocity, spectral width, copolar correlation coefficient, and differential phase.

CHAPTER 4

BUSHFIRE DETECTION AND MONITORING

Forest fires are an unavoidable necessity in many ecosystems. They allow for the regeneration of the local flora and support the biodiversity of the planet. However, these fires also pose significant risk to both local communities and the firefighters that protect them. From April to May 2013, an X-Band phased array radar deployed to South Australia to make polarimetric observations of prescribed burns and uncontrolled fires within and around the Adelaide Hills region. Analysis of the data collected indicate that areas of the smoke plume directly above the fire present different polarimetric signatures than those downwind. Based on these observations, an algorithm is proposed which distinguishes smoke plume observations from meteorological and clutter echoes and identifies areas with increased likelihood of being above or near active fire sources. The algorithm introduces a new spatial texture field, derived from the use of range filters, to identify areas in the smoke plume with increased ash and debris concentration, and storm cell tracking principles are used to track the motion of the smoke plume and estimate local wind direction. Results of the algorithm applied to untrained radar data collected from several bushfires are presented. Comparison against timelapse photography and local weather station data shows that the algorithm effectively identifies active fire sources and estimates the current wind direction.

4.1 Introduction

Dry summer months and high ground winds create a high risk of uncontrolled forest fires. Known as *bushfires* in Australia, these fires can spread quickly in certain terrains and meteorological conditions. The interaction between the fire, the terrain, and the local wind conditions can result in sudden changes in the fire direction and the creation of vortices [42]. Radar measurements can aid in understanding the fire morphology, and relaying that information to firefighters on the front line could reduce the loss of life and property. Forest fires are not just a problem in Australia, however. In the United States, increased periods of drought and hot, dry seasons are leading to a rapid escalation in forest fires. Since 1985, the cost to suppress wildland fires has more than quintupled to over $1.5 B [105, 104]. While many of these costs are due to an increased number of homes built near fire-prone areas, six of the most severe fires in the United States have occurred in the past decade since 2002 [51].

As the rate and extent of these fires grows, so does the risk to firefighters and emergency personnel. The Yarnell Hill Fire in June 2013 took the lives of nineteen firefighters when a rapid wind shift caused the fire to change direction suddenly [35]. Emergency personnel used the nearby Weather Surveillance Radar (WSR-88D) radar in Flagstaff, AZ during the fire both to predict wind shifts from observation of outflow boundaries and estimate smoke plume height. Fire behavior during forest fires, however, is still commonly estimated from visual observations and social media, remote aerial or satellite imagery [79], and fire behavior modeling [54].

As microwave radar systems have the capability to make observations over a large area, they are a useful source of information on fire morphology and have detected fire plumes since the 1950s. Birch [12] first reported cases in which weather radars in Australia have detected smoke plumes, and he cited two other detections in the United Kingdom and the US dating back to 1955 and 1961, respectively. Banta et al. [6] used an X-band Doppler radar to measure reflectivities from a forest fire

near Boulder, Colorado having reflectivities as high as 10 dBZ to 20 dBZ within the smoke plume. Jones and Christopher [65] analyzed data from an S-band radar and satellite imagery from a smoke and debris plume extending 100 km in range, having reflectivities near 20 dBZ at 5 km in height. Melnikov et al. [75] also studied the polarization characteristics from these fires. Although at S-band, they noted large, positive differential reflectivity, low copolar correlation coefficient, and high variances of differential phase and reflectivity measurements. Work has also been published to characterize the radar cross section of forest fire particulate and debris matter [46, 8].

This chapter is organized as follows. Sections 4.2 describes the test methodology used during the field campaign. Polarimetric observations and statistical analysis from the field campaign are presented in Section 4.3. Unlike most other reported measurements, raw data has been analyzed from a number of different burns and at close proximity to the fires. Additionally, during most other experiments and field studies the radars were located far away from the fire and hence only observed the plume at high altitudes above the heat source. This data was taken with the radar at close ranges to the bushfires and allowed for observations directly above the fire source. Based on the data analysis performed, an algorithm is proposed in Section 4.4 which uses fuzzy logic and storm cell tracking algorithms to detect areas above active fire sources. Section 4.5 presents results of the algorithm applied to an untrained data set from a prescribed burn. In situ wind measurements and timelapse photography are used to verify that the algorithm is effective at identifying potentially active fire areas and estimating the ambient wind direction.

4.2 Test Methodology

During April to May 2013, the X-band (9410 MHz) phased array radar system phased array radar system [84] made observations at seven separate bushfires over

Table 4.1: Prescribed burns and uncontrolled bushfire dates and locations.

Burn Site	Date	Area Burned (ha) (acres)	Ignition
Belair CP	4-April-2013	9.0 (22.2)	strip head
	5-April-2013	16.9 (41.8)	strip head
South Para Reservoir	10-April-2013	26.0 (64.2)	strip head
Barossa Reservoir	17-April-2013	47.6 (117.6)	aerial
Cleland CP	28-April-2013	10.0 (24.7)	strip head
Cox Scrub CP	1-May-2013	40.0 (98.8)	strip head
Kyeema CP	2-May-2013	39.6 (97.8)	strip head
Cherryville	9-May-2013	650 (1600)	uncontrolled
	10-May-2013	650 (1600)	uncontrolled

nine dates in and around the Adelaide Hills region in South Australia. Table 4.1 lists the attended bushfires, dates, and ignition type for each burn.

Prescribed bushfires are ignited in two ways: strip head or aerial. In strip head ignitions, firefighter personnel spark the fire using strip ignition patches. Aerial burns use a helicopter equipped with an ignited petroleum jelly dispenser to set the burn. One of the bushfires attended was an uncontrolled bushfire in Cherryville, while the rest were prescribed burns conducted by South Australian County Fire Services (CFS), Australian Department of Environmental, Water and Natural Resource (DEWNR), and South Australian Forestry Corporation (ForestrySA) personnel.

The phased array radar made Alternate Transmit/Alternate Receive (ATAR) dual polarized measurements at each burn [100]. During ATAR, the polarization of the transmitted pulse is alternated between horizontal and vertical, and a single receiver is used to receive the co-polarized signal. The measurements were made at a fixed Pulse Repetition Frequency (PRF) of 3 kHz, giving an effective PRF of 1.5 kHz per polarization. Three waveforms were used intermittently during each burn, having

range resolutions of 50 m, 15 m, and 7 m. The radar electronically-scanned at fixed elevations across a 90° sector, with intermittent Range-Height Indicator (RHI) and volumetric scans executed when the smoke plume intensity peaked. Clutter maps were also taken before and after each burn to be used as ground truth for comparative purposes.

Mobile weather stations provided local in situ measurements of the ambient environmental conditions near the burn for the uncontrolled bushfires and several of the larger prescribed burns. These provide up-to-date temperature, pressure, humidity, and wind velocity measurements. In addition, a camera mounted on the top of the radar system collected snapshots of the radar field-of-view, time synchronized with every azimuth scan collected.

The phased array radar system used for this research performs the *pulse pair processing* technique on received voltage samples. This technique is adapted from algorithms developed by Doviak and Zrnić [37] and Bringi and Chandrasekar [15]. See Chapter 3 for a description of the signal processing algorithms implemented.

4.3 Observations

4.3.1 Scattering Mechanism

Measurements of fallen ash and debris made at a prescribed burn at the Belair Conservation Park (CP) (5-April-2013) show that large debris particles consisted of either plate-like, leaf ash or complex debris from burnt grass and scrub. Plate-like particle matter samples, identified as Eucalyptus or Bracken Fern leaves, measured between 5 cm to 1 cm along its horizontal plane and less than 1 cm thick. Grass and other scrub debris samples were a complex spheroidal shape filled with rough, jagged edges and clusters measuring axial radii between 5 cm to 10 cm. These measurements agree with past work performed [6, 75].

4.3.2 Results

Figure 4.1 presents a snapshot of data at 06:14 Coordinated Universal Time (UTC) during the Cherryville uncontrolled bushfire (10-May-2013). Figure 4.1a shows the rising column of white smoke at 100 m to 400 m cross range, which correlates with the area of increased reflectivity in Figure 4.1b. Towards the right side of the photo, the smoke seems to disperse and become darker gray in color. The arrows in Figure 4.1b indicate the radar heading and current wind direction, showing that the smoke plume motion and direction is dominated by ambient ground winds.

The average radial velocity in Figure 4.1c confirms visual observations of the smoke drifting parallel or slightly away from the radar. Nearby weather stations monitored by the fire crews reported a North-Northeasterly wind (10°) at the time the data was taken. From Figure 4.1b and a radar heading of 150°, the smoke column appears to be drifting at a direction between 5° and 15°, which correlates well to the reported wind direction. We do notice some areas within the center of the smoke plume with zero radial velocity (≈60° wind direction), which may indicate the presence of fire-induced winds rather than ambient ground winds.

Comparison between Figure 4.1b and Figure 4.1d indicates correlation between higher reflectivity, lower differential reflectivity, and lower spectral width (not shown). Mean $\hat{Z}_h$ and $\hat{Z}_{dr}$ near [0.2, 2.0]km [cross range, down range] are 22 dBZ and 2 dB, respectively, while the mean values at [0.9, 2.2]km are 17 dBZ and 2.9 dB. Another patch of reduced differential reflectivity can also be seen at [1.1, 2.2]km. In addition, spectral width shows wide variation in the smoke plume returns, from 2.1 $\mathrm{m\,s^{-1}}$ near [0.2, 2.0]km to 1.3 $\mathrm{m\,s^{-1}}$ near [0.9, 2.2]km. In contrast, the copolar correlation coefficient in Figure 4.1e does not show any recognizable pattern or relationship with reflectivity, other than being randomly distributed with a low mean value of 0.4 within the smoke plume.

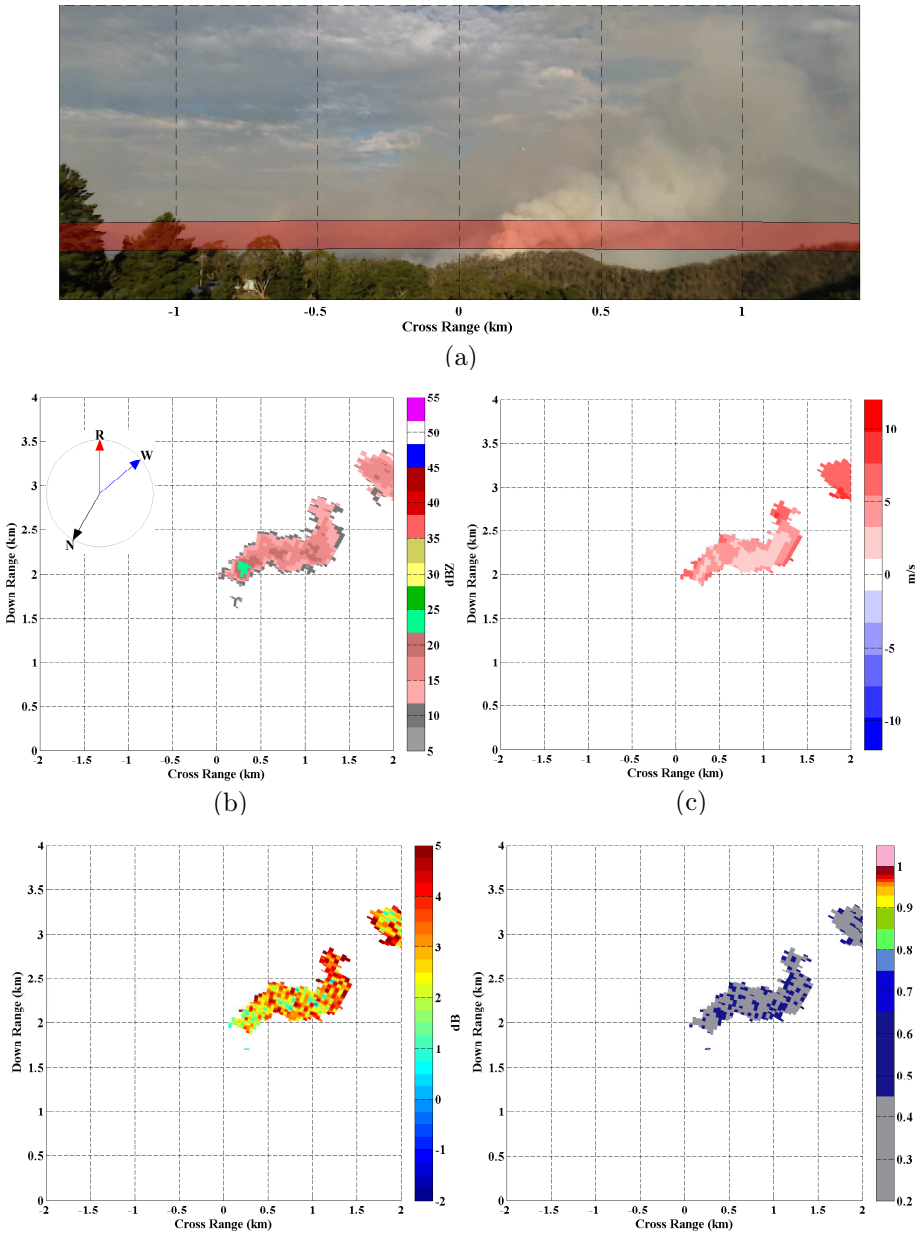

Figure 4.1: Timelapse photography and data from the Cherryville uncontrolled bushfire at 06:14 UTC. From top are (a) synchronized photography, (b) reflectivity (dBZ), (c) radial velocity ($\mathrm{m\,s^{-1}}$), (d) differential reflectivity (dB), and (e) copolar correlation coefficient. The red shaded area in (a) shows the radar field-of-view, using the radar 3 dB elevation beamwidth (2.8°). The arrows in (b) indicate due North (N), the radar heading (R), and measured wind directions (W).

Figure 4.2 shows data taken from a RHI scan during the Barossa Reservoir controlled burn (17-April-2013). Comparing the photo in Figure 4.2a to the reflectivity in Figure 4.2b, there is an area of increased reflectivity at a down range of 1.2 km

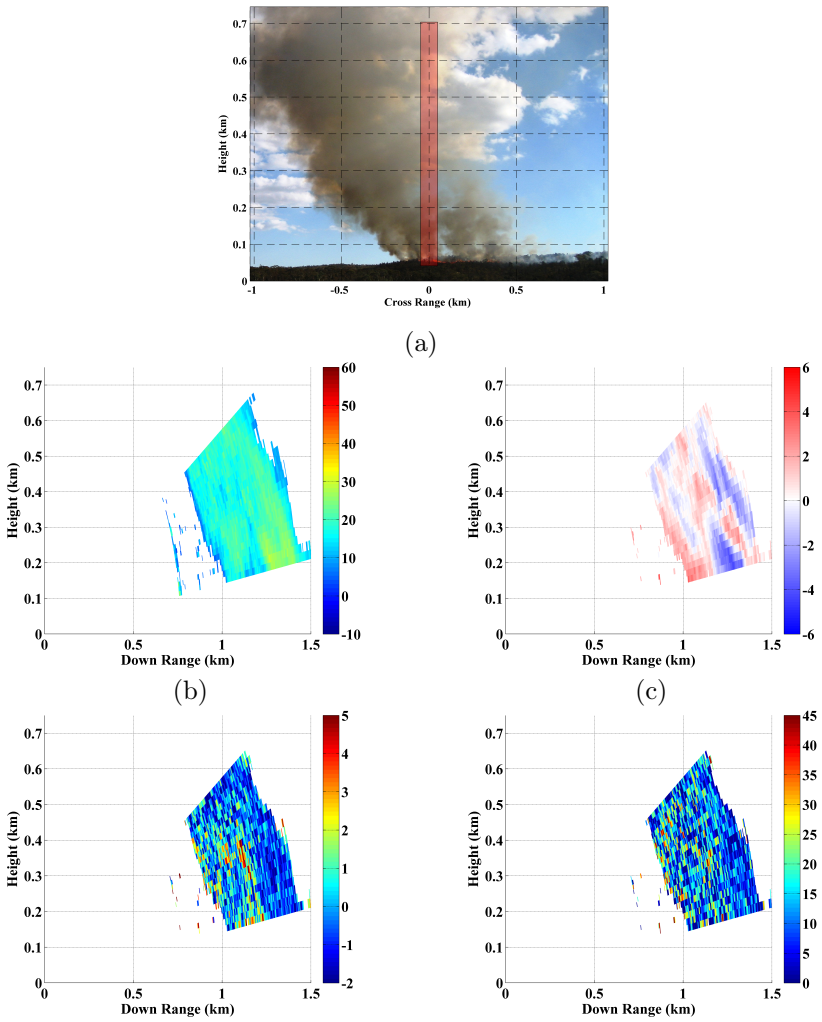

Figure 4.2: Timelapse photography and data from a RHI scan (22° elevation swath) from the Barossa Reservoir controlled burn at 06:03 UTC. From top are (a) synchronized photography, (b) reflectivity (dBZ), (c) storm-relative mean velocity ($\mathrm{m\,s^{-1}}$), (d) differential reflectivity (dB), and (e) differential phase (°).

to 1.5 km, which correlates to areas of darker, brown smoke in the photo at height of 0.1 km. The storm-relative mean velocity[1] in Figure 4.2c shows patches of inward and outward radial velocity within the smoke plume. Previous work [6] has attributed this observation to the presence of horizontal vortices in the smoke plume.

[1]Storm-relative mean velocity is taken as the difference between smoothed and raw estimates of velocity in a 1 km sliding window

Differential reflectivity shows similar patterns within the smoke plume as noted previously. Above the fire, at [1.4, 0.25]km, the mean $\hat{Z}_h$ and $\hat{Z}_{dr}$ are 22.4 dBZ and 0.1 dB, respectively. Away from the fire within the smoke plume at [1.1, 0.35]km), the mean $\hat{Z}_h$ and $\hat{Z}_{dr}$ are 17.9 dBZ and 1.1 dB. Positive $\hat{Z}_{dr}$ is consistent with previous work [75] and agrees with debris sample measurements as predominantly flat, plate-like particles from leaf matter. Copolar correlation coefficient (not shown) for the Barossa Reservoir data has a mean value within the plume of 0.61 and shows no pattern with reflectivity or location of the fire source. Differential phase, shown in Figure 4.2e, shows spikiness and variability within the plume. We observe large spikes as high as 45° within a 50 m range swath. This high variability between adjacent resolution volumes indicates predominantly backscatter differential phase.

Copolar correlation coefficient was low throughout the burns, averaging between 0.4 and 0.7. The mean correlation coefficient observed from the prescribed burns, Barossa Valley and Cox Scrub, is much higher than that reported in the uncontrolled bushfire at Cherryville. The uncontrolled bushfire was more intense than any of the prescribed burns, with measured reflectivities as high as 40 dBZ versus 25 dBZ for the controlled burns. This increased intensity may be causing higher turbulence within the smoke plume, which could explain the reduced correlation coefficient.

4.3.3 Analysis

We propose the following model to describe the scattering mechanism within the smoke plume at X-band. There are two dominant regions within the plume: above the fire source and downwind away from the fire source. We hypothesize that the localized variations in Z_{dr} are due to differences in the motion of ash and debris particles around these two regions. Above the fire source, where the heat flux and vertical updraft within the convection column are highest, the particles tumble more quickly about their axis as they are propelled upwards. These tumbling particles

appear to have a lower Z_{dr} because they scatter more in each polarization. As the debris particles rise and interact with ground winds, they are pushed away from the fire. These particles float or drift with their major axis parallel to the ground, causing higher measured Z_{dr} values.

Analysis of the data shows no recognizable pattern in ρ_{hv}, either at the fire source or areas downwind. Studies and field work [94] have observed that intense fires can create a downdraft of mist or water droplets, formed by water condensation onto smoke particulates as warm, moist air from the convective column cools and falls. This suggests that ρ_{hv} during these types of fires may be higher and more resembling precipitation (> 0.9). It is unclear as to whether the fires observed were not intense enough to create this effect, or the mixture of condensed water droplets and larger ash particles would still reduce the copolar correlation coefficient within the plume.

An analysis of the data was also performed to quantify how bushfire smoke plume returns would be classified in a traditional Hydrometeor Classification Algorithm (HCA). Figure 4.3 shows a statistical analysis of observations over a 3 h period from the Cherryville uncontrolled bushfire (10-May-2013). To generate this data, clutter cells were first identified and removed using the clutter identification procedure described by Hubbert et al. [58]. Next, a Signal to Noise Ratio (SNR) threshold of 10 dB was applied to the data, and each scan was visually inspected to ensure clutter or unidentified echoes were not contaminating the results. Products for differential reflectivity, copolar correlation coefficient, and textures of reflectivity and differential phase were gathered against reflectivity in 5 dBZ bins from 5 dBZ to 30 dBZ, corresponding to the the range of reflectivities observed over the burn. For each reflectivity bin, the mean, median, and 10th/25th/75th/90th percentiles of the data were computed.

Analysis of the data in Figure 4.3 shows a strong correlation with the Biological Scatterer (BS) category in the HCA. Low copolar correlation coefficient (0.4 to 0.6)

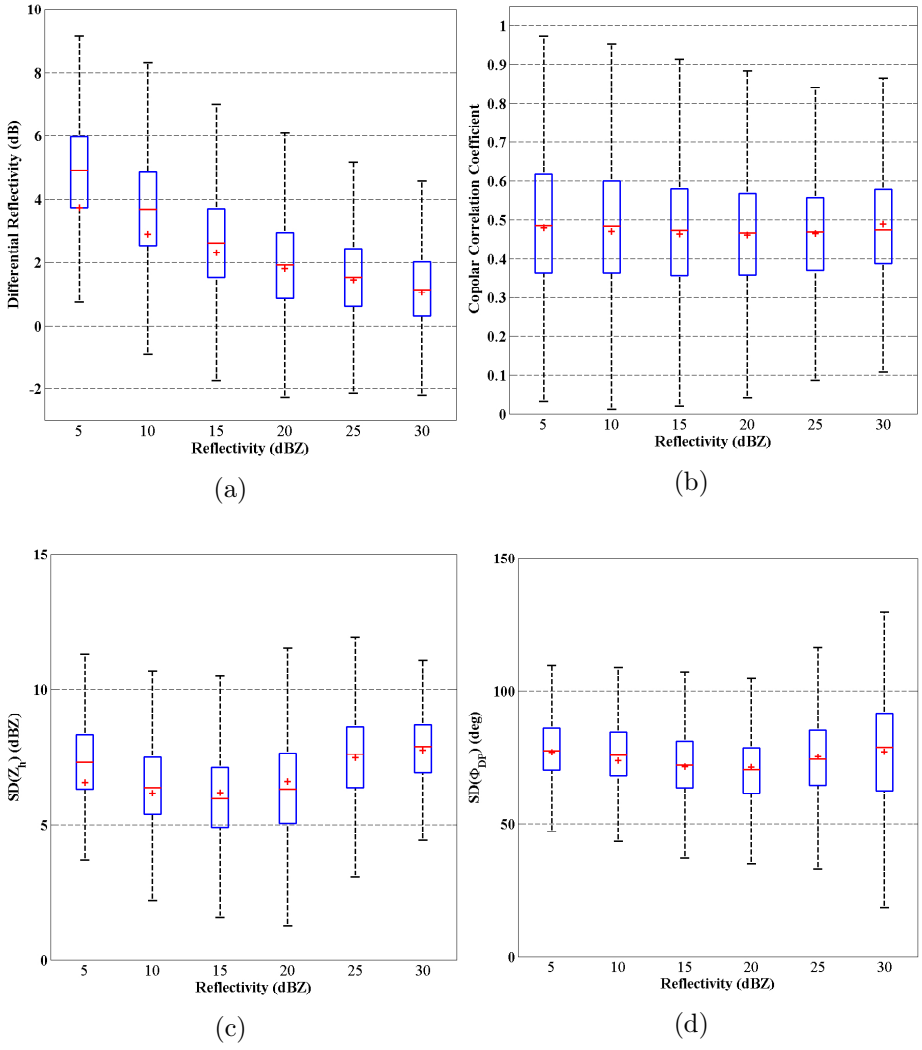

Figure 4.3: Statistical analysis from the Cherryville uncontrolled bushfire for measured (a) differential reflectivity, (b) copolar correlation coefficient, (c) texture of reflectivity, and (d) texture of differential phase. The bottom and top lines of the blue boxes represent the 25th and 75th percentiles, respectively, of the data for the corresponding reflectivity bin, and the top and bottom edges of the dashed lines represent the 10th and 90th percentiles. The red + symbol and line represent the mean and median of the data, respectively.

and high textures of reflectivity (5 dBZ to 8 dBZ) and differential phase (60° to 80°) are major discriminators from precipitation echoes. In agreement with our proposed model, differential reflectivity shows a decreasing trend with increasing reflectivity. The Pearson correlation coefficient [48] between reflectivity and differential reflectivity is -0.4 ($\alpha < 0.05$), which indicates a weak inverse correlation. These results are in

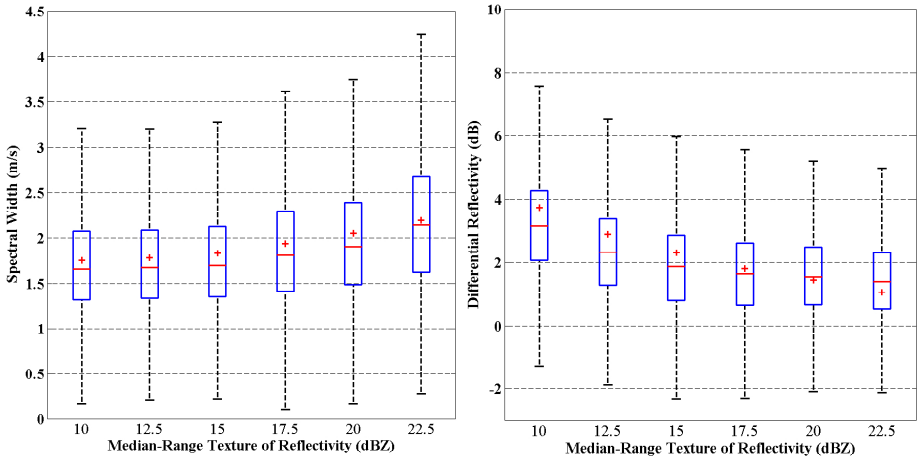

(a) (b)

Figure 4.4: As in Figure 4.3, but showing a statistical analysis from the Cherryville uncontrolled bushfire on 10-May-2013 compared against the Median-Range (MR) texture field ($\mathrm{MR}_{12,12}^{6,6}$). Data shows (a) spectral width and (b) differential reflectivity.

accordance with our initial hypothesis. Spatial texture fields have long been used in HCAs to differentiate precipitating from non-precipitating echoes [88, 2].

The previous data shows a weak correlation between increased reflectivity and locations of the active fire sources. To take advantage of this across forest fires of different size and intensity, we use texture analysis to detect areas within the smoke plume that have *relatively* higher reflectivity than the surrounding area. The spatial texture of reflectivity, taken as the mean Root Mean Square (RMS) difference between a Cell-Under-Test (CUT) and a kernel window (as in (3.4.18)), has shown to be a good discriminator between clutter and precipitating echoes [52, 58]. An alternate texture field is the Median-Range texture (see (3.4.20)), which is derived from the use of range filters for edge detection.

As in Figure 4.3, Figure 4.4 shows differential reflectivity and spectral width compared against the Median-Range texture field ($\mathrm{MR}_{12,12}^{6,6}$). As in the previous analysis, data shows that differential reflectivity and spectral width are weakly correlated to reflectivity, with correlation coefficients of 0.35 and -0.3 ($\alpha < 0.05$), respectively.

4.4 Forest Fire Detection and Monitoring

Based on the previous analysis, observations of forest fires at low elevations by small-scale systems present different signal characteristics than observations made at higher elevations by larger systems. Returns made directly above the fire source show increased reflectivity, lower differential reflectivity, and higher spectral width. These results agree well with the physical processes occurring in the fire. As ash particles and debris are lofted upwards in the convection column, their concentration is highest directly above the fire. Since there are more particles in the radar resolution volume, each tumbling at different rates, this results in increased reflectivity and spectral width. For polarimetric radars, the net effect of tumbling in both polarizations leads to a reduced apparent differential reflectivity. As these particles rise, interaction with ambient ground winds and natural dispersion in the atmosphere reduces their concentration. Larger, ashy leaf matter either breaks up into fine particulates that are undetectable by the radar or is carried downwind. Reduced concentration of particles having a mean motion vector closer to that of the ambient wind reduces their reflectivity and spectral width presented to the radar. Since the particles are no longer tumbling, they float with their major axis parallel to the ground, and the measured differential reflectivity increases.

Based on these results, we propose the following technique for the detection and monitoring of active forest fires by small-scale radar systems, known as the Bushfire Detection and Monitoring (BDM) algorithm. The purpose of this algorithm is to provide localized detection and monitoring of active fires in a small area. A system that could implement the algorithm would be able to provide the following capabilities:

- Detection and tracking of active fire fronts and smoke plume dispersion
- High spatial resolution (10 m to 250 m resolution)
- Near real-time imaging (5 s to 10 s) of a 10 km^2 to 20 km^2 area

- Lower atmospheric coverage (0 m to 500 m above vegetation tops)

Such a system would greatly enhance the current situational awareness during a fire by providing more localized and actionable data to firefighters over a large area. The system could be implemented on either a mobile platform or as a network of radars for border protection surrounding an urban area. Since spatial resolution is heavily dependent on angular resolution (typically 1° to 3° for X-band radars), mobile platforms could be deployed near the fire front (2 km to 4 km away) to provide higher spatial resolution and active tracking, while a fixed radar network could provide detection and surveillance capabilities for new threats.

The algorithm can be broken into three distinct stages: classification, identification, and tracking. The purpose of the classification stage is to classify all resolution cells in the scan volume as either potentially belonging to a smoke plume and to identify and discard returns from clutter and precipitation. The identification algorithm uses fuzzy logic and storm cell tracking techniques to estimate the likelihood that resolution cells within the smoke plume are located directly above active fire sources. The tracking algorithm monitors potentially active fire areas and provides an estimate of the surface wind field around the fire. These stages, as well as initial assumptions and hypothesis, are presented in the subsequent sections.

4.4.1 Assumptions

This algorithm makes the following assumptions about the dispersion of smoke particulates and ash particles from active fires. From the point of view of the radar system, it is assumed that the dominant scattering mechanism is only from significant concentrations of millimeter-size or larger size particles. Reflections from ash particulates (having diameters less than 10 µm to 1000 µm), ducting from high gradients in refractivity from high temperatures above the fire, or returns from potential water vapor or condensation near the fire [94] are assumed to be negligible.

The smoke plume itself, specifically the gas and aerosols in the plume less than 20 µm in diameter, is assumed to follow a Gaussian dispersion of the form [114]

$$\chi(x,y,Q,H) = \frac{Q}{2\pi\sigma_y\sigma_z u}\exp\left[-\frac{1}{2}\frac{y}{\sigma_y}^2\right] \left\{\exp\left[-\frac{1}{2}\frac{z-H}{\sigma_z}^2\right] + \exp\left[-\frac{1}{2}\frac{z+H}{\sigma_z}^2\right]\right\} \quad (4.4.1)$$

Where χ is the concentration of particles ($\mathrm{g\,m^{-3}}$), Q is the source emission rate ($\mathrm{g\,s^{-1}}$), σ_y and σ_z are the standard deviations of the concentration distributions in the crosswind and vertical directions (m), H is the the effective plume height (m), and x, y, and z are the downwind distance, crosswind distance, and vertical height from the fire source, respectively (m). This model assumes homogeneous meteorological weather and wind conditions around the region of interest, no downwind dispersion, and a constant emission rate. This dispersion model is the basis for several different commercial smoke plume model algorithms in use today ([106, 68]).

While (4.4.1) models the dispersion of small smoke particulates and aerosols, which are not assumed to be a dominant scattering mechanism for small-scale radars, this algorithm assumes that the larger particles and debris follow a similar dispersion model when viewed very near the fire source. That is, the concentration of larger particles within the smoke plume also follows a Gaussian distribution. For wind-driven fires, the flow and direction of the smoke plume (and therefore the ash and debris within the smoke plume) are dominated by the ambient surface winds in the lower 2 km to 3 km of the atmosphere. When these winds are light, the buoyancy of the hot gases in the convection column dominates and the particles within the smoke plume are projected into the upper atmosphere. Under the model assumption in (4.4.1), the direction of the smoke plume will always align with the ambient ground

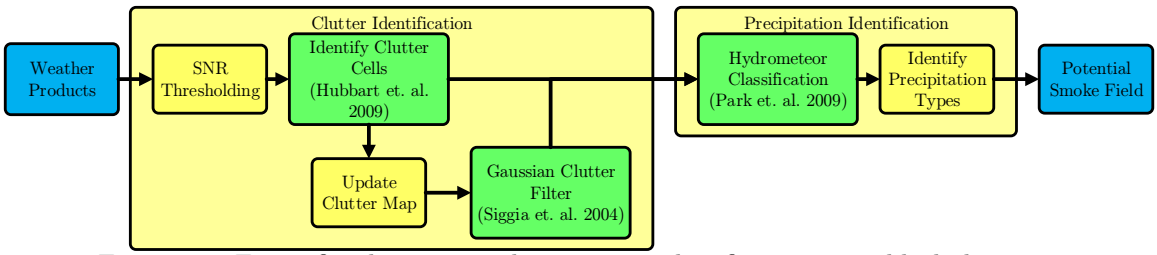

Figure 4.5: Forest fire detection and monitoring classification stage block diagram.

winds, if they are strong enough, but the spatial distribution of particles through a cross section of the plume is assumed to be Gaussian.

4.4.2 Classification

The purpose of the classification stage is to discriminate potential smoke plume returns from clutter, biological scatterers (such as birds and insects), and precipitation returns in the scan volume. It is important to filter out unwanted signals as much as possible in this stage, because any returns misclassified as smoke will result in false detections. The discrimination of smoke plume returns against other scatterers is done through the use of sequential algorithms for clutter identification and hydrometeor classification. Figure 4.5 shows a block diagram of the classification stage algorithm.

Classification begins with a SNR threshold to remove weak echoes (typically 6 dB), followed by a clutter identification algorithm. Clutter identification implements the technique developed by Hubbert et al. [58], using the same membership functions, weights, and thresholds described therein. This algorithm uses a fuzzy logic scheme with spatial texture and gradient feature fields to discriminate clutter. At the output of the algorithm, cells with a high likelihood of containing clutter are identified and re-processed through a clutter filter. A Gaussian Model Adaptive Processing (GMAP) technique is used to suppress clutter returns while preserving echoes from returns which present a Gaussian Doppler spectrum [107].

Following the clutter identification and filtering stage, unwanted precipitation returns are identified with the HCA developed by Park et al. [88]. This algorithm uses

the same trapezoidal membership functions, weights, and empirical limits described therein. Since the features of smoke plume returns overlap heavily with the Biological Scatterers (BS) type (see Section 4.3), a new classification type solely for smoke plume returns would not be effective. Since the purpose of this stage is to reject unwanted returns, any resolution cells identified from snow, ice, or rain precipitation types are identified and discarded[2].

The output of the classification stage is a set of filtered polarimetric products (as described in Chapter 3) and a binary matrix identifying which resolutions cells contain potential smoke plume returns.

4.4.3 Identification

The purpose of the identification stage is to identify the resolution cells within a potential smoke plume which have an increased likelihood of being located above or near a fire source. Specifically, the algorithm searches for areas which have (1) increased reflectivity relative to the rest of the smoke plume, (2) high spectral width, and (3) low differential reflectivity.

[2]It should be noted that precipitation, insect swarms, or flocks of birds were never observed during the attended bushfires in the field campaign. So, the data gathered is predominantly from smoke plume backscatter returns, clutter, and occasional air traffic around some of the burns. Operationally this will not be the case, however. This precipitation rejection stage is included to mimic real-world operation and verify that smoke plumes are not misidentified as precipitation.

Table 4.2: Parameters for membership functions for active forest fire classification.

	$P(\text{MR})$	$P(\sigma_v)$	$P(Z_{dr})$
SNR Threshold (dB)	6	6	10
x_1	15	2	$-\infty$
x_2	20	3	$-\infty$
x_3	∞	∞	2
x_4	∞	∞	2.5

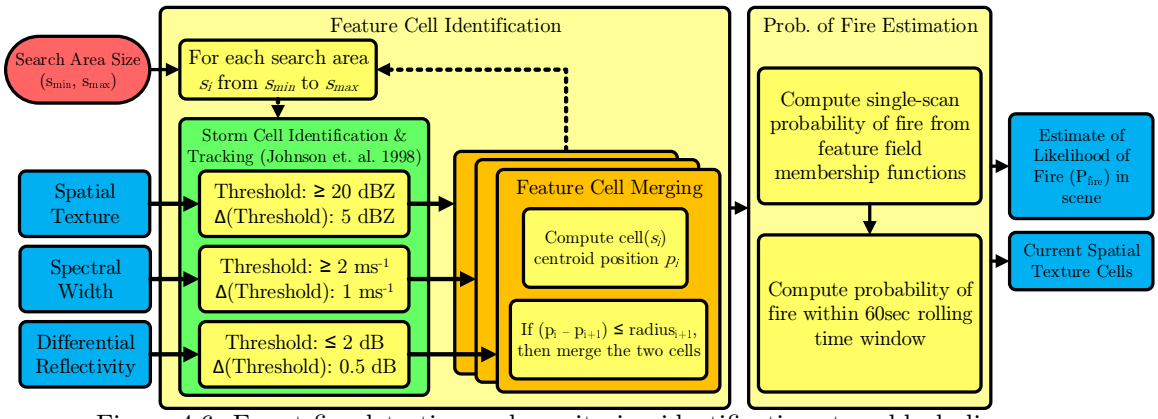

Figure 4.6: Forest fire detection and monitoring identification stage block diagram.

From a top-level perspective, the identification stage is a fuzzy logic algorithm using membership functions for spatial texture ($\mathrm{MR}_{m,n}$), spectral width (σ_v), and differential reflectivity (Z_{dr}). In contrast to traditional fuzzy logic techniques, however, the algorithm computes the aggregate summation of weights within a pre-defined area instead of each resolution cell. Since the convection column above the fire, where the algorithm is searching for specific polarimetric signatures, is confined to a specific area, it is natural then to only look for *areas* in which these signatures are present.

Table 4.2 summarizes the membership function parameters for each variable, which are derived from the data in Figure 4.3. Parameters x_1 through x_4 define the shape of a trapezoidal membership function [88], where x_1 and x_4 specify the lower base of the trapezoid, and x_2 and x_3 define the upper corners. Membership functions having parameters defined at $\pm\infty$ define one-sided trapezoidal membership functions. Lower limits are used for spatial texture and spectral width, and an upper limit is defined for differential reflectivity. The fuzzy logic algorithm can be described as an aggregate summation of membership functions, subject to a restriction on the connected component size of the feature fields

$$P_{fire} = \frac{\sum_i w_i P\left[x_i\right]}{\sum_i w_i} \tag{4.4.2}$$

Where P_{fire} is the likelihood that active fire is present at a resolution cell. P and w_i are the membership function and weight applied to the ith feature field, x_i, respectively. The membership functions are only valid where P_i is positive within a connected region

$$P\left[x_i\right] = \begin{cases} \text{trapmf}_{x_i} & \text{area}\left[x_i\right] > s \\ 0 & \text{otherwise} \end{cases} \tag{4.4.3}$$

This condition states that the membership function for x_i is only positive where an entire area of size s is positive. In other words, the fuzzy logic algorithm is performed with a coarse resolution cell size of s m^2. The term *connected region* is used here to describe an area of minimum size s in which all resolution cells are neighbors of each other, with a positive membership function weight.

The identification stage algorithm requires user inputs on the lower and upper limits ($s_{\text{min,max}}$) of the size of the active fire region to detect, specified as an area (m^2). The purpose here is to let the user threshold the size of active fires to detect and to minimize false detections for potential fires outside these limits. These size constraints correspond to the area threshold s given in (4.4.3). The algorithm uses these thresholds to iteratively search for areas which contain high spatial texture of reflectivity, high spectral width, and low differential reflectivity, subject to the membership functions and SNR thresholds in Table 4.2. On each iteration, corresponding to a specific search area s from s_{min} to s_{max}, the feature fields are first computed for the given area. The kernel window for the Median-Range texture ($\text{MR}_{m,n}$) is resized such that the [l, k] guard window matches the current search area, and the fields for spectral width and differential reflectivity are passed through a 2D low-pass filter with a passband equal to the search area. These feature fields are then fed to parallel Storm Cell Identification and Tracking (SCIT) algorithms [63].

The SCIT algorithm is a well-known and documented technique to detect and track regions of reflectivity which exceed pre-designated thresholds. In the original implementation on the WSR-88D system, storm cells are identified as regions of reflectivity which exceed (typ.) 30 dBZ and meet minimum size and detection requirements. As opposed to traditional target detection algorithms, the SCIT algorithm is a proven technique for the detection of volumetric targets.

Parallel SCIT algorithms are used here to identify areas of the feature fields having a size equal to or greater than the current search area. On each iteration, the SCIT algorithms generate a list of cells for each feature field. Each cell represents an area within the feature field greater than or equal to the current search area where the feature field membership function is positive. Once all search areas are processed, cells from the same feature fields are merged together. Two cells are merged if the centroid of one cell falls within the area contained by another. A similar approach is used by Johnson et al. [63] to merge storm cells from different reflectivity thresholds.

The output of the iterative search is a list of identified cells for each feature field on the current scan, where each cell defines an area where the feature field membership function is positive. The algorithm then computes the aggregate sum of the membership functions at each resolution volume across all identified cells for spatial texture, spectral width, and differential reflectivity. This quantity is known as the single-scan probability of fire

$$p^s_{fire} = \frac{\sum_i w_i P\left[x_i\right]}{\sum_i w_i} \tag{4.4.4}$$

Where P and w_i are the membership function and weight applied to the ith feature field, x_i, respectively. Each of the feature fields are weighted equally, which reduces (4.4.4) to an arithmetic mean. Since the feature fields used in the membership functions of (4.4.4) are cells, the single-scan probability of detection will contain localized areas where the feature field cells overlap each other. Areas within p^s_{fire} which ex-

ceed a pre-determined threshold are identified as active fire areas. This threshold is nominally set at 0.95 to strictly enforce the membership functions in Table 4.2.

Once the single-scan probability of detection is computed, the algorithm is repeated for consecutive scans within a 60 s time window. The likelihood that a region of active fire is present within this time window, known as the probability of fire (P_{fire}), is computed at each resolution cell in the scene as the arithmetic mean of the series single-scan probabilities of detection

$$P_{fire} = \frac{\sum_s p^s_{fire}}{N_s} \tag{4.4.5}$$

Where N_s is the total number of scans observed in the time window. Equation (4.4.5) represents the probability that an active fire is present below each range cell. The output of the identification stage is the probability of fire fields (P_{fire} and p^s_{fire}) within the current time window and the feature cells obtained from the parallel SCIT algorithms.

4.4.4 Tracking

The purpose of the tracking stage is to monitor the potential active fire areas and to estimate the current ambient wind field. As mentioned previously, the input to the tracking stage is the feature cells and single-scan probability of fire from the current scan and the probability of fire field from the current time window. The algorithm also requires a user threshold on the maximum ground speed of the fire front. The rate of advance of a fire front depends both on local weather conditions and the topology over which the fire advances, and can be as high as $4\,\mathrm{m\,s^{-1}}$ to $6\,\mathrm{m\,s^{-1}}$ [66]. To account for the unknown terrain of the scene, the algorithm expects a user guidance on the maximum fire speed. Figure 4.7 shows a block diagram of the tracking stage algorithm.

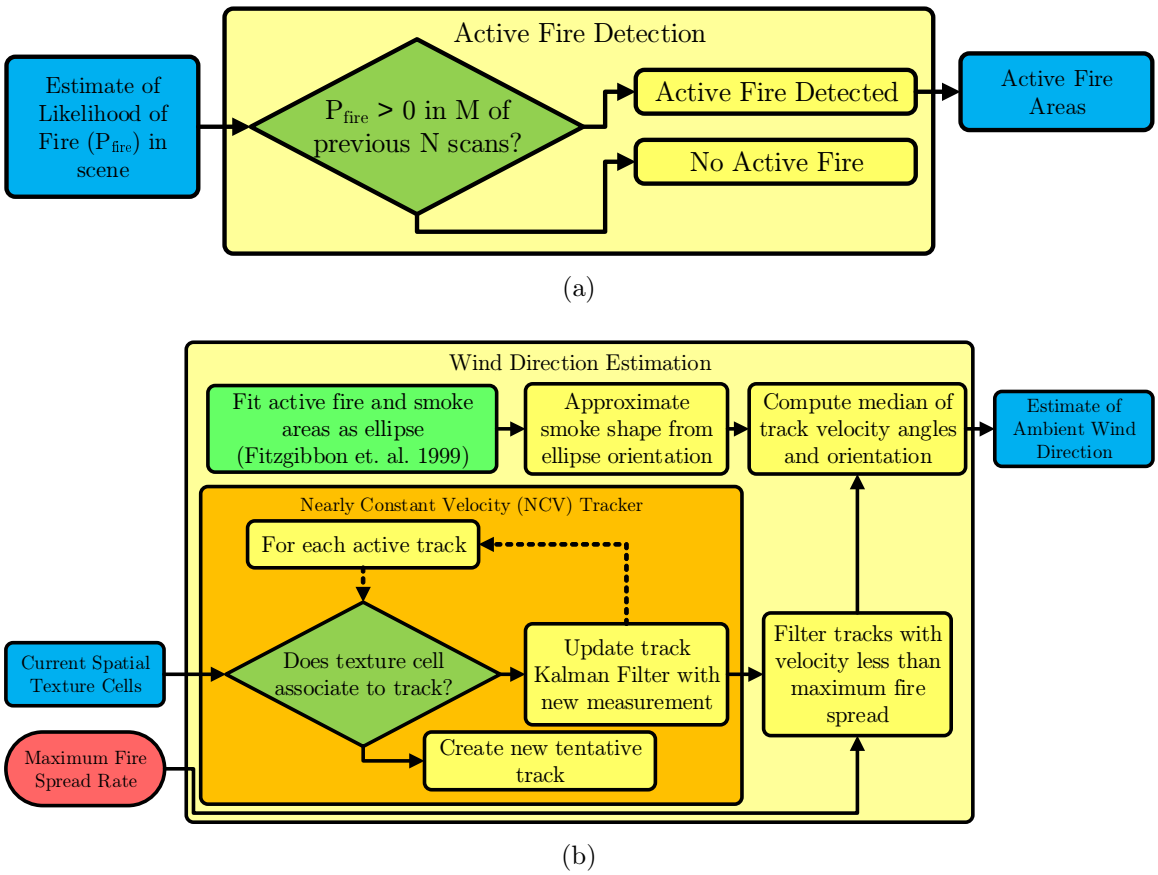

Figure 4.7: Forest fire detection and monitoring tracking stage block diagrams for (a) active fire detection and (b) wind direction estimation.

At the conclusion of each scan, active fire areas are declared as regions where the probability of fire (P_{fire}) exceeds a set threshold (nominally 0.5). This can be interpreted as a binary M of N detection algorithm [1, 97], where active fire is declared if $P_{fire} > 0$ in at least M radar scans out of the previous N. Here, M and N are set according to the number of available scans in the previous 60 s sliding window. Under nominal scan parameters for a 40 ms dwell time per radial and a 3.5 s azimuth scan, M and N correspond to 8 and 15, respectively. Areas in the scene which meet this M of N condition logic are identified as active *fire cells*.

Ambient wind direction is estimated using two different methods: from the flow field and the shape of the smoke plume. The flow of the smoke plume is estimated by measuring the motion of the particles within a specified time interval. Since

the spatial texture already identifies the regions within the plume with high particle concentration, it is natural then to track the motion of these texture cells as the flow of ash particles. Using the texture cells output from the identification stage, the motion of the cells is approximated using a Nearly Constant Velocity (NCV) model. Under this model, the cells are assumed to move with constant velocity between scans. That is, the algorithm assumes that the flow of the smoke plume, as estimated from the motion of these cells, is nearly constant between discrete time intervals. A Nearly-Constant Velocity (NCV) Kalman Filter algorithm with nearest neighbor data association and track initiation logic is implemented to filter the motion of the cells. The measurements of the Kalman Filter are the feature cell centroid positions, and the state provides an estimate of the cell position and velocity (see Appendix 4.7 for a description of the tracking algorithm). The flow field of the smoke plume is then computed from the median velocity vector from all tracked feature cells.

Ambient wind direction is also estimated from the shape of the smoke plume as follows. From the perspective of a radar scanning in one elevation cut through a smoke plume, a wind-dominated fire will present an ellipsoid-shaped echo with the fire source at one focus and the orientation of the ellipse aligned with the ambient wind direction along the major axis. To estimate the orientation of the major axis, and thus the ambient wind direction, we use an elliptical approximation technique [78] (see Appendix 4.8). Using this technique, the collection of resolution cells in the smoke plume are treated as a cluster of spatially-distributed data points. The approximation fits an ellipse around the 95 % confidence limits on this cluster. The wind direction is then estimated from the angle of the major axis in the direction of mean radial velocity within the smoke plume.

The ambient wind direction on each radar scan is computed from filtered estimates of the flow field and orientation of the smoke plume. Raw wind estimates are first computed from the median of velocity vectors from the flow field and orientation. The

final, filtered estimate is taken from a 60 s moving average of raw estimates. Because of the moving average operation, wind estimates are provided at a 30 s delay.

The output of the forest fire detection algorithm is a list of the (1) active fire areas where the probability of fire exceeds a pre-determined threshold and (2) an estimate of the wind direction from the flow and shape of the smoke plume.

4.5 Verification

From the 8 burns and bushfires attended during the field campaign listed in Table 4.1, different data sets were selected for *training* or *verification*. Training sets were used to develop, test, and fine tune the performance of the algorithm on real-world data. Once development was complete, the data from the verification sets were processed through the algorithm. Verification sets are used as *untrained* data to test the algorithm without bias. Specifically, two burns were chosen for training: South Para Reservoir (10-April-2013) and Barossa Reservoir (17-April-2013). The rest were used solely for verification and performance measurement. This section presents the verification methodology and results.

4.5.1 Verification Methodology

Under ideal conditions, the BDM algorithm should be tested against in-situ Infra-Red (IR) and LIDAR instrumentation, which would provide accurate truth data on the location of the heat sources and highest concentration of smoke particulates. However, only timelapse photography and local weather station data was available for the field campaign. Timelapse photography was obtained with a high-definition camera mounted on top of the array face aligned with the array boresight. At the start of each radar scan, the camera was digitally commanded to take a snapshot via control from the radar software. Weather data was available either from mobile weather stations setup by the fire management crews at each burn or permanent stations

maintained by the Australian Bureau of Meteorology. Weather data includes mean and standard deviation of local wind speed and direction, wind gusts, temperature, pressure, and humidity in 1 min intervals.

For each bushfire tested, the algorithm was applied to the raw timeseries data collected on each scan in the data set, typically over 2000 scans lasting 1 h to 3 h. As described in Section 4.4, the output of the algorithm after each scan is a feature field for the probability of fire field, which indicates the likelihood that an active fire is present in the resolution cell in a 60 s window ending on the current scan. Nominally, resolution cells with a probability of fire greater than 50 % ($P_{fire} > 0.5$) are declared as active fire detections. Also output is an estimate of the wind velocity vector at each scan, taken from estimates of the flow and shape of the smoke plume in the previous 60 s time window.

To measure the performance of the algorithm, the following metrics were used. Fire management crews maintain records of the burn map for each prescribed and uncontrolled bushfire in local fire management plans. The area for prescribed burns are planned years in advance to control the regrowth of vegetation in a large area. Similar records are kept for uncontrolled bushfires. The total burn area was estimated from the algorithm by computing the maximum probability of fire at each resolution cell over all scans processed. The total burn area estimate was then compared to the burn area map as recorded in the fire management plan.

Another method used is the timeline of fire activity. From timelapse photography and historical records, the speed and direction of the fire front can be estimated. In this manner, the location of the fire front can be tracked throughout the burn. The timeline of fire activity is computed from the algorithm by plotting the time and location of the centroid of each active fire area at 1 min intervals throughout the burn. The direction of spread of the fire is then estimated by tracking these centroids as a function of time.

Wind direction data was also compared against ground truth. To mimic the format of the weather station data, wind estimates from the algorithm were averaged in 1 min intervals throughout the data set. The wind estimation error was computed as the RMS error between the ground truth and algorithm estimate.

The algorithm was tested against two different bushfires: a prescribed burn at the Cox Scrub Conservation Park (1-May-2013) and the uncontrolled bushfire at Cherryville (10-May-2013). The verification results from these burns are presented in the following sections.

4.5.2 Cox Scrub Prescribed Burn (1-May 2013) Results

A prescribed burn was conducted by South Australian CFS and DEWNR personnel at the Cox Scrub CP (10-May-2013), which lasted over 3 h from first ignition at 04:30 UTC until 07:30 UTC and burned over 40 ha. Recorded timeseries data from the burn was processed by the fire detection and monitoring algorithm. The algorithm was completely untrained to the data and setup to search for active fires from $500\,\mathrm{m}^2$ to $1000\,\mathrm{m}^2$ in size with a maximum fire spread rate of $6\,\mathrm{m\,s}^{-1}$.

A sample output from the BDM algorithm during the burn at 05:28 UTC is shown in Figure 4.8b along with timelapse photography at the same instant in Figure 4.8a. The picture shows a small patch of forest burning at a cross range extent from $-0.22\,\mathrm{m}$ to $-0.12\,\mathrm{m}$, with the smoke plume extending from the fire source at an angle towards the radar. By comparison, the algorithm estimates the active fire in the scene to extend from $-0.22\,\mathrm{m}$ to $-0.36\,\mathrm{m}$ at a down range centered at 2 km. The discrepancy in the estimate of the fire location from the algorithm is due to strong ground winds. The heat flux from the fire is not strong enough to project the smoke plume into the upper atmosphere, so the ambient ground winds dominate and the smoke plume height is reduced. The radar is unable to accurately measure the smoke plume at its base because of clutter contamination near the tree line.

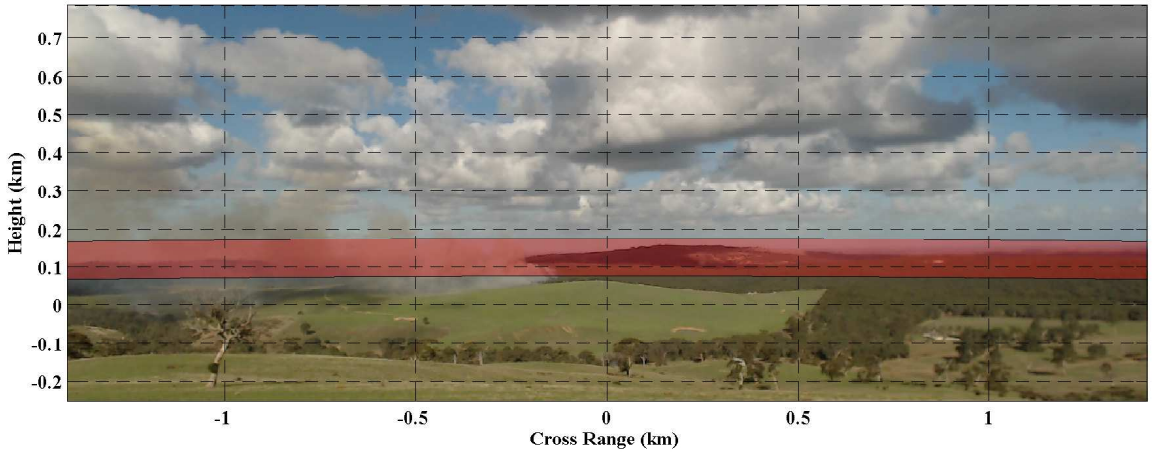

(a)

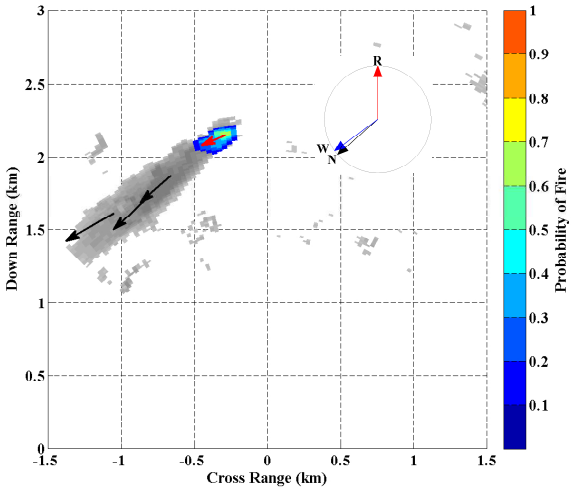

(b)

Figure 4.8: Snapshot of data processed by the BDM algorithm from the Cox Scrub CP prescribed burn at 05:28 UTC, showing the (a) timelapse photography and (b) algorithm output. The black box in (a) indicates the location of the active fire in the scene, which corresponds closely to the region of increased probability in (b). Black and red arrows in (b) indicate the wind estimates from the flow field and smoke plume shape, respectively. The arrows enclosed in the circle in (b) indicate due North (N), the radar heading (R), and measured wind direction (W).

From Figure 4.8, we see that the smoke plume is drifting in the wind, slightly towards the radar at a true angle of 15°. A local weather station data recorded the wind direction at that time to be 20° ± 10°, which closely matches the estimate from the algorithm. Wind estimates over a 1 h period during the burn, shown in Figure 4.9, show intermittent periods of weak and strong correlation ground truth. Over the

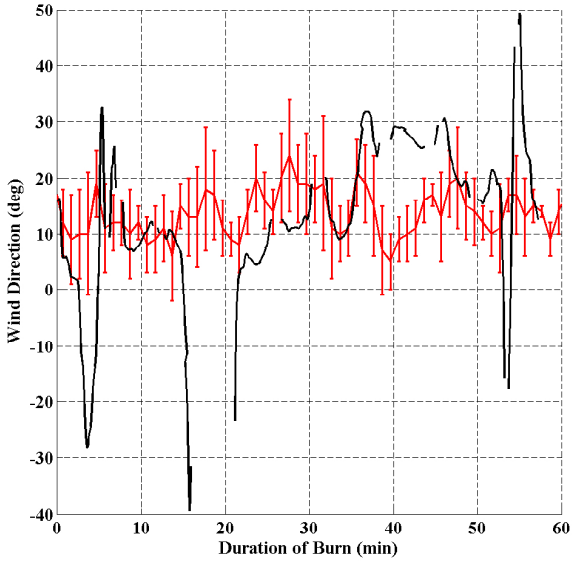

Figure 4.9: Wind estimates from the BDM algorithm applied to the Cox Scrub CP prescribed burn over a 1 h duration throughout the burn. The red line shows the mean and standard deviation of wind direction measurements from a nearby weather station, and the black line are the wind direction estimates from the algorithm. The gaps in the wind estimates correspond to times when the algorithm did not detect any active fires.

entire 1 h interval, the RMS error between wind estimates and weather station data during is 17.3°. While some of this error could be contributed to the separation between the weather station and the burn (16 km), gaps in the wind estimates are caused by periods when no active fire was detected by the algorithm. Inspection of the timelapse photography shows that these gaps occur when the intensity of the burn reduced. Since this was a controlled burn, these periods could correspond to breaks in the burning from fire crews.

Figure 4.10 show plots of the (a) total burn area and (b) fire timeline. The black dotted line in Figure 4.10 indicates the total area burned from CFS historical records. Inspection of Figure 4.10a shows a strong correlation between active fire areas declared by the algorithm and historical records. Over 80 % of the recorded burn area corresponds to predictions from the algorithm. In addition, the fire timeline in Figure 4.10b shows that the fire crews started burning on the East side of the fire at [−0.31, 2.13]km [cross range, down range] and finished on the West side at

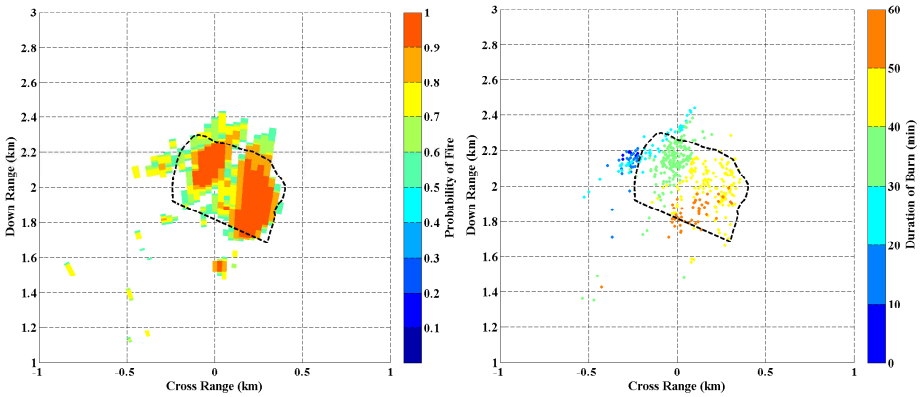

(a) (b)

Figure 4.10: Results from the BDM algorithm applied to the Cox Scrup CP prescribed burn, showing the (a) total area burned and (b) fire timeline. The total area burned shows the maximum probability of fire estimated from the algorithm at each resolution cell over the burn, while the fire timeline plots the centroids of each active fire area as a function of time since the start of the fire. The black dotted line is the actual area burned, from the recorded fire management maps from CFS personnel.

[0.12,1.83]km. This agrees well with timelapse photography and visual observations during the burn, with fire crews first igniting the burn at 04:30 UTC at a cross range of -0.29 km and proceeding westward.

4.5.3 Cherryville Uncontrolled Bushfire (10-May 2013) Results

For over three days from 9-May-2013, an uncontrolled bushfire near the town of Cherryville, South Australia burned over 650 ha. The radar made observations of the fire at a down range of 2 km to 3 km for a 6 h period on 10-May-2013, beginning at 04:45 UTC. The algorithm was completely untrained to the data and setup to search for active fires from 500 m^2 to 1000 m^2 in size with a maximum fire spread rate of 6 $m\,s^{-1}$.

Figure 4.11 shows the algorithm output at the same timestamp as shown in Figure 4.1. Comparison between the two figures show that the active fire present in the timelapse photography at a cross range of 0.10 km to 0.35 km agrees well with the area of increased probability of fire in Figure 4.11. The estimated wind direction,

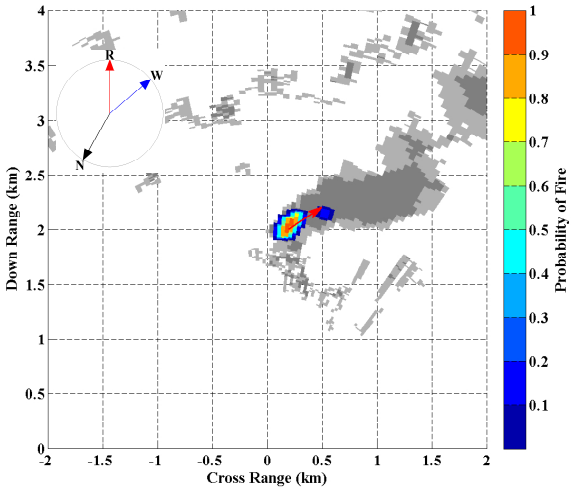

Figure 4.11: Results of the BDM algorithm at 06:14 UTC during the Cherryville uncontrolled bushfire at 06:14 UTC. Gray areas indicate potential smoke echoes, and the probability of fire feature field is indicated by the blue to red colormap. The red arrow indicates the estimate of the wind direction, while the arrows enclosed in the circle indicate due North (N), the radar heading (R), and measured wind direction from a nearby weather station (W). Note how the wind estimate aligns very well with the measured wind direction.

indicated by the red arrow, also aligns very well with the measured wind direction at the same instance (the blue arrow enclosed in the circle).

Wind estimates during the burn show good agreement with measured data from local weather stations. Figure 4.12 shows estimated versus measured wind estimates over a 140 min interval during the bushfire. The RMS deviation between the estimate and the measured data over the entire interval is 24.1°, while the error during a 40 min interval from 100 min to 140 min during peak intensity is just 11.2°. Since the algorithm relies on estimates of the smoke plume shape from the data, periods where the smoke plume echoes are weak or non-existent cause errors in the wind estimates. The period from 100 min to 140 min corresponds to when the bushfire intensity peaked.

Due to the large extent of the fire, burn maps from historical records cannot be used to precisely determine the area burned during the radar observation time. Nonetheless, the burn map and fire timeline during the bushfire is shown in Figure 4.13. Observations made during the fire indicate that intense burning began on

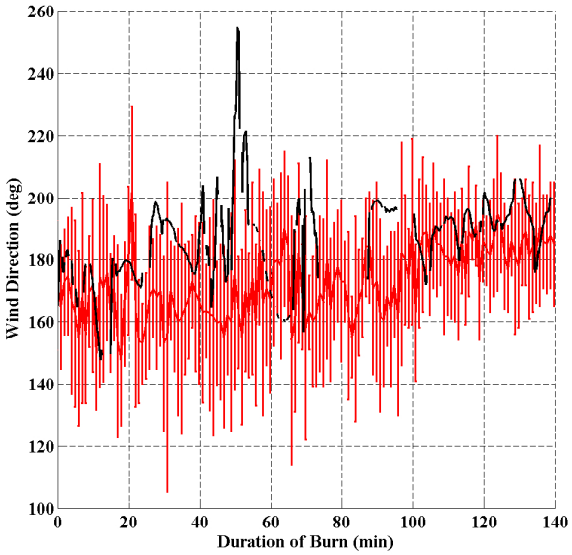

Figure 4.12: Wind estimates from the BDM algorithm during a 140 min period during the Cherryville uncontrolled bushfire on 10-May-2013. The red line shows the mean and standard deviation of wind direction measurements from a nearby weather station, and the black line is the wind direction estimates from the algorithm. The gaps in the wind estimates correspond to times when the algorithm did not detect any active fires. The RMS deviation between the estimate and the measured data over the entire interval is 24.1°, while the error during the 40 min interval from 100 min to 140 min during peak intensity is just 11.2°.

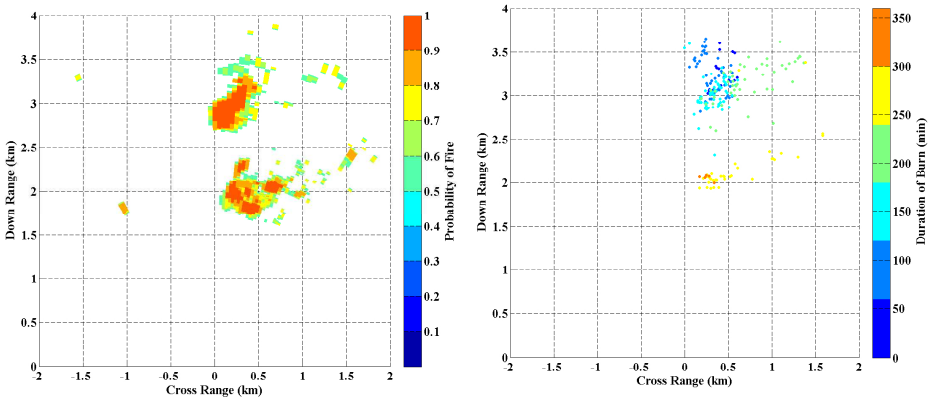

(a) (b)

Figure 4.13: Results from the BDM algorithm applied to the Cherryville uncontrolled bushfire on 10-May-2013, showing the (a) total area burned and (b) fire timeline. The total area burned shows the maximum probability of fire estimated from the algorithm at each resolution cell over the burn, while the fire timeline plots the centroids of each active fire area as a function of time since the start of the fire.

10-May-2013 on the side of a small ridge located 3 km to 4 km from the radar, and progressed Northerly towards the radar. These observations align well with the fire

timeline, which show intense fire activity at the beginning (60 min to 120 min) and end (260 min to 320 min) of the radar observation time.

4.5.4 Discussion

In addition to the data sets described previously, two additional data sets were also analyzed. Table 4.3 shows a summary of the results against all burns analyzed, comparing the actual area burned from historical records against the burn area estimate and wind direction RMS error. The burn area estimate from the algorithm is classified as areas *inside* or *outside* the actual burn area. That is, areas outside the burn area are taken to be false detections from the algorithm, and the difference between the inside and actual burn areas are missed detections.

While additional testing with co-located thermal imagery would be required to fully verify the performance, these results show that the algorithm does perform well during the burns. From timelapse photography, the algorithm estimates active fire areas coincident with the base of the smoke plume, radiating outwards in the direction of the ambient wind. In several cases, the rate and direction of fire spread correlates well to timelapse photography. Over all of the burns tested against, the average RMS wind direction error was 21.3°, with errors as low as 8.4° to 11.2° at times during several of the burns. The algorithm performs well at identifying areas above active fire sources, but it is prone to errors at low SNR from weak fires. We observed that most false detections occurred during wind-driven fires, when the ambient wind was strong enough to *topple* the convection column, causing the algorithm to incorrectly classify areas outside of the burn area as active fire.

4.6 Summary and Conclusions

Radar systems routinely observe smoke plumes from industrial and wildland fires, so the scattering mechanism of ash and debris particles is well understood. However,

Table 4.3: Summary of algorithm performance against different bushfires and controlled burns, showing the actual area burned from historical records against the algorithm burn area estimates and wind direction RMS error. Burn area from the algorithm is classified as areas inside or outside the actual burn area. The dash (–) in cells indicate that data is from an uncontrolled bushfire, where reliable burn maps are not available.

Date	Area Burned (ha)	Duration (min)	Est. Area Burned (ha)		Wind Dir. RMS Error (deg)
			Inside	Outside	
1-May-2013	40.0	60	36.5	17.4	17.3
2-May-2013	39.6	30	21.7	15.1	8.4
9-May-2013	-	25	33.8	-	26.9
10-May-2013	-	140	115.6	-	24.1

many of the previous observations were made at great distances to the fire front, so the smoke plumes could only be observed at great heights. In contrast, the measurements performed here were made with the radar system very close to the active fire (less than 5 km), which allowed the radar to make precise polarimetric measurements directly above the fire.

By comparing measurements from areas above the fire to those downwind, several patterns were discovered. Areas in the smoke plume directly above the fire show increased reflectivity, increased spectral width, and decreased differential reflectivity. These observations agree well with the physical process within the smoke plume. Higher concentrations of tumbling particles above the fire in contrast to lower concentrations of drifting particles downwind present different polarimetric signatures.

Based upon these assumptions, a BDM algorithm was proposed that estimates the location of active fires and wind direction from smoke plume observations. Using a newly proposed texture field for the Median Range (MR) field of reflectivity, the algorithm uses modified storm cell algorithms, combined with fuzzy logic, to estimate areas in the smoke plume which have increased probability of being above active fire

sources. The output field, known as the probability of fire, indicates potential active fire areas.

The algorithm was verified by processing untrained data from the field campaign. Comparison of the output against timelapse photography shows that the algorithm correctly identifies areas in the smoke plume above active fire sources. Results do show, however, that the algorithm is prone to errors for wind-dominated fires or if the smoke plume echoes are weak. On average, the algorithm estimates wind direction with an RMS error from 20° to 24°. As with the fire probability, wind estimates become unreliable when the SNR from the smoke plume decreases. However, during periods of peak fire intensity the RMS error of wind estimates decreased to just 11.2°. This indicates that the algorithm performance may improve during more intense, uncontrolled fires.

Research is currently underway to test the algorithm against additional forest fires in the Western United States. A low-cost, experimental system is being developed to refine and test the algorithm against a live forest fire. The future system will include a mobile command center to provide live, localized, and actionable data directly to fire management crews.

4.7 Constant-Velocity Kalman Filtering

The purpose this section is to describe the Kalman Filter algorithm used in the tracking of the feature cells. We begin by presenting the relevant equations used by the generic Kalman Filter algorithm without derivation. For a complete derivation of the equations and explanation, please refer to [98, 108].

4.7.1 Kalman Filter Basics

The flow of the Kalman Filter is a two stage process: prediction and correction. The prediction equations are used to predict an estimate of the state at the current

time, $X_{k|k-1}$, under a linear dynamic model from the state at some previous time, $X_{k-1|k-1}$. Associated with the state is the state error covariance, $P_{k|k-1}$, which is also estimated to the current time using a linear dynamic model. The notation $X_{i|j}$ refers to the estimate at the current state at time i using measurements up to and including time j. The predictor equations are given as

$$X_{k|k-1} = F_{k-1}X_{k-1|k-1} \tag{4.7.1a}$$

$$P_{k|k-1} = F_{k-1}P_{k-1|k-1}F_{k-1}^T + G_{k-1}Q_{k-1}G_{k-1}^T \tag{4.7.1b}$$

Where

$$\begin{aligned} X_{k|k-1} &= \text{predicted state estimate at time } k \\ X_{k-1|k-1} &= \text{corrected state estimate at time } (k-1) \\ F_{k-1} &= \text{linear dynamic model} \\ P_{k|k-1} &= \text{predicted state error covariance at time } k \\ P_{k-1|k-1} &= \text{corrected state error covariance at time } (k-1) \\ G_{k-1}Q_{k-1}G_{k-1}^T &= \text{input process noise} \end{aligned}$$

Note the subtlety in the above equations. The previous, corrected state at time $(k-1)$ is used to predict an estimate of the current state at time k. This is the same for both the state and the state error covariance. The input process noise matrix is often an algorithm design parameter that is used to model random dynamics of the state during state transitions. For the purposes here, it is set to the identity matrix. The corrector equations are

$$X_{k|k} = X_{k|k-1} + K_k \left[Z_k - H_k X_{k|k-1} \right] = X_{k|k-1} + K_k \tilde{Z}_k \tag{4.7.3a}$$

$$P_{k|k} = \left[I - K_k H_k \right] P_{k|k-1} \tag{4.7.3b}$$

$$K_k = P_{k|k-1} H_k^T S_k^{-1} \tag{4.7.3c}$$

$$S_k = H_k P_{k|k-1} H_k^T + R_k \tag{4.7.3d}$$

Where

$$X_{k|k} = \text{corrected state estimate at time } k$$

$$P_{k|k} = \text{corrected state error covariance at time } k$$

$$H_k = \text{observation matrix}$$

$$Z_k = \text{measurement}$$

$$\tilde{Z}_k = \text{measurement residual}$$

$$K_k = \text{Kalman Filter gain}$$

$$S_k = \text{covariance of measurement residual}$$

$$R_k = \text{measurement error}$$

The practical considerations of the Kalman Filter gain should be mentioned. The gain is a weighting that is applied to the measurement residual, which is then added to the predicted state, $X_{k|k-1}$, to get the corrected state, $X_{k|k}$. If the state error covariance is much lower than the measurement residual covariance, then the weighting will favor the state estimate over the measurement in computing the corrected state. If, on the other hand, the covariance of the measurement residual is lower, then the weighting will favor the measurement and the corrected state will be closer to the new measurement than the predicted state.

Practically speaking, the Kalman Filter optimally chooses the correct gain to minimize the error in the state prediction. If the previous measurement was fairly close to the previous state, then the Kalman Filter will trust the next measurement is more accurate than the next state estimate. However, if the previous measurement was very far from the previous state, then the Kalman Filter will trust that the previous state prediction was more accurate. Inherently, the Kalman Filter is optimized for the applicationŠs particular dynamic progression model.

4.7.1.1 Position and Velocity Estimation

A Kalman Filter for estimation of a target position and velocity in 3D Cartesian coordinates uses a [6,1] state matrix of the form

$$X_k = \begin{bmatrix} x_k & \dot{x}_k & y_k & \dot{y}_k & z_k & \dot{z}_k \end{bmatrix}^T . \tag{4.7.5}$$

Where (x_k,y_k,z_k) and ($\dot{x}_k$,$\dot{y}_k$,$\dot{z}_k$) are the target's position and velocity, respectively. The corrector equations take the state estimate, $X_{k|k-1}$, and a new measurement, Z_k, to compute a corrected state at time k, $X_{k|k}$. The corrected state is an optimal weighting between the measurement and the state estimate, known as the Kalman Filter gain at time k, K_k.

The observation matrix in (4.7.3) maps the state into the measurement space, and is simply a static matrix of the form

$$H_k = H = \begin{bmatrix} 1 & 0 & 0 & 0 & 0 & 0 \\ 0 & 0 & 1 & 0 & 0 & 0 \\ 0 & 0 & 0 & 0 & 1 & 0 \end{bmatrix}^T . \tag{4.7.6}$$

For input measurements as the current target position estimate, the measurement matrix is a [3,1] matrix of the form

$$Z_k = \begin{bmatrix} \hat{x}_k & \hat{y}_k & \hat{z}_k \end{bmatrix}^T . \tag{4.7.7}$$

Where ($\hat{x}_k$,$\hat{y}_k$,$\hat{z}_k$) are the target position measurements. The measurement noise, which defines the covariance matrix of the measurement, assumes that the measurements are independent, zero-mean Gaussian random variables. The measurement noise is assumed to be a zero-mean noise process having a covariance matrix equal to

$$R_k = \begin{bmatrix} \sigma_x^2 & 0 & 0 \\ 0 & \sigma_y^2 & 0 \\ 0 & 0 & \sigma_z^2 \end{bmatrix} . \tag{4.7.8}$$

Here, the variance terms define the error in each dimension about the measurement. The higher the measurement error, the less the Kalman Filter will trust new measurements to update the state.

4.7.1.2 Linear Dynamic Model for Nearly Constant Velocity

The linear dynamic model describes how the state evolves with time. In this application, the linear dynamic model describes the kinematic motion of the target. Here, we assume that between the discrete time intervals in which the algorithm updates, the target undergoes Nearly Constant Velocity (NCV). This kinematic motion is a design constraint that depends on both the estimated target model and the rate at which the filter will be fed new measurements.

Under the NCV model and assuming the state matrix in (4.7.5), the linear dynamic model matrix is given by

$$F_k = \begin{bmatrix} 1 & \delta_k & 0 & 0 & 0 & 0 \\ 0 & 1 & 0 & 0 & 0 & 0 \\ 0 & 0 & 1 & \delta_k & 0 & 0 \\ 0 & 0 & 0 & 1 & 0 & 0 \\ 0 & 0 & 0 & 0 & 1 & \delta_k \\ 0 & 0 & 0 & 0 & 0 & 1 \end{bmatrix} \tag{4.7.9}$$

Where δ_k is the elapsed time since the last update. Thus, we observe that the state prediction of the target position and velocity is simply a projection of the past target position plus the distance traveled, assuming the most recent velocity remained constant.

Another design choice in the Kalman Filter algorithm is the input process noise covariance matrix. The input process noise characterizes the motion of the target state that could occur between time internals. This could be caused by the geometry of the state coordinate frame or other factors, so care must be taken when choosing the form. We model the input process noise to account for random, unknown target maneuvers as a white Gaussian noise process having a spectral density of q g/Hz. Under this model, the input process noise matrix is given by [16]

$$G_{k-1}Q_{k-1}G_{k-1}^T = q \begin{bmatrix} \delta_k^3/3 & \delta_k^2/2 & 0 & 0 & 0 & 0 \\ \delta_k^2/2 & \delta_k & 0 & 0 & 0 & 0 \\ 0 & 0 & \delta_k^3/3 & \delta_k^2/2 & 0 & 0 \\ 0 & 0 & \delta_k^2/2 & \delta_k & 0 & 0 \\ 0 & 0 & 0 & 0 & \delta_k^3/3 & \delta_k^2/2 \\ 0 & 0 & 0 & 0 & \delta_k^2/2 & \delta_k \end{bmatrix} \tag{4.7.10}$$

In practice, the input process noise could evolve with time, to account for different target motion or different model behavior. For simplicity, we assume a constant input process noise for all state models. Studies have shown that typical values for q should be between 50 100% of the assumed target maximum acceleration [14].

4.7.2 Dual Extended Kalman Filter Applied to Radar Target Tracking

While the previous Kalman Filter derivation works well for estimating positions from measurements made in the Cartesian coordinate system, it is ill-suited to estimating the positional state of a target from measurements made in the spherical coordinate system, as is the case with most radar systems. As the Kalman Filter is a *linear* estimator, it assumes that the process and error covariance terms are linear functions from one state to the next. However, the conversion from the measurement frame (spherical coordinates) to the estimation frame (Cartesian coordinates) is non-linear. Thus, tracking

The Kalman Filter implemented here estimates the position of a target in a Cartesian coordinate frame using detection measurements provided by the radar system in polar coordinates. The complication in this scenario is the different coordinate systems. The Kalman Filter is optimized to minimize the mean square state pre-

diction error when the random processes, including measurement error, are assumed Gaussian. Although the radar measurement errors can be assumed to have zero-mean Gaussian statistics, the coordinate transformation from polar to Cartesian coordinate systems is non-linear. Thus, any white Gaussian noise in the measurement frame will change statistics when converted to a Cartesian frame. To solve this issue, this section describes a Dual-Extended Kalman Filter [13]. The two important differences between the Dual Extended Kalman Filter and the generic Kalman Filter are the observation matrix and the use of dual coordinate systems.

As shown in (4.7.3), the Kalman Filter gain, K_k, depends on the state error covariance and the measurement residual covariance. For measurements made in polar coordinates, we wish to keep the measurements and the covariance of the measurement residual in the polar frame. This is the basic theory behind the Dual Extended Kalman Filter. The state model and the state error covariance are maintained in the Cartesian frame, while the measurement and the covariance of the measurement residual are maintained in the spherical coordinate system. In this manner, the measurement noise processes do not undergo any non-linear transformation, and the Kalman Filter retains its optimality. However, with two coordinate systems maintained at the same time, there must be some way to fuse the data from one frame to another. This is the purpose behind the observation matrix. The observation matrix, H_k, is used to map the state frame into the measurement frame.

It should be noted that this filter is not implemented for the BDM algorithm described here. Since smoke plume measurements remain in a relatively fixed position over a long time period, the algorithm described herein translates all measurements to the Cartesian frame before feeding them to the Kalman Filter. As the range to the measurements remains static, the resolution cell and measurement uncertainties also remain fixed and are approximated to be consistent throughout the state estimates.

4.7.2.1 State and Covariance Models Explained

The state model we will be estimating is the targetŠs position and velocity. Each of state dimensions are assumed to be statistically independent. In other words, we assume that the targetŠs position or velocity in the x-dimension is not affected by its position or velocity in any other dimension. The state matrix is a [6,1] matrix of the form

$$X_k = \begin{bmatrix} x_k & \dot{x}_k & y_k & \dot{y}_k & z_k & \dot{z}_k \end{bmatrix}^T . \tag{4.7.11}$$

The measurements are made in a spherical coordinate system, referenced to the radar boresight direction perpendicular to the plane of the array front. The four measurements taken are the targetŠs range, bearing, elevation, and range-rate. As with the state model, each of the measurements is assumed to be statistically independent from one another, a fact that will become apparent when the measurement error matrix, R_k, is given. The measurement matrix is a [4,1] matrix of the form

$$Z_k = \begin{bmatrix} r & \theta & \phi & \dot{r} \end{bmatrix}^T . \tag{4.7.12}$$

The measurement noise is assumed to be a zero-mean noise process having a covariance matrix equal to

$$R_k = \begin{bmatrix} \sigma_r^2 & 0 & 0 & 0 \\ 0 & \sigma_\theta^2 & 0 & 0 \\ 0 & 0 & \sigma_\phi^2 & 0 \\ 0 & 0 & 0 & \sigma_{\dot{r}}^2 \end{bmatrix} \tag{4.7.13}$$

where σ_r^2, σ_θ^2, σ_ϕ^2, and $\sigma_{\dot{r}}^2$ are the measurement accuracies, or the variances of the measurements. So, upon examination of (4.7.13) we see that each of the measurements is statistically independent from one another.

The observation matrix maps the state space onto the measurement space. In Cartesian coordinates where the transformation from the state to the measurement space is linear, this matrix structure is rudimentary, as shown in (4.7.12). In this application, we need to perform a non-linear coordinate transformation from the state space into the measurement space. By keeping the measurement space in polar coordinates, we can refrain from performing a non-linear transformation that would distort the white-noise process. We perform this transformation by a linear estimate of the target motion around the most recently predicted state. Here, the observation matrix is given by

$$H_k = \begin{bmatrix} x/r & 0 & y/r & 0 & z/r & 0 \\ y/r_h^2 & 0 & -x/r_h^2 & 0 & 0 & 0 \\ \frac{-xz}{r^2 r_h} & 0 & \frac{-xz}{r^2 r_h} & 0 & 1/r & 0 \\ H_{dk}(1) & x/r & H_{dk}(3) & y/r & H_{dk}(5) & z/r \end{bmatrix} \tag{4.7.14}$$

Where

$$H_{dk}(1) = \frac{(y^2+z^2)\,\dot{x} - (y\dot{y}+z\dot{z})\,x}{r^3} \tag{4.7.15a}$$

$$H_{dk}(3) = \frac{(x^2+z^2)\,\dot{y} - (x\dot{x}+z\dot{z})\,y}{r^3} \tag{4.7.15b}$$

$$H_{dk}(5) = \frac{r_h^2\dot{z} - (x\dot{x}+y\dot{y})\,y}{r^3} \tag{4.7.15c}$$

$$r = \sqrt{x^2+y^2+z^2} \tag{4.7.15d}$$

$$r_h = \sqrt{x^2+y^2} \tag{4.7.15e}$$

Here, the position variables (x, y, z) are the positions in the most recently predicted state, $X_{k|k-1}$. An important point to note is that although the use of dual coordinate systems alleviates the problem of the non-linear coordinate transformation, this linearized mapping is not optimal under all measurement noise models. For instance, [98] states that the performance of the Extended Kalman Filter degrades when the target measurement noise has the following characteristic

$$\frac{r\max\left[\sigma_\theta^2, \sigma_\phi^2\right]}{\sigma_r^2} \geq 0.4 \tag{4.7.16}$$

Where σ_θ^2, σ_ϕ^2, and σ_r^2 are the variances of the measurement noise from (4.7.13) at time k. Upon examination of (4.7.16), we see that the performance of the Extended Kalman Filter will degrade at far ranges if, for example, the radar system has very poor angular accuracy. We can think of the observation matrix for this case as an approximation to the partial derivative of the standard Cartesian-to-spherical coordinate transformations.

4.7.3 Track Initiation Logic

On each scan, radar detections must be processed to form new tracks or associate to existing tracks. This is known as *track initiation and data association*. Track initiation for a declared detection begins by attempting to correlate the detection with an existing track. Detections which do not correlate are declared as new tracks. Since the presence of false detections can result in false tracks, new tracks are first declared *tentative* until enough detections have been associated to the track on subsequent scans. This is known as an M of N track initiation policy [108, pp. 7.28–7.37], where tracks are tentative until at least M detections out of the previous N observations have associated to the track. Once the M of N criterion is met, the tracks are declared *firm* and are maintained by the radar system. Tentative tracks not confirmed within a designated observation window are subsequently dropped. For the M of N track

initiation logic, the probability that a track is initiated can be calculated from the binomial distribution for M successes in N trials. For a single-look target probability of detection of P_d, the probability of establishing a firm track is

$$P_t = \sum_{i=0}^{\lfloor N \rfloor} \binom{n}{k} P_d^i (1 - P_d)^{(M-i)} \tag{4.7.17}$$

Where the $\lfloor \rfloor$ symbol is the *floor* operation, equal to the greatest integer that is less than or equal to N. Note how the track probability in (4.7.17) is taken from the total number of M detections out of a possible N observations, which does not require M consecutive detections (in which case the track probability would reduce to a cumulative product). For a probability of detection of 95 % ($P_d = 0.95$) with M and N set to 4 and 5, respectively, the probability of firm track is 98 %. If, however, the probability of detection is just 75 %, the probability of establishing a firm track reduces to 63 %.

Detections are correlated to existing tracks via a distance threshold. Rather than using the Euclidean or geometric distance, this implementation uses the statistical distance to test whether a detection associated to a track. Detections are correlated to a track if they are within the correlation gate of the most recent track position state estimate. For radar measurements in spherical coordinates, the statistical distance is computed as

$$d_m = \sqrt{\frac{r - r_m}{\sigma_r^2} + \frac{\theta - \theta_m}{\sigma_\theta^2} + \frac{\phi - \phi_m}{\sigma_\phi^2}} \tag{4.7.18}$$

Where the subscripts k and m denote the track and measurement position estimates, respectively, and (σ_r^2, σ_θ^2,σ_ϕ^2) are the state variance estimates in each dimension. For

Kalman Filter algorithms, this distance measure can be computed directly from the state matrices in (4.7.3) as

$$d_m = \sqrt{\tilde{Z}_k^T S_k^{-1} \tilde{Z}_k} \tag{4.7.19}$$

This statistical distance, also known as the *Mahalanobis* distance [72], is a measure of whether the detection falls within the confidence limits of the track error covariance.

Since the Kalman Filter assumes measurement and process noise as zero-mean Gaussian distributions, the error covariance of the state estimates will follow a similar distribution. The statistical distance as the squared summation of these error terms is then a Chi-Square probability density function where the degrees of freedom is the dimensionality of the position estimate. The distance threshold can be computed from the inverse Chi-Square density function. For example, for a correlation gate corresponding to the 95 % confidence interval about the state estimates, detections are associated if $d_m < 7.81$ ($\chi^-1(0.95) = 7.81$).

4.8 Elliptical Approximation Technique

Suppose you have a collection of normally-distributed data points in two dimensional space, [x,y]. Intuitively, one could approximate a shape to this cluster of points, such that all data points are contained within the shape. The problem then is which shape to use and how to approximate such a shape to the data. This sections describes the elliptical approximation technique to a collection of data points.

We begin by assuming that the cluster of points can be approximated by an ellipse. The radii of the ellipse can be thought of as being proportional to the density, or variance, of the cluster in each dimension. The covariance matrix, Cov$[x, y]$ provides an estimate of the cross- and co-correlation terms as

$$\mathrm{Cov}\,[x, y] = \begin{bmatrix} \sigma_x^2 & \sigma_{x,y} \\ \sigma_{y,x} & \sigma_y^2 \end{bmatrix} \tag{4.8.1}$$

If x and y represent a collection of points which can be approximated by an ellipsoidal shape, the eigenvalues of (4.8.1) are proportional to the major and minor axis length of the ellipse, and the angle of the eigenvectors are the orientation. For major and minor axial lengths of a and b, respectively, the edge of the ellipse containing the points is given by

$$\left(\frac{x}{a}\right)^2 + \left(\frac{y}{b}\right)^2 = s \tag{4.8.2}$$

Where s is the scale of the ellipse. Since x and y are both normally distributed random variables with zero mean about the centroid of the ellipse, their squared sum, s, is a Chi-Square distribution with 2 degrees of freedom (or 3 degrees of freedom is this case is extended to three dimensions). The edges of the ellipse therefore represent a chosen confidence limit, p, of the data points, where the probability a data point in $[x_n,y_n]$ is contained within s is less than p. From this fact, s can be computed from the inverse Chi Square distribution for a given confidence limit p. In this manner, the equation of the ellipse approximated by the smoke plume using 95 % confidence intervals on the distribution of data points can be calculated. The ambient wind direction is taken as the orientation of the major axis of the approximated ellipse.

CHAPTER 5

ADAPTIVE SCANNING TECHNIQUES

X-band radar systems are becoming increasingly popular for meteorological and remote sensing operations. As X-band radars can achieve the same angular resolution as lower frequency S- and C-band systems at a fraction of the aperture size, they are well-suited to localized surveillance in inhospitable terrain or urban areas. With the next-generation systems focusing on phased array radars for weather sensing, however, more research and development must be performed before networks of such systems could be used to augment or replace the current and next-generation infrastructure. Additionally, any future capability system would have to simultaneously support a wide variety of missions, from weather and hydrologic forecasting to aircraft surveillance. Therefore, the amount of time dedicated to weather sensing must be highly optimized to meet top-level data quality requirements, while allowing other radar missions to be fulfilled. This research presents a quantitative analysis of the data quality of an X-band phased array radar, specifically focusing on characterizing the standard deviation of pulse-pair product estimates. Simulations and analysis are presented that compare the standard deviation from theoretical, simulation, and radar data. The results are then extrapolated to estimate the minimum volume scan time required for X-band phased array radars to meet a set of notional data quality requirements. Based on these results, this research proposes a new set of reduced data quality requirements that limit the scan time needed to support the weather surveillance mission on future capability systems.

5.1 Introduction

The future of radar surveillance in the United States is moving towards multi-mission support and operational awareness across a multitude of disciplines, organizations, and entities. Any next-generation system will have to simultaneously support weather, hydrologic, and climate forecasting for the National Weather Service (NWS), asset protection and situational awareness for the Department of Defense (DoD), mesoscale phenomena for the Federal Aviation Administration (FAA), cooperative and non-cooperative aircraft surveillance for the Department of Homeland Security (DHS), and many more applications [41]. Active phased array radars are the optimal system choice to meet these requirements, due to their flexible scanning and waveform capabilities, combined with reduced maintenance and recurring costs from the solid state architecture used.

While phased arrays represent the next logical step in deployed systems, meeting the requirements for every mission with traditional scanning strategies will be a challenge. Notional requirements for terminal and global weather surveillance need scan volume update rates on the order of 1 min to 2 min [110, 38], while maintaining track update rates from 5 s to 10 s on up to hundreds of targets in view. Initial trade studies on the scanning strategy in phased array radars indicate that traditional scanning will be inefficient to meet the update and refresh rates for both weather and target applications. Yu et al. [119] proposed a beam multiplexing strategy as an implementation of the Independent Pair Sampling (IPS) technique to reduce the integration time while maintaining the same data quality. Zrnic et al. [123] proposed a novel strategy known as *within-the-pulse* beam multiplexing that rapidly transmits multiple pulses at different frequencies in different directions and uses Digital Beam Forming (DBF) on receive to sample the radar echoes simultaneously from each scan angle. Galati and Pavan [44] studied the scan times for different volume scan strategies, and pro-

Table 5.1: Multifunction Phased Array Radar (MPAR) notional weather surveillance requirements. Note that these requirements are in the context of the S-band radars currently operated by the NWS.

Product	σ_{max}				Δ_{max}			
		SNR (dB)	σ_v ($\mathrm{m\,s^{-1}}$)	ρ_{hv}		SNR (dB)	σ_v ($\mathrm{m\,s^{-1}}$)	ρ_{hv}
Reflectivity (Z_h)	1.8 dBZ	10	4		1.0 dBZ			
Radial Velocity (v)	$1\,\mathrm{m\,s^{-1}}$	8	4		$0\,\mathrm{m\,s^{-1}}$			
Spectral Width (σ_v)	$1\,\mathrm{m\,s^{-1}}$	10	4		$0.2\,\mathrm{m\,s^{-1}}$	10	12	
Differential Reflectivity (Z_{dr})	0.3 dB, $\theta_{el} < 20°$	20	2	0.99	0.1 dB ($Z_{dr} < 1$ dB), else $0.1 Z_{DR}$			
Copolar Corr. Coefficient (ρ_{hv})	6E−3, $\theta_{el} < 20°$	20	2	0.99	0.001	20	2	0.99
Differential Phase (Φ_{DP})	2.5°, $\theta_{el} < 20°$	20	2	0.99	0°			
Signal to Noise Ratio (SNR)	2.0 dB	0	4		1.0 dB			

posed the use of DBF with fan beams on transmit and pencil beams on receive to meet weather and target surveillance requirements.

These techniques are designed to reduce the volume scan time while maintaining the same data quality achieved with the current operational Next-Generation Radar (NEXRAD) system. Table 5.1 lists a set of notional requirements for weather observation, established for the MPAR system [110]. The requirements list the required standard deviation and bias for each measured weather product, which are a function of the measured Signal to Noise Ratio (SNR), spectral width, and copolar correlation coefficient.

Phased array radars face many challenges in meeting these requirements. As polarimetric phased arrays scan off boresight, coupling between the polarizations causes bias errors in differential reflectivity, copolar correlation coefficient, and differential phase [122]. Because of these biases, system calibration is more difficult for a phased array because the array gain, beamwidth, and system phase potentially require beam-to-beam correction factors. Mismatch in the co- or cross-polar fields and beam pointing errors can further increase bias in the polarimetric products [45]. Further-

more, the implementation of the Alternate Transmit/Alternate Receive (ATAR) polarization pulsing scheme has been shown to contribute additional variability and bias when compared to the Simultaneous Transmit/Simultaneous Receive (STSR) scheme when tested on the NEXRAD Weather Surveillance Radar (WSR-88D) [76].

The purpose of this research is to perform a quantitative analysis of the standard deviation of the weather product estimates for an X-band phased array radar employing the ATAR pulsing scheme. Results from the analysis are used to determine how well X-band phased arrays can meet the data quality requirements in Table 5.1. Section 5.2 reviews the scanning strategies that will be implemented and tested with the phased array radar. Section 5.3 describes the test methodology used to perform the analysis, which includes a description the procedure used to estimate the standard deviation of simulated and live radar data. In Section 5.4, theoretical approximations for the standard deviation of the polarimetric products will be compared against simulation. In Section 5.5, live radar data results are presented and compared to theoretical approximations. The results and implications to X-band phased array weather radars are discussed in Section 5.6. Section 5.7 provides a summary and concluding remarks. To limit the scope and number of data sets presented herein, the analysis was only performed on estimates of reflectivity (Z_h), differential reflectivity (Z_{dr}), copolar correlation coefficient (ρ_{hv}), and differential phase (Φ_{DP}).

5.2 Background

Two categories of scanning techniques were implemented for this analysis: Contiguous Pair Sampling (CPS) and Independent Pair Sampling (IPS). Contiguous Pair Sampling (CPS) is the traditional scanning strategy employed by most systems whereby a contiguous series of M pulses at a Pulse Repetition Time (PRT) of T_s seconds are transmitted in succession for N_r radials. The total scan time in CPS is therefore equal to $N_r M T_s$. IPS is an alternate technique that transmits L pairs of

pulses at a PRT of T_s seconds displaced in time by an inter-dwell period of T_d seconds for N_r radials [119]. This results in a total scan time of $N_r L T_d$. The purpose of IPS is to decorrelate pulse-pair estimates from one another in time to reduce the variance in the final estimate. This can easily be derived from basic statistical analysis techniques. Consider discrete sample measurements of a random variable x. The sample variance of a linear combination of i estimates chosen from $\hat{x}$ depend on both the variance of $\hat{x}_i$ and the cross-covariance terms between each sample [69]

$$\mathrm{Var}\left[\sum_i \hat{x}_i\right] = \sum_i \mathrm{Var}\left[\hat{x}_i\right] + 2\sum_i \mathrm{Cov}\left[\hat{x}_i, \hat{x}_j\right]. \tag{5.2.1}$$

From (5.2.1), we see that the variance in the estimate will increase if the sample measurements are correlated ($\mathrm{Cov}\left[\hat{x}_i, \hat{x}_j\right] > 0$). The purpose of IPS is to decorrelate the sample estimates in time so that the last term on the right-hand side of (5.2.1) goes to zero, and the variance of the estimate depends only on the sum of the variances of each sample. Assuming that the Doppler spectrum of received samples has a Gaussian shape (as in (3.2.6)), the decorrelation time can be directly estimated from (3.2.9). Figure 5.1 compares the decorrelation time at X-band (9410 MHz, 3 kHz PRF) and S-band (2750 MHz, 1 kHz PRF) for signals having a true spectral width of $1\,\mathrm{m\,s^{-1}}$. The time for the correlation coefficient to reduce to less than 0.03 (shown as the dotted line in the figure) is over three times lower at X-band (6.6 ms) than at S-band (22 ms).

Practically, IPS is implemented by computing the arithmetic average of pairs of correlations at each radial. Yu et al. [119] extended IPS to a technique known as Beam Multiplexing (BMX), where the radar is tasked to other azimuth locations during the inter-dwell period, and demonstrated a 2 to 4 times improvement in the standard deviation when compared to CPS. However, this improvement came at the cost of increased bias in spectral width. As correlation terms in IPS are collected from short

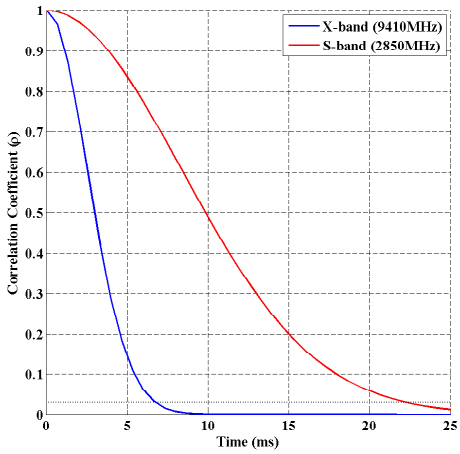

Figure 5.1: Comparison of the decorrelation time of received weather samples at X-band (9410 MHz) and S-band (2750 MHz), assuming a true spectral width of $1\,\mathrm{m\,s^{-1}}$ and Pulse Repetition Frequencys (PRFs) of 3 kHz and 1 kHz, respectively. The time for the correlation coefficient to reduce to less than 0.03 (shown as the dotted line) is over three times lower at X-band (6.6 ms than at S-band (22 ms).

pairs or triplets [33] of pulses, spectral leakage in the covariance estimators creates unwanted bias.

To estimate this bias in the context of polarimetric radar, we first extend the technique to the displacement of L *groups* of M_L pulses displaced in time. Correlation terms are then gathered for each group, and pulse-pair estimates are computed from the arithmetic average of LM_L correlation terms. This technique can be derived from from (3.4.2) as

$$\hat{S}_h = \frac{\sum_{l=0}^{L-1}\left\{\frac{1}{M_L}\sum_{m=0}^{M_L-1}|V_{hh}[m]|^2 - \hat{N}_h\right\}}{L} \tag{5.2.2a}$$

$$\hat{S}_v = \frac{\sum_{l=0}^{L-1}\left\{\frac{1}{M_L}\sum_{m=0}^{M_L-1}|V_{vv}[m]|^2 - \hat{N}_v\right\}}{L} \tag{5.2.2b}$$

$$\hat{R}^n_{hh} = \frac{\sum_{l=0}^{L-1}\left\{\frac{1}{M_L}\sum_{m=0}^{M_L-1}V_{hh}[2m]^* V_{hh}[2m+n]\right\}}{L} \tag{5.2.2c}$$

$$\hat{R}^n_{vv} = \frac{\sum_{l=0}^{L-1}\left\{\frac{1}{M_L}\sum_{m=0}^{M_L-1}V_{vv}[2m+1]^* V_{vv}[2m+1+2n]\right\}}{L} \tag{5.2.2d}$$

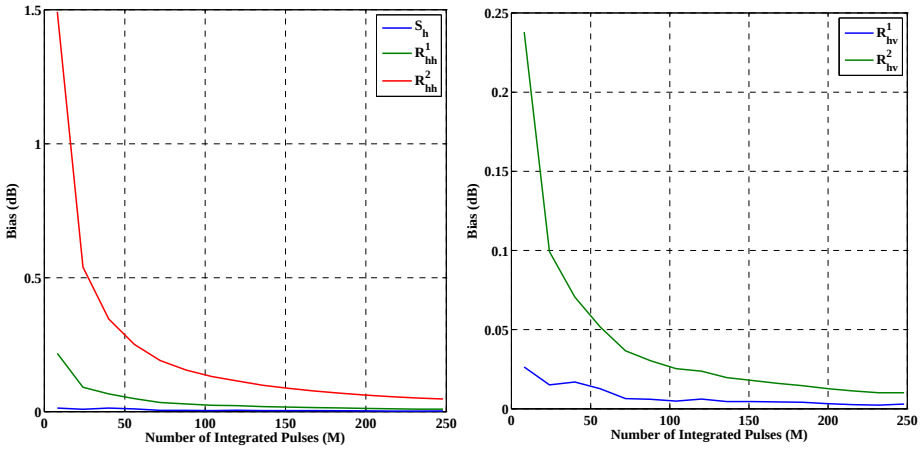

(a) (b)

Figure 5.2: Simulated bias in (a) co-polar and (b) cross-polar correlation estimates as a function of the number of integrated pulses (M). Simulation was setup to generate data having a copolar correlation coefficient of 0.99, a true spectral width of $2\,\mathrm{m\,s^{-1}}$, and assumed a 3 kHz PRF. These results show that correlation estimates from short-pulse CPIs introduce significant bias at higher order time lags.

Where the summation is taken across each of the L groups of M_L pulses each, and a rectangular window is used. The cross-polar correlation terms (not shown) can be similarly derived.

The source of errors in IPS can be found by analyzing the effect of windowing and segment length on the pulse-pair estimates. To this end, the following Monte Carlo experiment was performed. On each trial, weather signals were generated as 512-pulse H- and V-polarization timeseries in the ATAR polarization pulsing scheme (using the technique in Section 3.6). All data was generated with a copolar correlation coefficient of 0.99, a true spectral width of $2\,\mathrm{m\,s^{-1}}$, and assumed a 3 kHz PRF. Correlation terms were then gathered for different Coherent Processing Interval (CPI) lengths from 8 pulses to 512 pulses. For each segment, the magnitude and phase of the correlation terms were collected. After all trials were complete, the bias was computed with the truth data taken as the correlation terms from the maximum CPI length. The simulation was run with a minimum of 100k trials.

The results of the Monte Carlo simulation are shown in Figure 5.2 for estimates of the magnitude of the co- and cross-polar correlation terms (R^n_{hh}, R^n_{hv}, and R^n_{vh}). The bias is negligible in the power estimates (S_h), but increase dramatically at higher lags. As expected, the bias for all estimates falls off as the number of pulses in the CPI increases. These results provide insight into the source of bias in spectral width observed in previous work [119, 33]. Polarimetric products that are a function of power estimates (Z_h and Z_{dr}) are expected to be unbiased in IPS because the number of integrated pulses introduces negligible bias. However, any pulse-pair estimate which depends on higher-order co- or cross-polar correlation terms will contain unwanted bias. Spectral width estimates are biased because it depends on R^1_{hh} (as in (3.4.9)) or R^2_{hh} (as in (3.4.11)). Furthermore, any product which depends on higher-order cross-polar correlation terms (R^1_{hv} or R^1_{vh}) will be biased, including copolar correlation coefficient (ρ_{hv}) and differential phase (Φ_{DP}).

The IPS strategy can be implemented in different ways. Besides displacing returns in time, the returns can also be displaced in frequency. This technique, known as frequency diversity or Frequency Multiplexing (FMX), works by shifting the center frequency of the transmit waveform by an amount equal or greater than the receiver bandwidth. Thus, returns at one frequency will be independent of terms from another frequency. Pazmany et al. [90] employed this frequency diversity scheme to speed up volume scan time for a rapidly rotating mechanical radar by shifting the center frequency after each group of 12 pulses.

Based on the previous analysis, it is hypothesized that the IPS scanning strategy will not show significant improvement for X-band phased array radars as was observed at S-band. The rationale for this hypothesis is as follows. First, the decorrelation time at X-band is three times shorter than at S-band, so the *effective* number of independent samples in a CPI will inherently be higher. Second, the use of ATAR requires a minimum of 4 pulses per group to gather higher order correlation terms (R^1_{hh} and

R_{hv}^1), so the number of averaged groups is reduced. Because the improvement in standard deviation from IPS is proportional the number of independent groups averaged, reducing the number of groups will increase the estimated variance. Furthermore, to restrict the bias in IPS to acceptable levels, more than 4 pulses may be required. This will further reduce any observed improvement.

5.3 Test Methodology

Due to the space-time variability of weather, measurement of the standard deviation of the produce estimates must be carefully considered, and different techniques have been employed in the past. Liu et al. [70] averaged radar data along a single radial in a 6 s interval and computed the standard deviation and 95 % confidence intervals of copolar correlation coefficient. Yu et al. [119] used a similar technique for data collected from a passive S-band phased array radar. They estimated the mean velocity vector of the storm and analyzed data over time intervals small enough to assume weather was a stationary process. The technique used here builds upon these methods.

To accurately estimate the standard deviation of the polarimetric products, storm motion must be accounted for. For weather moving purely tangential to the radar at an advection speed of $24\,\mathrm{m\,s^{-1}}$, assuming a range resolution and azimuth beamwidth of 120 m and 1.8°, respectively, it will take 5 s to 10 s for the scatterers in one resolution volume to be replaced (over a range extent from 8 km to 35 km). For weather moving radially, it will take just 5 s. Since each scan takes up to 7.8 s to complete, the motion of the storm between scans must be used to align resolution volumes for accurate analysis.

For weather features moving with a mean velocity vector of $\vec{v} = [v_x, v_y, v_z]\mathrm{m\,s^{-1}}$, the total displacement between scans can be estimated as

$$\vec{d} = -\hat{v}\delta_t \tag{5.3.1}$$

Where δ_t is the time between scans. If we assume that the storm tangential motion is negligible ($\vec{v}$ normal to array boresight), this displacement can be written in terms of the range and radial velocity

$$\delta R = -\hat{v}T_{sc} \tag{5.3.2}$$

Where T_{sc} is the total scan time (s). Equation (5.3.2) can be rewritten in terms of range resolution (δR_0)

$$\delta R_p = -\frac{\hat{v}T_{sc}}{\delta R_0}. \tag{5.3.3}$$

Here, the amount of radial storm displacement is expressed as a fraction of the radar range resolution. This is the primary source of error in the estimation procedure. Theoretical approximations for the standard deviation of products are derived from empirical analysis, but measuring in practice requires an adequate sample size. That is, to estimate the standard deviation achieved within a particular resolution cell, we require *repeated* measurements taken in that resolution cell over time. However, when the scatterers displace from one resolution cell to the next, differences in the backscattered echoes change the measured SNR, spectral width, or correlation coefficient. Thus, we recognize two sources of variability in our measurements: signal and statistical. Signal variability is caused from the natural variations in the precipitation features over an area, whereas statistical variability is from the pulse-pair estimates themselves. This technique attempts to measure the latter, but the former is a source of error for these measurements.

While it is impossible to completely account for signal variability, steps can be taken to minimize its effects on the variance estimation here. When δR_p exceeds 0.20, range bins on the current scan are shifted so as to align to the bins on the previous scan. In other words, at a range bin spacing of 24 m and range resolution of 120 m,

when 20 % (or one range bin's worth) of the scatterers are replaced in a resolution volume between scans, the range bins are shifted so that the scatterers from the same resolution volume are aligned. This technique has been used previously in variance analysis [33].

After motion compensation, the standard deviation is computed along each range bin in the sliding window for each polarimetric product analyzed. These measurements are grouped by measured SNR and spectral width at that bin. Range bin standard deviations are averaged along each radial and scan to produce the final estimates for the products. Each radar data set contains at least 50 radar azimuth scans (over 390 s). The standard deviation is calculated at each range gate within a 60 s sliding window (≈8 radar scans).

5.4 Simulation

Before live data was collected, a simulation model was developed both to predict and verify experimental results. This section presents the simulation results which compare theoretical (empirical) approximations for the standard deviation against simulated performance. The simulation generates synthetic In-phase and Quadrature (IQ) data by passing white Gaussian noise through a shaping filter [15]. For a detailed description of the simulation procedure, see Section 3.6. To test the against data quality requirements in Table 5.1, a Monte Carlo simulation was run to generate timeseries data having SNRs of [0, 8, 10, 20]dB and spectral widths of [2, 4]m s^{-1}, for a total of 8 different cases. One each iteration, at least 100 k iterations were run.

Figure 5.3 shows plots of the standard deviation of reflectivity ($SD(Z_h)$), differential reflectivity ($SD(Z_{dr})$), copolar correlation coefficient ($SD(\rho_{hv})$), and differential phase ($SD(\Phi_{DP})$). Approximations for the standard deviation at arbitrary SNR were used to estimate theoretical performance [76]. Since no closed form solution exists for

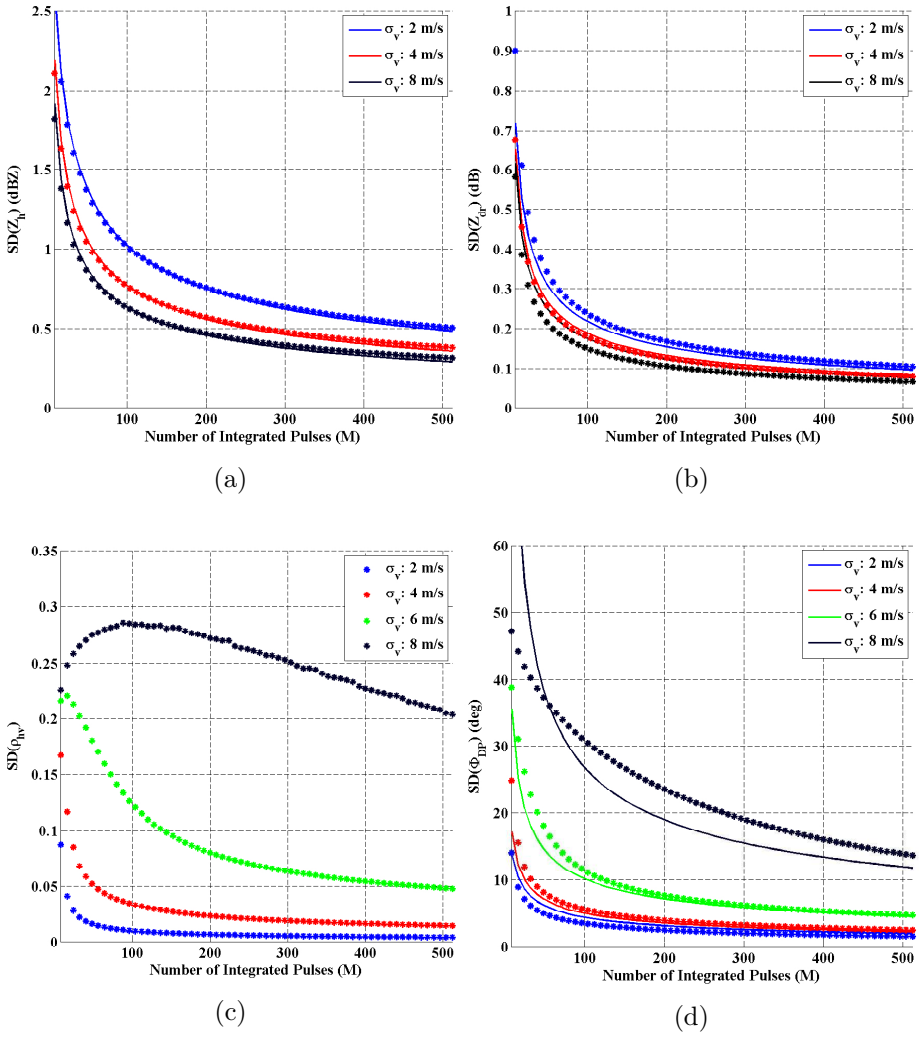

Figure 5.3: Plots of simulated (∗) and theoretical (—) results versus number of samples for standard deviation of (a) reflectivity, (b) differential reflectivity, (c) copolar correlation coefficient, and (d) differential phase. This data was simulated assuming an X-band (9410 MHz radar operating with a 3 kHz PRF. The simulated SNR for each case was taken from the test conditions for the variable as listed in Table 5.1.

the standard deviation of copolar correlation coefficient, only simulation results are relied on.

Inspection of Figure 5.3 shows that the simulation agrees well with theoretical approximations, especially at low spectral width. In agreement with previous work [76], the standard deviation of correlation coefficient and differential phase increase dramatically at large spectral widths. Results indicate that when the normalized

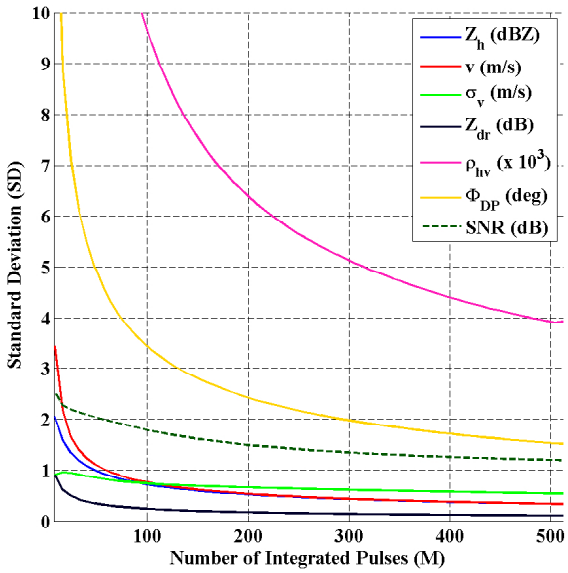

Figure 5.4: Plots of simulated results for all polarimetric products, using the conditions for SNR, spectral width, and copolar correlation coefficient listed in Table 5.1. The simulation was setup to generate synthetic IQ data from an X-band (9410 MHz) radar implementing the ATAR polarization scheme.

spectrum width ($\sigma_{vn} = 2\sigma_v T_s/\lambda$) exceeds 0.25, $SD(\Phi_{DP})$ and $SD(\rho_{hv})$ increase dramatically. We therefore hypothesize that X-band radars implementing the ATAR scheme operating close to a 3 kHz PRF will produce poor quality returns for spectral widths above 5 m s^{-1} to 6 m s^{-1}.

To estimate the performance against all polarimetric products, the simulation was run iteratively for each SNR, spectral width, and copolar correlation coefficient condition listed in Table 5.1. The measured standard deviations for each products as a function of the number of integrated pulses is shown in Figure 5.4. From inspection of the data, at least 64 total pulses per beam (21.3 ms at 3 kHz PRF) are required to meet the requirements in Table 5.1 for the single-polarization moments (reflectivity, velocity, and spectral width). However, at least 224 pulses (74.7 ms) are required to meet all data quality requirements for the polarimetric products.

IPS returns were also simulated by processing sparse groups of pulses from simulated IQ data. On each Monte Carlo iteration to simulate a total of L groups of M_L pulses, additional *fill* pulses were generated between each group. The amount

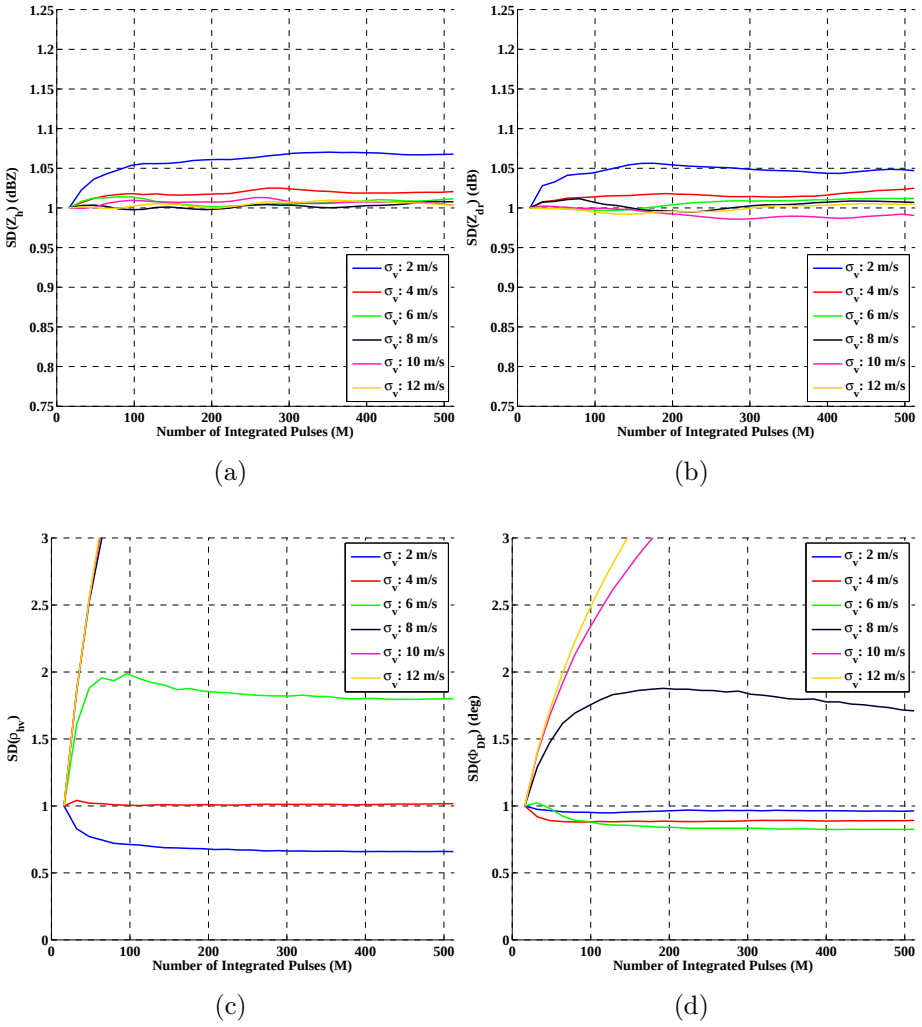

Figure 5.5: Plots of improvement factor in standard deviation of simulated IPS over CPS scanning strategies as a function of the number of integrated pulses (M) for different spectrum widths from $2\,\mathrm{m\,s^{-1}}$ to $12\,\mathrm{m\,s^{-1}}$. Plots show the improvement in (a) reflectivity, (b) differential reflectivity, (c) copolar correlation coefficient, and (d) differential phase. Improvement factor is defined as the ratio of standard deviation in CPS to IPS. Values greater than one indicate that the standard deviation in IPS is better than CPS; values less than one indicate that it is worse.

of fill pulses was chosen such that each group was sufficiently decorrelated from one another. For each simulation trial, groups of 8 pulses ($M_L = 8$) were generated, with enough fill pulses between each group to allow the correlation coefficient to drop below 0.03 for the normalized spectral width being tested. For example, using the correlation coefficient from (3.2.9), a spectral width of $1\,\mathrm{m\,s^{-1}}$, and a 3 kHz PRF, at least 20 pulses are required to sufficiently decorrelate groups from one another.

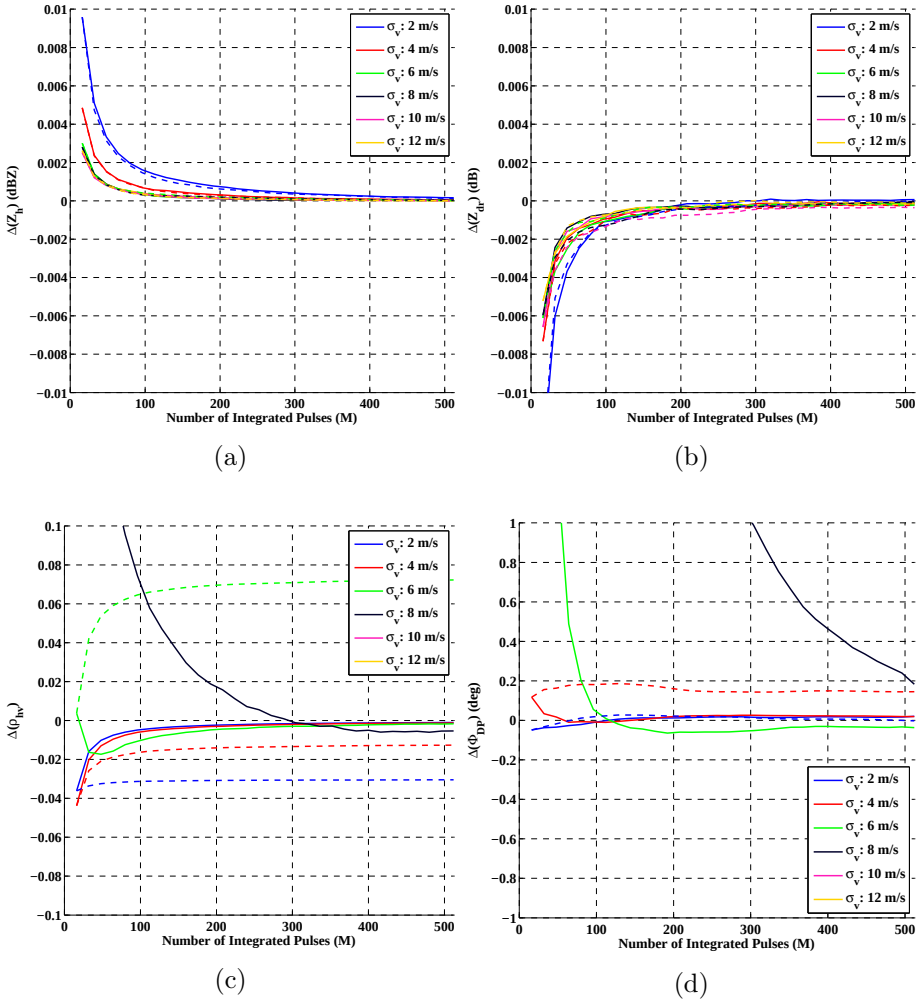

Figure 5.6: Plots of bias in simulated CPS (—) and IPS (– –) scanning strategies as a function of the number of integrated pulses (M) for different spectrum widths from $2\,\mathrm{m\,s^{-1}}$ to $12\,\mathrm{m\,s^{-1}}$. Plots show the bias in (a) reflectivity, (b) differential reflectivity, (c) copolar correlation coefficient, and (d) differential phase. Note that the bias in correlation coefficient and differential phase in (c) and (d) are above the plot limits for spectral widths greater than $6\,\mathrm{m\,s^{-1}}$ and $4\,\mathrm{m\,s^{-1}}$, respectively. IPS introduces significant bias for spectral widths above $4\,\mathrm{m\,s^{-1}}$ to $6\,\mathrm{m\,s^{-1}}$ in ρ_{hv} and Φ_{DP}.

Figures 5.5 and 5.6 show plots of the improvement factor in standard deviation and bias errors, respectively. Here, improvement factor is defined as the ratio of the standard deviation in CPS to IPS. Values greater than one indicate that the standard deviation in IPS is better than CPS; values less than one indicate that it is worse.

At narrow spectral widths ($\sigma_v \leq 2$), IPS shows above a 5 % improvement in reflectivity and differential reflectivity, with negligible improvement at higher spectral widths. Bias in reflectivity and differential reflectivity are less than 0.01 dB. This

is expected, since simulation results in Figure 5.2 predict negligible bias in power estimates for different CPI lengths.

Simulated improvement factors for ρ_{hv} and in Figures 5.6c and 5.6d are misleading, since IPS introduces significant bias at spectral widths above $2\,\mathrm{m\,s^{-1}}$ to $4\,\mathrm{m\,s^{-1}}$. Furthermore, CPS data are also biased above $6\,\mathrm{m\,s^{-1}}$, which agree with previous work. Melnikov and Zrnić [76] studied the bias in ATAR over STSR polarization pulsing schemes and demonstrated significant bias in ATAR at high spectral width.

5.5 Radar Data

To verify simulation and theoretical approximations, two experiments were performed. In the first experiment, the radar executed the CPS scanning strategy by transmitting a contiguous series of 256 total pulses (across both polarizations). IPS data was synthetically generated from the data set by selectively processing groups of 8-pulses in a radial. On each radial, the measured spectral width was used to determine the number of pulses to skip between groups to force independence between pulse-pair estimates. With 256 total pulses were per radial and measured spectral widths as low as $0.5\,\mathrm{m\,s^{-1}}$, at least 41 fill pulses were required at times. For this reason, IPS data was only available for up to $\lfloor 256/(8+41) \rfloor\, 8 = 40$ total pulses. In addition, the measured SNR, spectral width, and correlation coefficient were used to approximate the standard deviation from theoretical formulae [76]. Theoretical approximations at each range bin were averaged over all radials and scan, similar to the procedure described in Section 5.3.

The second experiment tested actual implementations of BMX and FMX scanning strategies. In this test, three different radar modes were setup and run concurrently. Table 5.2 lists each of the radar modes tested. The modes represent actual implementations of the (1) CPS, (2) FMX, and (3) BMX strategies. All radar modes operated with a 3 kHz PRF, a 55 µs 2.5 MHz) Linear Frequency Modulated (LFM)

waveform, with a range extent out to 35 km. Radar mode 1 was setup execute a contiguous series of pulses at sequential azimuth beam positions throughout the scan. Radar mode 2 executed a FMX strategy, where the center frequency was shifted by 5 MHz after each block of 16 pulses. With a receiver bandwidth through the Digital Receiver/Exciter (DREX) Digital Down-Converter (DDC) chain of 3.125 MHz and waveform bandwidth of 2 MHz, each block should be independent from one another. Product estimates were collected by averaging correlation terms gathered from each block (as in (5.2.2) with $M_L = 16$). Radar mode 3 executed the BMX strategy by transmitting short, 16-pulse CPIs at each radial, for a total scan time of 485.3 ms. Data from each azimuth beam position on successive scans was averaged to estimate the products. To mitigate unwanted second-trip echoes between the radials in BMX, azimuth beam positions were multiplexed in a scan. Section 2.4 describes the azimuth multiplexing technique.

Different CPI lengths from 16 to 128 were synthetically generated from the time-series by limiting the number of processed pulses for the CPS mode 1 or limiting the number of averaged groups for the IPS modes 1 and 2. The procedure described in Section 5.3 was used to estimate the standard deviation for each CPI length across all radar modes.

Figure 5.7 shows analysis of data from the first experiment during a 10 min time interval from the LPAR system in Amherst, MA from 27-May-2015. The red and dashed lines show measured and theoretical approximation for the standard deviation, respectively, for both CPS (blue line) and IPS (red line). Over this period, a squall line was observed moving in a North-Easterly direction towards the radar. Measured reflectivity within the storm exceeded 30 dBZ, with significant attenuation causing returns to eclipse within 15 km of the storm front. The storm was moving at a mean

[1]See Section 2.4 for a description of the multiplexed azimuth positioning technique.

Table 5.2: List of radar modes executed concurrently to compare CPS and IPS scanning strategies implemented on the Low-power Phased Array Radar (LPAR) system. For each radar mode, the *period* and *burst* fields control how often each radar mode is executed and how long it runs for. A zero burst value indicates that the radar mode is executed once every *period* seconds, and ∞ indicates that the mode should be run continuously. Radar modes 1 and 2 were executed once every 20 s, and mode 3 was run continuously.

ID	Strategy	Description	Period (s)	Burst (s)	No. Pulses (M)
1	CPS	Fixed frequency, sequential azimuth positioning	20	0	128
2	FMX	Frequency diversity, sequential azimuth positioning	20	0	128
3	BMX	Fixed frequency, multiplexed azimuth positioning[1]	∞	∞	16

radial velocity of $22\,\mathrm{m\,s^{-1}}$, and the maximum observed spectral width was $5\,\mathrm{m\,s^{-1}}$. Figure 5.7 shows the mean and standard deviation of $SD(Z_h)$, $SD(Z_{dr})$, $SD(\rho_{hv})$, and $SD(\Phi_{DP})$ during this event. Data was thresholded at 10 dB (Z_h) and 20 dB (Z_{dr}, ρ_{hv}, and Φ_{DP}).

Results show good agreement with theoretical approximations. Average $SD(Z_h)$ shows slight deviation from theoretical, particularly at longer integration times. Since reflectivity is uncorrected for attenuation, there is likely additional variability as the signals attenuate through the storm. Differential reflectivity and differential phase track well to theoretical approximations as well, and although areas of high spectral width ($> 5\,\mathrm{m\,s^{-1}}$) were observed, these did not appear to detrimentally affect the measured standard deviation. Results indicate that $SD(Z_h)$ in IPS is up to 12 % lower than in CPS, but there is no noticeable difference in $SD(Z_{dr})$. While $SD(\rho_{hv})$ appears to be lower in IPS, this result is misleading since the mean bias in ρ_{hv} (not shown) over the data set was -0.12. So, while the standard deviation was reduced, the significant bias degrades the IPS data. Standard deviation of differential phase

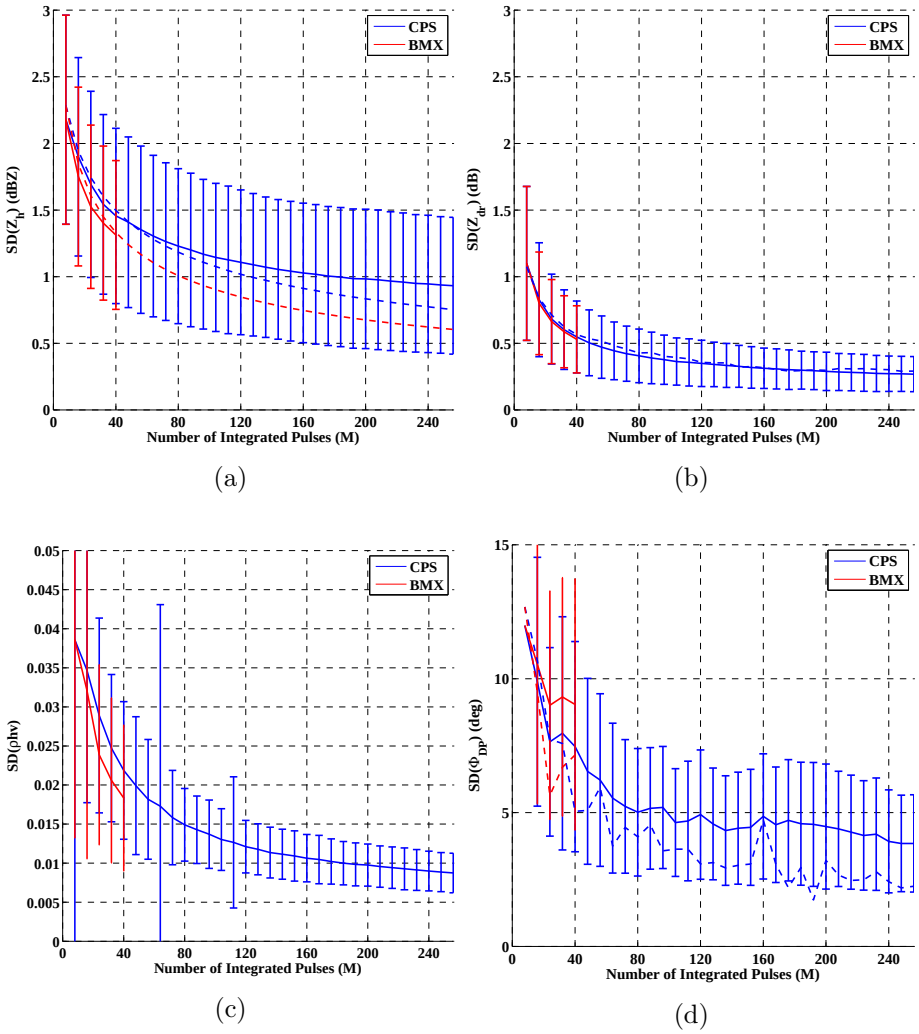

Figure 5.7: Measured (—) and theoretical (– –) standard deviations of (a) reflectivity, (c) differential reflectivity, (c) copolar correlation coefficient, and (d) differential phase for the precipitation event on 27-May-2015. Data shows standard deviation from different CPI lengths for both CPS (blue) and IPS (red). IPS data was synthetically-generated from CPS data by selectively processing groups of displaced pulses.

also appears to be higher than theory, which could be attributed to the unfolding algorithm used[2].

Figure 5.8 shows analysis of data from the second experiment performed during a 12 min time interval from the LPAR system on 22-April-2015. As in the first experiment, $SD(\rho_{hv})$ from both the IPS strategies, FMX and BMX, appears on first

[2]see Section 3.4 for a description of the differential phase unfolding algorithm

inspection to show significant improvement. However, ρ_{hv} from both techniques again is heavily biased, from $-0.1\,\mathrm{f}$ to $-0.15\,$for FMX and BMX, respectively. Differential phase is also biased from 2.5° to 5° for each mode. As expected from simulation, reflectivity and differential reflectivity show negligible bias between the IPS and CPS strategies (less than 0.01 dB), but still show some improvement in standard deviation. Improvement in BMX here is higher than predicted in simulation, from 5 % to 15 %. This increase in improvement than observed in simulation can be attributed to a lower measured spectral width (from $0.5\,\mathrm{m\,s^{-1}}$ to $1.5\,\mathrm{m\,s^{-1}}$) during the precipitation event.

5.6 Discussion

Analysis of the simulation results, verified against theoretical approximations and radar data, show that a 74.7 ms dwell time (224 pulses at a 3 kHz PRF) would be required to meet the requirements in Table 5.1. While IPS scanning strategies do show a slight improvement (from 5 15%) in the standard deviation of reflectivity and differential reflectivity, the bias introduced in copolar correlation coefficient and differential phase estimates makes either FMX or BMX impractical for operational purposes. As noted in previous work [119], this bias is inversely proportional to the number of pulses per CPI in IPS. So, the bias could be reduced for a long enough CPI. However, this would then decrease the number of averaged groups (and thus the improvement factor).

To determine how these results apply to a practical system, a hypothetical 2D X-band phased array, electronically-steered in both azimuth and elevation, is used herein to extrapolate the minimum dwell times from a single CPI to a realistic volume scan. The system assumes 2° azimuth and elevation beamwidths (at boresight) and a volume coverage from a down range of 40 km, a maximum height of 30 000 ft, and an elevation coverage from 1° to 30°. The radials in the scan are aligned in a grid for

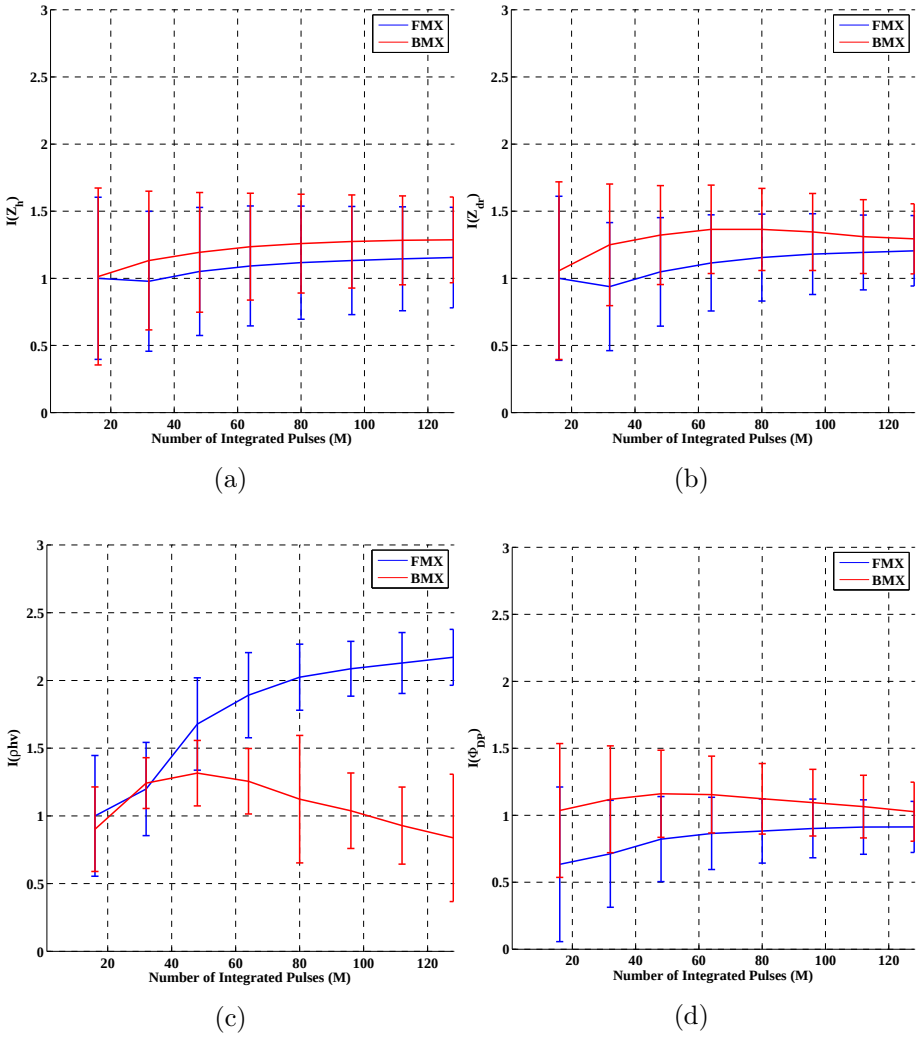

Figure 5.8: Measured improvement factor in standard deviation of (a) reflectivity, (b) differential reflectivity, (c) copolar correlation coefficient, and (d) differential phase for the precipitation event on 22-April-2013. Improvement factor is defined as the ratio of standard deviation from CPI to the BMX (red) and frequency hopping (blue).

simplicity, with 1° spacing in both azimuth and elevation. Note that this assumes no DBF and only the use of a pencil beam on transmit and receive. This architecture and system design is similar to the phased array described by Hopf et al. [57].

Table 5.3 lists the the beam positions, PRTs, and cumulative scan times for each elevation in the hypothetical volume scan. Note how the PRT is tailored at each elevation to only cover a range window and height out to 40 km and 30 000 ft, respectively. The dwell times at higher elevations can be reduced by restricting the range

Table 5.3: List of beam positions, PRTs, and range windows for the hypothetical phased array radar used in the analysis of X-band volume scan times. Note that the PRTs on each elevation tilt are optimized to scan out to a maximum horizontal down range of 40 km and height of 30 000 ft.

Elevation (deg)	Max Range (km)	PRT (µs)
1 to 2	40.0	321
3 to 5	40.1	322
6 to 7	40.2	323
8 to 9	40.4	324
10 to 13	40.9	327
14 to 17	37.8	306
18 to 20	29.6	252
21 to 30	19.5 to 26.4	185 to 231

extent to the minimum between the down range and height requirements. The true range to the down range (r_d) and height (r_h) can be calculated via

$$r_d = \frac{r_0}{\cos\phi} \tag{5.6.1a}$$

$$r_h = \frac{h_0}{\sin\phi} \tag{5.6.1b}$$

Where r_0 and h_0 are the volume scan range and height extents, respectively (40 km and 30 000 ft in this case), and ϕ is the true elevation. The minimum PRT at a particular elevation is found from the minimum value between r_d and r_h, plus a padding term

$$\mathrm{PRT}_\phi = \min\left[r_d, r_h\right] + \left\lfloor \frac{2\tau}{c} \right\rfloor . \tag{5.6.2}$$

Additional padding is required at the end of the instrumented range in (5.6.2) to account for pulse compression. To ensure that the pulse compression gain is maintained throughout the entire receive window, additional samples must be collected and processed to mitigate *edge effects* during pulse compression. The padding term in (5.6.2)

adds enough samples as would be covered by the blind range of the waveform (or the length of the matched filter waveform, whichever is greatest).

From these results and assuming a dwell time of 74.7 ms per radial, it will take 190.3 s to complete each volume scan. If the standard deviation requirements for Z_{dr}, ρ_{hv}, Φ_{DP} are relaxed at elevations above 20° and a 64-pulse CPI is used, the volume scan time is reduced to 129 s. While this scan time is sufficient for a radar performing weather surveillance only, it would detrimentally affects the radar ability to perform other missions concurrently, such as airport or air route surveillance. The implications of this result are discussed in the next section.

5.7 Summary and Conclusions

Several conclusions can be reached from analysis of both the simulation and radar data. Results show that the standard deviation achieved with X-band phased arrays agrees with theoretical approximations. This is a simple, but powerful result: X-band phased arrays do not contribute additional variability to the pulse-pair estimates. Theoretical approximations, when computed with actual SNR, spectral width, and correlation coefficient, are in good agreement to the estimates of standard deviation of the products from the live data. Results do show an increase in variability, or *spread*, of standard deviations when compared to theoretical values, which is attributed to errors in the motion compensation procedure and natural variability of weather.

Additionally, simulations show that X-band radars using ATAR require a dwell time of at least 21.4 ms (64 total pulses per radial at a 3 kHz PRF) and 74.7 ms (224 total pulses per radial) for single- and dual-polarization modes, respectively, to meet the MPAR notional requirements in Table 5.1. When extrapolated to a hypothetical phased array radar covering a down range of 40 km and height of 30 000 ft, the total volume scan time is 129.7 s.

Table 5.4: Summary of data quality requirements and minimum dwell times, derived from simulation results and radar data. Here, data quality refers to the standard deviation of the product estimates. It should be noted that when considering differential phase in the context of translating the notional requirements X-band, since the wavelength (λ) at X-band (3.2 cm) is approximately three times shorter than at S-band (10 cm). Because of this, the requirements for differential phase can be relaxed, as indicated by the requirements in parentheses.

Product	σ^0_{max}	σ^1_{max}	σ^2_{max}
Reflectivity (Z_h)		1.8 dBZ	
Radial Velocity (v)		$1\,\mathrm{m\,s^{-1}}$	
Spectral Width (σ_v)		$1\,\mathrm{m\,s^{-1}}$	
Differential Reflectivity (Z_{dr}, $\phi < 20°$)		0.3 dB	
Copolar Corr. Coefficient (ρ_{hv}, $\phi < 20°$)	6.0E−3	8.4E−3	12.9E−3
Differential Phase (Φ_{DP}, $\phi < 20°$)	2.5° (7.5°)	3.0° (9.0°)	4.3° (12.9°)
Signal to Noise Ratio (SNR)		2 dB	
M_l ($\phi < 20°$)	224	128	64
M_u ($\phi > 20°$)	64	64	64
Volume Scan Time (s)	129.7	78.7	44.7

Based on these results, it is therefore not practical for X-band phased array radars that support multiple missions to meet these requirements. To that end, Table 5.4 proposes a set of reduced requirements for the standard deviation of the polarimetric products. As bias is heavily dependent on system calibration and characterization, the proposed requirements focus exclusively on standard deviation. The table shows three sets of requirements that correspond to the original requirements in Table 5.4 (σ^0_{max}), a 20 % reduction (σ^1_{max}), and a 40 % reduction (σ^2_{max}). The proposed requirements in σ^1_{max} (σ^2_{max}) degrade the most stringent requirements by 20 % (40 %) and reduce the volume scan time to 78.7 s (44.7 s). How well X-band phased array radars perform Quantitative Precipitation Estimation (QPE) and Quantitative Precipitation Forecasting (QPF) with these degraded requirements is beyond the scope of this

research, but these results provide valuable insight into the degree of performance expected under different scan scenarios.

Another important consideration can also be drawn from these results. If the measured spectral width exceeds $4\,\mathrm{m\,s^{-1}}$ to $6\,\mathrm{m\,s^{-1}}$, estimates of copolar correlation coefficient and differential phase will be biased and exhibit increased variance. Since differential phase unfolding algorithms [116] typically search for *valid* areas of differential phase from limits on ρ_{hv} and Φ_{DP}, analysis of the measured spectral width should be included in these algorithms as well. In the LPAR system, for example, valid Φ_{DP} is typically declared if the standard deviation of differential phase is less than 10° and copolar correlation coefficient is greater than 0.8. However, if the spectral width is greater than $4\,\mathrm{m\,s^{-1}}$, the limit on ρ_{hv} is reduced to 0.5. The same strategy should be used whenever ρ_{hv} is used as a threshold parameter for an algorithm.

CHAPTER 6

ADAPTIVE RADAR WAVEFORM CONTROL

Most current operational weather radars use a static set of waveform and scan parameters to observe the environment. Top-level requirements such as data quality, sensitivity, and volume revisit rates flow down to lower-level component requirements on the hardware and software. Scan acquisition parameters, transmit waveforms, and signal processing algorithms are judiciously chosen to meet these top-level requirements. As many of the current operational systems use passive magnetron or klystron-based transmitters with mechanically-rotating antennae, this flow of operations is required because of the hardware's inability to vary beam pointing angle or waveform on short time scales. With the development of affordable phased array radars however, modern meteorological radars can now support a more flexible and adaptive concept of operations. This chapter presents the development of an algorithm for the adaptive control of the radar dwell time to meet data quality requirements on the standard deviation of weather products. The algorithm uses a system of adaptive weights to control how the radar dwell time is varied in response to real-time measurements of the signal variance of one or more products. Simulation results and radar data are presented That demonstrate the ability of the algorithm to adaptively control the integration time to meet a set of notional data quality requirements.

6.1 Introduction

The notion of adaptively changing a radar mission in response to the environment has already been investigated for use in defense applications. Techniques have been

developed and tested for adaptive radar resource management [32, 11], adaptive waveform selection [109], and adaptive target detection and tracking [24]. More recently, the field has expanded to include the new concept of cognitive radar. Haykin [53] first distinguished cognitive from adaptive radars as having three qualities:

- The radar continuously senses the environment and passes this information to the receiver
- The transmitter intelligently changes its illumination of the environment, making adjustments to the transmitted signal in an effective and robust manner
- The radar is a closed loop system between the transmitter, environment, and receiver

In radar meteorology, initial work has already begun to make weather radars more cognitive and adaptive to the environment. The next-generation Multifunction Phased Array Radar (MPAR) being developed at the National Weather Radar Testbed (NWRT) has proposed an adaptive scanning strategy to optimize the update rates on weather targets. The strategy, called Adaptive DSP Algorithm for Phased-Array Radar Timely Scans (ADAPTS) adaptively adjusts target revisit times and minimizes scanning inactive sectors to optimize radar allocation of resources and data quality [112]. The strategy uses a time balance radar scheduler, which prioritizes radar modes according to the time they take to execute. The ADAPTS algorithm also adjusts the dwell times differently for surveillance of inactive areas (short dwell times) or detection and tracking of active weather areas (long dwell times). Additionally, Curtis [33] proposed that adaptive scanning in phased array weather radars also could also include the tailoring of dwell times at each beam position.

In addition, Zink et al. [121] developed an adaptive scanning strategy for networked radars, known as Distributed Collaborative Adaptive Sensing (DCAS). Based on the principles of Multi-Attribute Utility Theory (MAUT), the system senses the

active areas and adaptively schedules where each radar is tasked. Radar resources are optimized for scan quality (update rate) and end-user priority. While not adaptive, Bharadwaj and Chandrasekar [10] proposed a frequency-diverse waveform selection scheme to mitigate the discontinuities in sensitivity at blind range boundaries between waveforms. Waveforms with increasing pulsewidths at different frequencies are used, and radar returns from each waveform are mapped to different range extents.

The aforementioned techniques are a critical first step at making meteorological radars more intelligent and adaptive to the environment. However, there are many more opportunities for improvement. Little research has been done to make these systems more waveform-agile beyond the selection of distinct radar modes for clear air and convective weather or for surveillance and tracking. Performance monitoring has been used to govern beam placement and update rates, as described previously, but the technique has not been extended to measure and control the quality of detected weather signals using waveform agility.

To illustrate the benefit of improved waveform agility, consider the following example. Suppose a radar is required to support a standard deviation of Reflectivity no greater than 1.8 dBZ at an Signal to Noise Ratio (SNR) of 10 dB and spectral width of $4\,\mathrm{m\,s^{-1}}$. Using the theoretical analysis from the previous section, at least 32 samples are required for an X-band phased array radar operating at a 3 kHz Pulse Repetition Frequency (PRF). Without adaptive control, any weather tracking mode of operation would operate with at least 32 pulses to meet the top-level requirement. However, what if the actual measured spectral width is only $2\,\mathrm{m\,s^{-1}}$? The integration time could be theoretically reduced while maintaining the same signal variance. Furthermore, if the standard deviation and spectral width were continuously monitored, the integration time could be adaptively adjusted on-the-fly. In this manner, the dwell time on the weather target would be minimized, while still meeting the data quality requirement.

This chapter is organized as follows. Section 6.2 presents background information and a motivation for the use of adaptive control in weather radar processing. In Section 6.3, an Adaptive Waveform Control (AWC) algorithm is proposed to monitor a volume and adaptively manipulate the Coherent Processing Interval (CPI) within designated areas to meet top-level data quality requirements. The AWC algorithm is broken into distinct steps for (1) situation assessment and (2) performance evaluation. Section 6.4 presents simulation results of the algorithm applied to two different scenarios. In each scenario, the algorithm was setup to meet a different set of data quality requirements. Radar data is presented in Section 6.5 from a precipitation event in April 2015, where the algorithm was tasked with meeting a desired standard deviation of reflectivity ($SD(Z_h)$). Section 6.6 provides a summary and concluding remarks.

6.2 Background

The theoretical formulas for estimating the variances of the polarimetric weather products are well understood, and the sources of variability can be broken down into both statistical errors from the measurement and additive errors introduced by the system. Under ideal system performance, the variances of the products are dependent on the radar wavelength (λ), received SNR, spectral width (σ_v), and copolar correlation coefficient (ρ_{hv}) [37]. Approximations for these variances under high SNR and other conditions are presented by Doviak and Zrnić [37], while exact solutions for arbitrary SNR are available for either the Simultaneous Transmit/Simultaneous Receive (STSR) [76] or Alternate Transmit/Alternate Receive (ATAR) polarization pulsing schemes [77]. In general, for convective weather, measurement errors can be reduced by increasing the integration time, or CPI, on a region of interest. For pedestal-mounted dish antennae, this corresponds to decreasing the rotation rate. Phased array radars, on the other hand, utilize electronic-steering in azimuth and

elevation, so the integration time can be set directly for each radial by specifying the PRF and number of incoherently integrated pulses.

With this in mind, logic would suggest then that the phased array integration time could simply be statically set according to the measured products. That is, the integration time for each radial on the next scan could be calculated directly from the measured SNR, spectral width, and correlation coefficient so as to achieve a desired variance on the next scan. In practice, however, the problem is not so straightforward. Non-ideal system performance and atmospheric artifacts can cause the measured variance to deviate from theory. Melnikov and Zrnić [76] presented experimental results that show the ATAR polarization mode will cause additional variability at large spectral widths, which were not accurately modeled by empirical approximations. Since the polarization is switched after every pulse in ATAR, the effective PRF per polarization is halved. As the spectral width approaches the Nyquist velocity, the Doppler spectrum flattens and the pulse-pair estimates become inaccurate. With phased arrays, mismatch in gain and phase between the polarizations also contributes to both the bias and variance of product estimates [45]. Similarly, mismatch between the beam patterns or pointing angles in each polarization can also contribute errors. While these error sources may not be significant, they warrant a more sophisticated algorithm for adaptive control of the integration time.

One of the major challenges that next-generation phased arrays face are stringent requirements for support of simultaneous missions for air traffic control and atmospheric surveillance [41, 110]. Recent studies have indicated, however, that traditional scanning strategies will not be able to support both missions and that more advanced phased array geometries or scanning techniques are required. Zrnic et al. [123] proposed using time and beam multiplexing to task the radar to look in different directions simultaneously. Galati and Pavan [44] performed a trade study with different

overlapping beams and proposed using Digital Beam Forming (DBF) with fan/pencil beams on transmit/receive to meet air traffic control and weather requirements.

As opposed to novel phased array architectures or advanced beamforming, this AWC algorithm focuses on optimizing scan time by an efficient concept of operations. In traditional radar system design, top-level requirements on data quality are used to set the integration time, beam positioning, and revisit rates on the radar. In contrast, this algorithm sets adaptively sets the integration time to achieve a desired level of data quality. The details of the algorithm are presented herein.

6.3 Algorithm Description

The AWC algorithm takes advantage of the flexible scanning offered by phased arrays and adaptively controls the dwell time on an area of interest in response to measured performance. The purpose of the algorithm is to find the *minimum* dwell time required to meet a set of user data quality specifications. Note that this technique will find the *minimum*, not optimal, dwell time required. The concept of operations for the algorithm, and how it relates to minimality versus optimality, best be illustrated with an example.

Suppose one desires to estimate the polarimetric products with the standard deviations given in Table 5.1. From the analysis in Section 5.7, at least 224 pulses are required in each CPI[1]. So, if the spectral width and SNR of the weather echoes are approximately $2\,\mathrm{m\,s^{-1}}$ and 20 dB, respectively (per the conditions in Table 5.1), the algorithm will adaptively change the CPI on the area and settle at 224 pulses. If the measured spectral width reduces to $1\,\mathrm{m\,s^{-1}}$, less pulses would be required to meet the standard deviation requirements (as evidenced from the trends in Figure 5.3). The

[1]This CPI length assumes a 74.7 ms dwell time at X-band with a 3 kHz, in accordance with the simulation parameters in Section 5.7.

algorithm then would respond to the changes in spectral width and reduce the CPI accordingly.

This introduces a problem, however. Suppose that a system is specified to meet requirements for standard deviation of multiple products, such as reflectivity and differential phase. From Figure 5.4, it is apparent that the requirement for differential phase would require a longer CPI. What then is the *optimum* dwell time in this scenario? This algorithm finds the minimum dwell time that would meet both requirements, and it would thus set the dwell time to meet the differential phase requirement. By extension, the reflectivity requirement would also be met.

The AWC algorithm is designed to be completely autonomous so that the only interaction the radar operator has with the system are initial specifications on the standard deviation in the weather products. Internally, the algorithm accounts for non-ideal variability in the data by relying on a system of adaptive weights to control the integration time on future scans. The details of the algorithm are described below.

6.3.1 Situation Assessment

The concept of operations for the AWC algorithm begins with situation assessment. At the onset of operations, the radar is setup to execute a volume scan with a short, 16 − to 32 −pulse CPI. For an X-band phased array looking out to an unambiguous range of 40 km, the volume scan takes between 10 s to 20 s to execute. This volume scan is similar to that used on the X-band phased array as described by Hopf et al. [57]. This is used as the weather surveillance scan to probe for new, active areas containing weather.

Data from the surveillance scan at each azimuth location is then passed to the tracker. The role of the tracker is to analyze the measured data from each azimuth radial and identify areas of active weather. This is done through the use of a weather map, which groups the azimuth radials in over-lapping, 3° azimuth bins throughout

the scan sector. Within each azimuth bin, a performance evaluation technique is used to adaptively control the CPI within that area. Torres and Curtis [112] proposed a similar technique of weather mapping a desired volume, known as the ADAPTS strategy, which maintains a list of the active weather areas in the volume and decreases the integration time on inactive areas. This algorithm uses a similar technique, except that the CPI in the active areas is adaptively managed. The details of how the CPI is adaptively controlled are described in the next section.

6.3.2 Performance Evaluation

This algorithm uses three different performance metrics, or *figures of merit*, to control how the CPI should be modified in real-time on a region of interest. The technique described herein is concurrently applied to each azimuth bin. Nominally, each bin encompasses (typ.) three radials of data within a single 3° sector.

The AWC algorithm uses an adaptive weighting scheme to determine how the integration time will evolve. After each surveillance scan, the number of incoherently integrated pulses (M) on the next scan action within the current azimuth bin is updated from the product of a weighting factor and the default pulse block size (δ_M). The pulse block size (typ. 32) limits the amount by which the CPI can vary from one scan to the next. In addition, the absolute minimum and maximum total number of integrated pulses are bounded to (typ.) 16 and 256 pulses, respectively. The number of pulses per radial on the $(n+1)$th scan ($M[n+1]$) is updated from from the number of pulses on the nth scan ($M[n]$) multiplied by a weighting factor

$$M[n+1] = M[n] + w[n]\delta_M. \tag{6.3.1}$$

The weighting factor (w) is computed from the aggregate summation of weights derived from the measured SNR (w_{SNR}) and performance metric for the pth weather product (w_p). Nominally, this performance metric is derived from the standard devi-

ation of the product, but this technique is generalized to any metric of interest. The weighting factor used in (6.3.1) is computed as

$$w = \frac{\sum_{p=0}^{N_P} a_p \overline{w}_s^p}{\sum_{p=0}^{N_P} a_p} \tag{6.3.2}$$

Where N_P is the total number of products analyzed and a_p is a user weighting factor which ranks the importance of the pth product ($a_p > 0$). Typically, a_p is set to unity for each product, which reduces the summation in (6.3.2) to an arithmetic mean. The weighting factor for each weather product ($\overline{w}_s^p$) is computed from the performance metric averaged over all range bins in the azimuth bin, multiplied by a SNR-dependent weight

$$\overline{w}_s^p = \frac{\sum_g w_{\mathrm{SNR}}[g]\, w_c[g]\, w_s^p[g]}{\sum_g w_{\mathrm{SNR}}[g]}. \tag{6.3.3}$$

This weighting ($\overline{w}_s^p$) is a factor that quantifies how close the measured performance metric at each gate is to the desired metric for that product within the storm cell, and w_c is a control weighting factor. The SNR-dependent weighting (w_{SNR}) is used as a quality control to prevent the algorithm from over-compensating for poor quality at low SNR. The purpose of the quality control threshold is to apply less weight ($w_{\mathrm{SNR}} \rightarrow 0$) if the measured SNR is below a desired threshold and more weight ($w_{\mathrm{SNR}} \rightarrow 1$) if the SNR is higher. This is accomplished through the use of the continuous-log sigmoid function. The equation of the sigmoid function for an input value x is given by

$$f(x, a, c) = \frac{1}{1 + \exp[-a(x - c)]}. \tag{6.3.4}$$

The sigmoid function ranges from ± 1 at $\pm\infty$ and 0.5 when $x = c$. The factor a determines the slope of the function about c. The weight at each range bin is computed from the measured SNR ($\hat{\text{SNR}}$) and a threshold parameter (SNR_0) as

$$w_{\text{SNR}} = f\left(\text{SNR}, 1, \text{THR}\right). \tag{6.3.5}$$

Here, THR defines the minimum desired Signal to Noise Ratio for valid samples in the azimuth sector. To estimate the performance metric weighting factor at each gate ($w_s^p\left[g\right]$), the algorithm computes the moving statistics of the metric across each gate in the azimuth bin within a 60 s sliding time window. In the case of the metric as the standard deviation of the products, a moving standard deviation is performed. Otherwise, it is a moving average. The challenge in this measurement technique is correctly compensating for the motion of the storm within each sliding time window. This motion compensation step performs the technique described in in Section 5.3 to correct for radial motion. This algorithm currently does not account for tangential motion of the storm.

After motion compensation, the average performance metric is computed along each gate in the sliding window. The metric weighting factor at each ($w_s^p\left[g\right]$) is computed from the sigmoid function in (6.3.4)

$$w_s^p\left[g\right] = 2f\left(\hat{x}^p\left[g\right] - x_0^p, \alpha, 0\right) - 1 \tag{6.3.6}$$

Where $\hat{x}^p$ is the measured performance metric, x_0^p is the desired metric, and α is a factor that controls the steepness of the sigmoid function (typ. $\alpha = 4$). The weighting in (6.3.6) is such that range bins with a performance metric below (above) the desired level are given positive (negative) weight, and bins with values close to the desired level (x_0^p) are given zero weight. In a similar fashion, w_c from (6.3.3) is a control factor

that thresholds $\overline{w}_s^p$ if the metric requirement has been met. The control weighting is also calculated from a sigmoid function

$$w_c\left[g\right] = f\left(\frac{\hat{x}^p\left[g\right] - x_0^p}{x_0^p}, \beta, 0\right). \tag{6.3.7}$$

Here, β controls the steepness of the control weighting about $\hat{x}^p = x_0^p$ (typ. $\beta = 4$).

The rationale for this weighting scheme is straightforward. Assume that the performance metric being measured is the standard deviation, and that one requires a standard deviation of reflectivity of 1.8 dBZ. If the actual measured deviation is 4 dBZ, then the weighting from (6.3.6) will be positive and the number of pulses requested on the next scan from (6.3.1) will be increased. This in turn will decrease the standard deviation in subsequent time windows. On the other hand, if the measured standard deviation is 0.5 dBZ, then the weighting will be negative and the algorithm will reduce the integration time. Thus, the dwell time (and total scan time) is reduced while maintaining a desired standard deviation. If, however, the measured SNR is too low for a standard deviation of 4 dBZ, the quality control weighting in (6.3.5) will de-value the weight applied to (6.3.1), and the integration time will not be affected by those gates. Thus, the algorithm only reacts to the measured data quality if the SNR is above a pre-determined threshold.

There are several error sources and deficiencies recognized in this algorithm that will degrade performance. First, tangential motion of the storm is not accounted for. Practically, accurately estimating the two-dimensional velocity vector from a single radar within a finite time window is a difficult task. While techniques such as Storm Cell Identification and Tracking (SCIT) have been been implemented on operational radars for tracking the storm motion between long volume scans (5 min to 6 min), they have not been effectively demonstrated at short intervals. Additionally, the algorithm is subject to over-constraint. That is, under certain conditions it may be impossi-

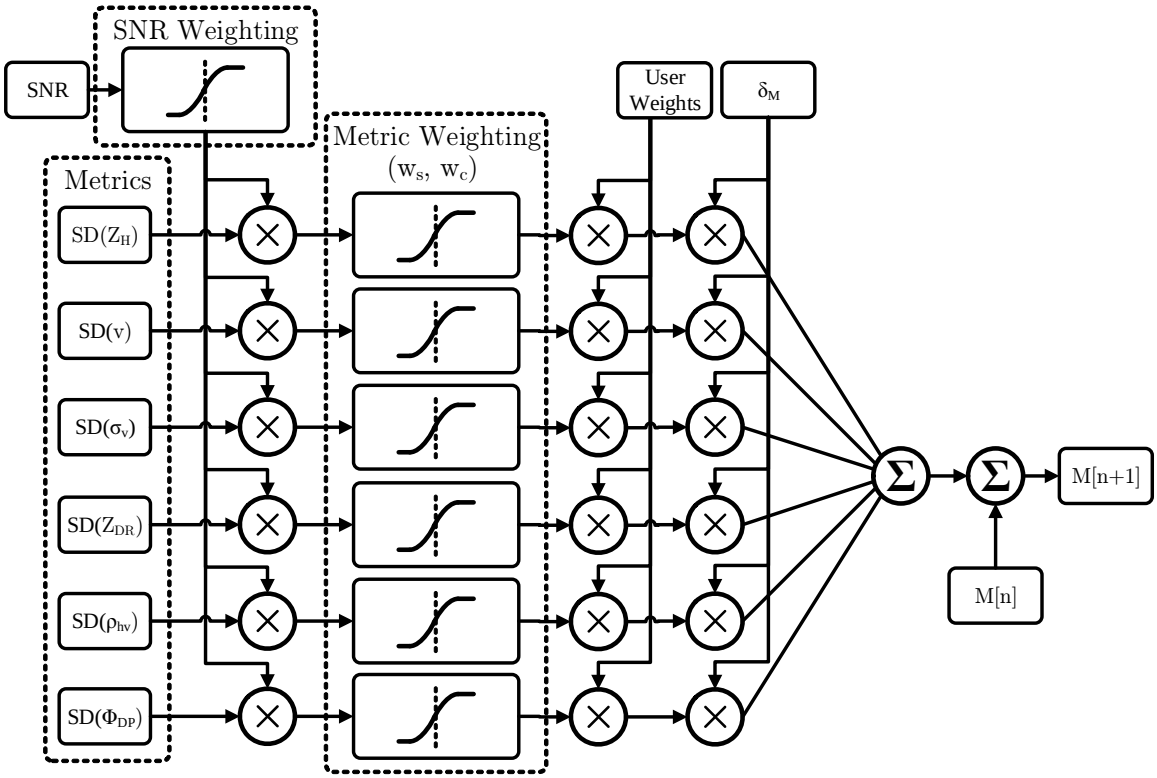

Figure 6.1: Block diagram of the performance evaluation stage of the AWC algorithm, assuming the performance metric as the standard deviation of the products. Computation of the standard deviation weighting (w_σ) and control weighting (w_c) is performed within the *Metric Weighting* block. This stage accepts as input the estimates of the standard deviation on the products, and outputs the change in CPI length for the next scan action on the track.

ble to simultaneously meet multiple requirements. Requirements and conditions on minimum SNR should be considered beforehand, so that the it's

6.4 Simulation

The following Monte Carlo simulation was performed to test the adaptive CPI technique described previously. On each trial, radar In-phase and Quadrature (IQ) data was generated for a hypothetical storm cell encompassing a sector of 5 radials and 100 range bins. To simulate the storm progression in each trial, 100 observations spaced 6 s apart were simulated and fed to the adaptive CPI algorithm. The range bin locations of the IQ data on the simulated storm cell were shifted to account for a radial velocity of $3\,\mathrm{m\,s^{-1}}$. The algorithm was setup to find the minimum CPI to meet a set

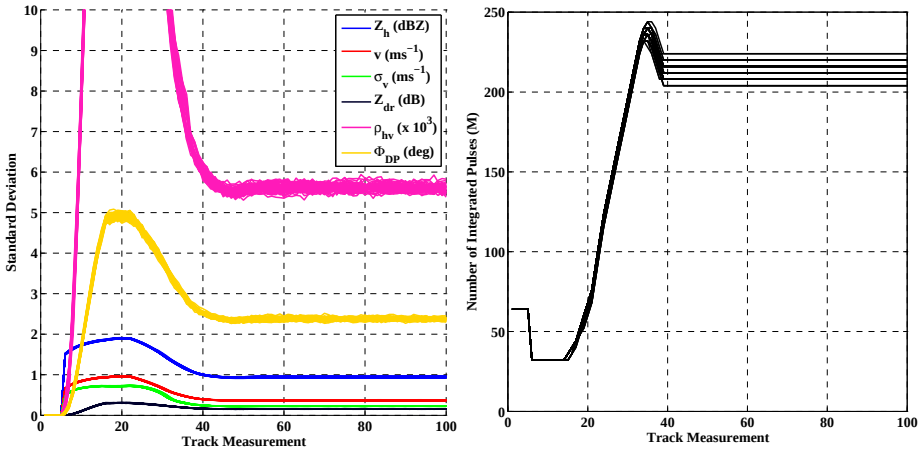

(a) (b)

Figure 6.2: Simulated results of the AWC algorithm, showing the evolution of the (a) estimated product standard deviations and (b) commanded CPIs for each track measurement. The algorithm was setup to meet the standard deviation requirements from Table 5.4 (σ^0_{max}), of which the most stringent requirements are those on ρ_{hv} (6E−3) and Φ_{DP} (2.5°). The simulation assumed operation at a 3 kHz PRF and the polarimetric ATAR scheme. Results confirm a resting 212-pulse CPI after 42 track observations.

of requirements on the standard deviation of the product estimates. On each trial, the algorithm was initialized with a 32-pulse CPI. IQ data was generated in each range bin using the Gaussian shaping filter approach described in Section 3.6, with a minimum 20 dB SNR, a copolar correlation coefficient above 0.99, and a 2 m s^{-1} spectral width. Two different simulations were executed, with a minimum of 100 trials each. Following each Monte Carlo simulation, the following results were analyzed. The *settling time* and *resting* CPI for each trial run was measured as the time taken for the CPI to settle on to 10 % of its final value. In addition, the final resting standard deviations of each product estimate were computed.

The algorithm was setup to find the minimum CPI in order to meet the σ^0_{max} and σ^1_{max} requirements listed in Table 5.4. The difference between these requirements sets are a relaxing of the standard deviation for ρ_{hv} and Φ_{DP}. From the previous research, it is expected that the final CPI from each simulation should be close to 224 and 128 pulses, respectively

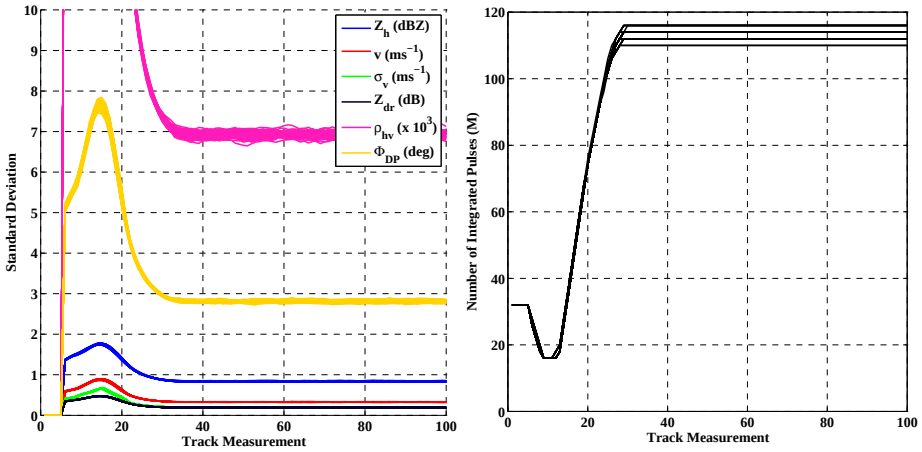

(a) (b)

Figure 6.3: Simulated results of the adaptive CPI control algorithm, showing the evolution of the (a) estimated product standard deviations and (b) commanded CPIs for each track measurement. The algorithm was setup to meet the standard deviation requirements from Table 5.4 (σ^1_{max}), of which the most stringent requirements are those on ρ_{hv} (6E−3) and Φ_{DP} (2.5°). The simulation assumed operation at a 3 kHz PRF and the polarimetric ATAR scheme. Results confirm a resting 112-pulse CPI after 42 track observations.

Figure 6.2 shows the results of the first scenario to meet the σ^0_{max} requirements. From analysis of the data, the CPI was commanded from 32 pulses initially to an average final dwell length of 212 pulses in under 39 observations. This data aligns well with the previous analysis in Table 5.4, which indicated that 224 pulses would be required. Figure 6.3 shows similar results from the second scenario to meet the σ^1_{max} requirements. Results also agree well with the previous analysis, with the algorithm arriving at a 112-pulse CPI after 40 observations.

Inspection of Figures 6.2a and 6.3a indicates that the algorithm does exhibit some overshoot before settling to final estimation of the standard deviations from each product. This overshoot is due to the sliding window during which the standard deviation is actually measured. For a 6 s track interval between measurements, it takes 10 observations for the algorithm to estimate the standard deviation accurately. So, we can expect an overshoot on the order of twice the sliding window length, since it takes another 10 observations for the algorithm to respond to the change.

Table 6.1: Summary of simulation results from the AWC algorithm applied to different notional data quality requirements from Table 5.4. Results indicate that the algorithm is effective at measuring the standard deviation and adaptive controlling the CPI to meet the requirements. For requirement sets σ^0_{max} and σ^1_{max} Table 5.4, the algorithm adaptively controlled the CPI to 212 pulses and 114 pulses, respectively, which closely match expected results. Fields marked with a dash (—) indicate that data is not applicable or the simulation results do not apply.

Product	σ^0_{max}		σ^1_{max}	
	Req.	Meas.	Req.	Meas.
Z_h (dBZ)	1.8	0.94	1.8	0.90
v ($\mathrm{m\,s^{-1}}$)	1	0.36	1	0.32
σ_v ($\mathrm{m\,s^{-1}}$)	1	0.23	1	0.18
Z_{dr} (dB)	0.3	0.16	0.3	0.18
ρ_{hv}	6E−3	5.6E−3	8.4E−3	6.9E−3
Φ_{DP} (deg)	2.5	2.3	3.0	2.8°
No. Integrated Pulses (M)	224	212	128	114
No. Observations	—	40	—	40

Table 6.1 shows a summary of the simulation results for each scenario tested against. Results show that the algorithm was successful at adaptively controlling the CPI to meet the set of desired product standard deviations. As evidenced in the results, the minimum CPI is dominated by the most stringent requirements, copolar correlation coefficient and differential phase. As such, while the algorithm is successful at meeting each requirement for each product, it over-estimates the standard deviations of the less stringent requirements.

6.5 Radar Data

To test the algorithm against live radar data, the following experiment was performed. Timeseries data was collected during a precipitation event within a 10 min time interval on 7-April-2015. During this period, a storm cell having a mean reflectivity above 25 dBZ was observed moving across the radar field-of-view. The storm

cell encompassed close to a 30° azimuth sector in front of the array, initially centered on boresight of the array. During this period, the radar was setup to execute a single 90° sector scan, with a 256-pulse CPI at a 3 kHz PRF. The radar operated with a 55 µs, 2 MHz Linear Frequency Modulated (LFM) chirp waveform with a Blackman window applied.

To analyze how the algorithm performed against the 256-pulse CPI, a measure of detectability was used to estimate the degradation in detection performance in using the algorithm. Ivic et al. [61] used ratios of detections between different scan algorithms to measure the performance benefit of different data thresholding algorithms. Similar to their method, an estimate of the probability of detection between the measured SNR fields from two scans (SNR_A and SNR_B) is computed as

$$\hat{P}_d = \frac{\mathrm{num}\left[(\mathrm{SNR}_A > \mathrm{THR}) \,.*\, (\mathrm{SNR}_B > \mathrm{THR})\right]}{\mathrm{num}\left[(\mathrm{SNR}_B > \mathrm{THR})\right]} \tag{6.5.1}$$

Where THR is the SNR threshold level (in dB). Here, SNR_A and SNR_B correspond to data from the AWC algorithm output and the 256-pulse CPI, respectively. In this fashion, the terms in brackets represent binary matrices, where a value of 1 indicates that a detection is present, and a value of 0 indicates no target. The *num* operator calculates the total number of ones present in the input matrix, and the .* operator is an element-wise multiplication operation. Equation (6.5.1) is the ratio of the number of detections that are produced when data is processed by the AWC algorithm that were not present in the traditional Contiguous Pair Sampling (CPS) data. This gives a measure of the decrease in the probability of detection from the algorithm.

Recorded timeseries data during the event was then fed to the algorithm for post-processing. As described previously, the algorithm was setup to adaptively monitor the performance in 5° azimuth bins throughout the 90° sector. Within each azimuth bin, the technique described in Section 6.3.2 was used to monitor the standard deviation of reflectivity and adaptively control the CPI within that sector. The CPI output

at each azimuth was then used to limit the pulse-pair processing on subsequent scans. During this experiment, the algorithm was setup to achieve a standard deviation of reflectivity of 1.2 dBZ ($SD(Z_h) \leq 1.2$). To simplify the analysis, no other products were monitored by the algorithm.

Figure 6.4 shows plots of the evolution of the (a) CPI and (b) measured standard deviation of reflectivity at each azimuth radial. Moving upwards along the y-axis shows the change over each observation in the time interval (≈ 75 radar scans). White areas in the plots show the lower limits in each figure. By comparison, Figure 6.5 plots the measured reflectivity (Z_h) on the (a) first scan and the (b) 50th scan. Note how the peak reflectivity moves across the array from boresight initially towards an azimuth angle of 30°, as shown in the accompanying plots in Figure 6.5.

Several observations are evident from these plots. Beyond the initial scans as estimates are fed through the 60 s moving average windows, the algorithm settles to a mean $SD(Z_h)$ of 1.1 dBZ across all azimuth radials past the 35th scan, which confirms that the algorithm was able to meet the specified requirement. Additionally, past the 45th scan, as the region of peak reflectivity moves towards the right side of the plot, the algorithm decreases the CPI within azimuth angles near $-30°$ to 0°. During this period, the measured SNR was below the threshold set for the algorithm (8 dB), which caused the algorithm to reduce the CPI. Similarly, we observe that the algorithm never increased the CPI at azimuths $-30°$ to $-20°$. Again, the SNR never exceeded threshold at this sector, so the algorithm did not increase the dwell time.

The probability field in Figure 6.4c shows that the algorithm maintained a minimum 85 % probability of detection against the 256-pulse CPI data. That is, use of the algorithm only degraded our sensitivity by 15 % at most. Inspection of the data shows that the probability of detection near the region of peak reflectivity was maintained above 95 % during the time interval observed.

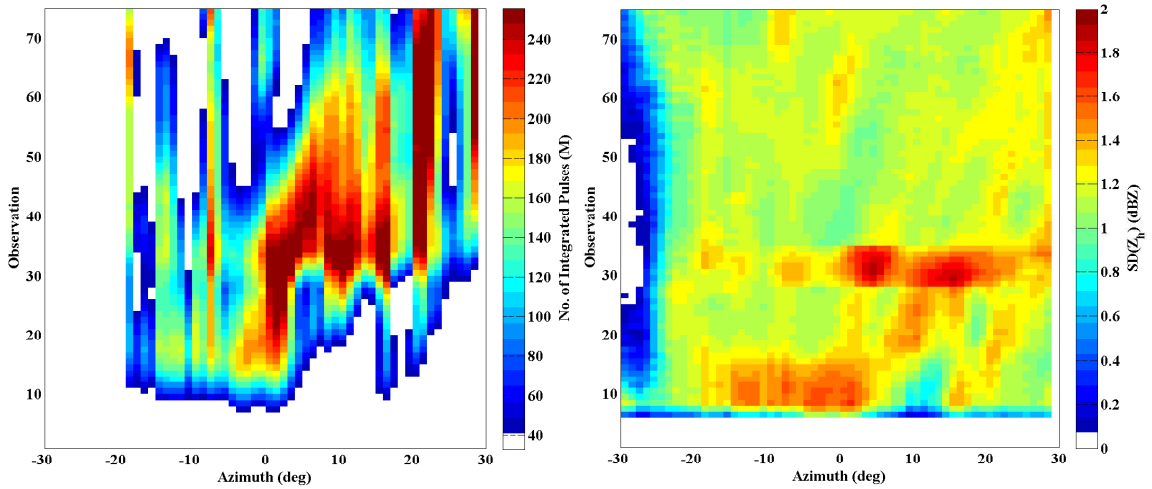

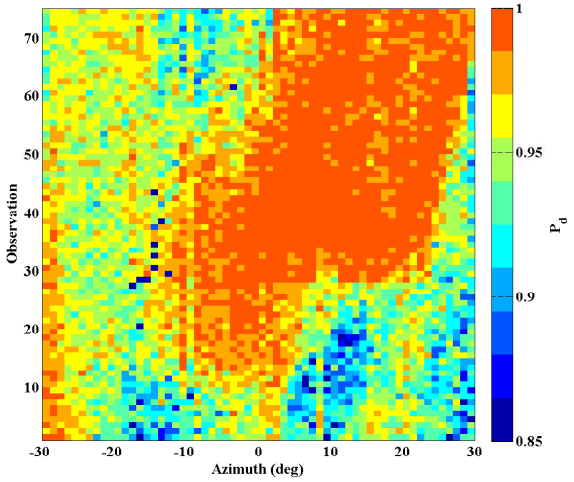

Figure 6.4: Results of the AWC algorithm applied to a 10 min period during a precipitation event on 7-April-2015. From top left show the evolution of the (a) CPI, (b) measured standard deviation of reflectivity, and (c) estimated probability of detection. The x-axis shows the azimuth radial, and the y-axis shows the scan observation count. Here, the algorithm was set to meet a standard deviation of reflectivity of 1.2 dBZ ($SD(Z_h) \leq 1.2$), which the algorithm was effective at maintaining over all azimuth radials beyond the 35th scan. The probability of detection in (c) is computed from (6.5.1) by counting the number of detections common to both the AWC algorithm and a traditional CPS scan strategy with 256 pulses.

The total amount of dwell time commanded by the algorithm over the time interval, over all radials in the sector, was just 133.8 s, compared to 390 s for the 256-pulse CPI. This represents a 290 % reduction in the scan time.

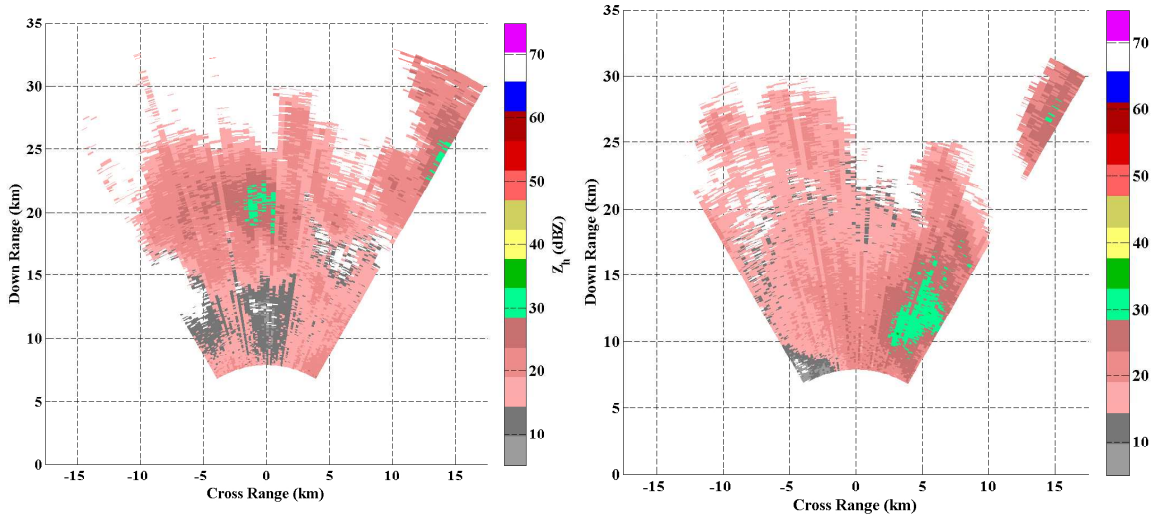

Figure 6.5: Plots of the measured reflectivity field ($\hat{Z}_h$) from two observations at timestamps (a) 20:20 UTC and (b) 20:27 UTC. In accordance with the AWC algorithm results shown in Figure 6.4, a region of peak reflectivity in the storm cell migrated from boresight to an azimuth angle of 30° ([5, 12]km [cross range, down range]).

6.6 Summary and Conclusion

This research proposed a technique for the adaptive control of the radar integration time within a volume scan in response to specified performance requirements. Building upon a previous technique [112], the algorithm maintains a map in the volume of the areas containing active weather. Within active weather areas, the algorithm uses a systems of weights derived from sigmoid activation functions to find the minimum CPI required such that each requirement is met. In the context of the radar mission, the algorithm can be used to meet a desired data quality requirement, such as bias or standard deviation of the product estimates.

Radar data was presented that tested the algorithms performance in meeting a desired standard deviation of reflectivity. Results indicate that the algorithm takes from 30 to 35 observations of an area to settle, but thereafter the standard deviation requirement was met in the volume. In addition to meeting the specified requirement,

the algorithm only degraded the sensitivity (taken as the decrease in detectability) by 15 %.

While this algorithm has been demonstrated to be effective at controlling the standard deviation of a product, it may be more advantageous to monitor the detection performance or some other metric. However, the details of the algorithm were proposed as generic, such that alternate applications to monitoring other metrics is supported.

CHAPTER 7

CONCLUSION

X-band phased array radars are rooted in military and defense applications. To-date, they have exclusively been used primarily for target surveillance and tracking, with weather as an ancillary mode performed intermittently at best. As the cost of this technology decreases, however, more commercial and civil entities will find uses for phased array systems. But, in the context of a radar supporting multiple, simultaneous missions, it is important both to discover novel applications for phased arrays while verifying their performance for traditional purposes. To that end, this research has both investigated the data quality of phased array radars for weather surveillance and two novel algorithms.

For over four months in 2013, the Low-power Phased Array Radar (LPAR) system followed fire personnel and made polarimetric observations in South Australia. Analysis confirms general observations made from previous studies, but the data also shows that smoke plumes present different signatures in areas above the fire. From this analysis, an algorithm is proposed that actively searches for these specific signatures as indication of fire within a smoke plume. Using texture analysis, storm cell tracking, and a fuzzy logic algorithm, results of the algorithm applied to several untrained data sets demonstrate that areas above active fire sources can be reasonably well estimated. Additionally, using approximations of the shape and flow of the smoke plume, the ambient wind direction is estimated with a Root Mean Square (RMS) error from 10° to 25°. While these error bounds may seem large, they are ac-

curate enough to provide emergency personnel with localized estimates of wind shifts in near real-time.

To verify the data quality achievable with X-band phased array radars, research was performed to measure the standard deviation of the polarimetric products against theoretical approximations. Simulation results and radar data confirmed that X-band phased arrays do not contribute additional variability to data. As an extension to this work, research also investigated the performance benefits of more complex scanning strategies, Beam Multiplexing (BMX) and Frequency Multiplexing (FMX). While both methods show an improvement in standard deviation of reflectivity (Z_h) and differential reflectivity (Z_{dr}), bias errors introduced in copolar correlation coefficient (ρ_{hv}) and differential phase (Φ_{DP}) estimates make either BMX or FMX impractical for live operation.

As an extension to the previous research effort, an Adaptive Waveform Control (AWC) algorithm was proposed that monitors the radar volume and adaptively controls the Coherent Processing Interval (CPI) in regions containing active weather to meet top-level data quality requirements. Simulation and radar data were presented that demonstrate the algorithm is effective at both decreasing the integration time on areas where the measured Signal to Noise Ratio (SNR) is below a desired threshold (i.e. *inactive* weather areas) and increasing the integration time when data quality falls below threshold. While the algorithm is far from operational, it demonstrates the capabilities that phased arrays offer in next-generation systems.

This research represents an important first step towards the widespread use of networks of small-scale, X-band phased array radars for either weather or target surveillance applications. While the phase-tilt architecture is a useable, low-cost design and is still applicable in low-altitude surveillance missions, the industry is heading towards an azimuth/elevation electronically-steered phased array radar. Currently,

research efforts are being focused on integrating and testing the Raytheon 2D Low-power Radar (LPR) system [57, 91].

BIBLIOGRAPHY

[1] D. Abraham, "Analysis and design of sliding m-of-n detectors," DTIC Document, Tech. Rep., 2011.

[2] H. Al-Sakka, A.-A. Boumahmoud, B. Fradon, S. J. Frasier, and P. Tabary, "A new fuzzy logic hydrometeor classification scheme applied to the french x-, c-, and s-band polarimetric radars," *Journal of Applied Meteorology and Climatology*, vol. 52, no. 10, pp. 2328–2344, 2013.

[3] Amazon, "Revising the airspace model for the safe integration of small unmanned aircraft systems," in *Proc. of the NASA Unmanned Aerial Systems (UAS) Traffic Management Convention*. NASA, July 2015.

[4] J. M. Ashe, R. L. Nevin, D. J. Murrow, H. Urkowitz, N. J. Bucci, and J. D. Nespor, "Range sidelobe suppression of expanded/compressed pulses with droop," in *Proc. of the National Radar Conference*. IEEE, 1994, pp. 116–122.

[5] D. Bailey and R. Hodgson, "Range filters: Local-intensity subrange filters and their properties," *Image and Vision Computing*, vol. 3, no. 3, pp. 99–110, 1985.

[6] R. M. Banta, L. D. Olivier, E. T. Holloway, R. A. Kropfli, R. W. Bartram, R. E. Cupp, and M. J. Post, "Smoke-column observations from two forest fires using Doppler lidar and Doppler radar," *Journal of Applied Meteorology*, vol. 31, pp. 1328–1349, November 1992.

[7] A. S. Barry, "Terminal doppler weather radar (TDWR) coverage of satellite airports," in *Proc. of the Digital Avionics Systems Conference (DASC)*, vol. 2. IEEE, 2000, pp. 7B3–1.

[8] T. Baum, L. Thompson, and K. Ghorbani, "A complex dielectric mixing law model for forest fire ash particulates," *IEEE Geosci. Remote Sens. Lett.*, vol. 9, no. 5, pp. 832–835, 2012.

[9] N. Bharadwaj and V. Chandrasekar, "Waveform design for CASA x-band radars," in *Proc. AMS 36th Conference on Radar Meteorology*. American Meteorological Society, 2005.

[10] ——, "Frequency diversity wideband waveforms for dual-polarization weather radars," in *Proc. AMS 34th Conference on Radar Meteorology*. American Meteorological Society, 2009.

[11] E. Billam, "Parameter optimisation in phased array radar," in *Radar 92, International Conference*. IET, 1992, pp. 34–37.

[12] R. Birch, "Radar observations of smoke," *Australian Meteorological and Oceanographic Journal*, pp. 30–31, 1968.

[13] S. Blackman and R. Popoli, *Design and Analysis of Modern Tracking Systems*, ser. Artech House radar library. Artech House, 1999.

[14] W. D. Blair, "Design of nearly constant velocity track filters for tracking maneuvering targets," in *Information Fusion, 2008 11th International Conference on*. IEEE, 2008, pp. 1–7.

[15] V. Bringi and V. Chandrasekar, *Polarimetric Doppler Weather Radar: Principles and Applications*. Cambridge University Press, 2001.

[16] E. Brookner, *Tracking and Kalman filtering made easy*, ser. A Wiley-Interscience publication. Wiley, 1998.

[17] J. Brotzge, K. Hondl, B. Philips, L. Lemon, E. Bass, D. Rude, and D. Andra Jr, "Evaluation of distributed collaborative adaptive sensing for detection of low-level circulations and implications for severe weather warning operations," *Weather and Forecasting*, vol. 25, no. 1, pp. 173–189, 2010.

[18] D. Brunkow, V. Bringi, P. C. Kennedy, S. A. Rutledge, V. Chandrasekar, E. Mueller, and R. K. Bowie, "A description of the CSU-CHILL national radar facility," *Journal of Atmospheric and Oceanic Technology*, vol. 17, no. 12, pp. 1596–1608, 2000.

[19] V. Chandrasekar, D. McLaughlin, J. Brotzge, M. Zink, B. Philips, and Y. Wang, "Distributed collaborative adaptive radar network: Preliminary results from the CASA IP1 testbed," in *Radar Conference (RadarCon), 2008 IEEE*. IEEE, 2008, pp. 1–5.

[20] ——, "Evaluation of distributed collaborative adaptive sensing in a four-node radar network: Integrated project 1," in *Geoscience and Remote Sensing Symposium (IGARSS), 2008 IEEE International*, vol. 5. IEEE, 2008, pp. V–148.

[21] V. Chandrasekar, D. McLaughlin, M. Zink, J. Brotzge, B. Philips, Y. Wang, S. Lim, F. Junyent, N. Bharadwaj, E. Lyons *et al.*, "The CASA IP1 test-bed after 5 years operation: Accomplishments, breakthroughs, challenges and lessons learned," in *Proc. of the 6th European Conf. on Radar in Meteorology and Hydrology (ERAD)*, 2010.

[22] V. Chandrasekar, Y. Wang, S. Lim, F. Junyent, N. Bharadwaj, D. McLaughlin, B. Philips, M. Zink, E. Lyons, D. Westbrook *et al.*, "Accomplishments, challenges and opportunities in developing network based radar systems for high-impact small-scale weather events," in *Radar Conference (RadarCon), 2011 IEEE*. IEEE, 2011, pp. 1056–1061.

[23] V. Chandrasekar, R. Keränen, S. Lim, and D. Moisseev, "Recent advances in classification of observations from dual polarization weather radars," *Atmospheric Research*, vol. 119, pp. 97–111, 2013.

[24] K.-C. Chang, "Multitarget tracking with adaptive detection thresholds," *IEEE Trans. Aerosp. Electron. Syst.*, vol. 32, no. 1, pp. 401–406, 1996.

[25] H. Chen and V. Chandrasekar, "High resolution rainfall mapping in the dallas-fort worth urban demonstration network," in *Geoscience and Remote Sensing Symposium (IGARSS), 2012 IEEE International*. IEEE, 2012, pp. 1936–1939.

[26] ——, "High resolution rainfall mapping with a regional network of polarimetric radars at s-and x-band frequencies," in *Proc. of the 31st General Assembly and Scientific Symposium (URSI-GASS)*. IEEE, 2014, pp. 1–4.

[27] J. Y. Cho, "Multi-PRI signal processing for the terminal Doppler weather radar. part II: Range-velocity ambiguity mitigation," *Journal of Atmospheric and Oceanic Technology*, vol. 22, no. 10, pp. 1507–1519, 2005.

[28] J. Cho, "Signal processing algorithms for the terminal Doppler weather radar: Build 2," Massachusetts Institute of Technology: Lincoln Laboratory, Tech. Rep. ATC-363, Febrary 2010.

[29] S. Choudhury and N. Bharadwaj, "Computer simulation of weather radar signals," *Department of Electrical & Computer Engineering, Colorado University*, pp. 1–6, 2002.

[30] D. o. E. Committee on Weather Radar Technology Beyond NEXRAD, National Research Council, B. o. A. S. Life Studies, and Climate, *Weather Radar Technology Beyond NEXRAD*. National Academies Press, 2002.

[31] S. Creaney and I. Kostarnov, "Designing efficient digital up and down converters for narrowband systems," Xilinx, Tech. Rep., 2008.

[32] S. T. Cummings and K. Behar, "Radar resource management for mechanically rotated, electronically scanned phased array radars," in *Radar Conference (RadarCon), 1991 IEEE*. IEEE, 1991, pp. 88–92.

[33] C. D. Curtis, "Exploring the capabilities of the agile beam phased array weather radar," Ph.D. dissertation, The University of Oklahoma, 2009.

[34] M. DeGarmo and G. M. Nelson, "Prospective unmanned aerial vehicle operations in the future national airspace system," in *Proc. of the 4th Aviation Technology, Integration and Operations (ATIO) Forum*. American Institute of Aeronautics and Astronautics, 2004, pp. 20–23.

[35] A. S. F. Division, "Yarnell hill fire: Serious accident investigation report," Arizona State Forestry Division, Tech. Rep., September 2013.

[36] P. Doherty and P. Rudol, "A UAV search and rescue scenario with human body detection and geolocalization," in *Advances in Artificial Intelligence*. Springer, 2007, pp. 1–13.

[37] R. Doviak and D. Zrnić, *Doppler Radar And Weather Observations*. Dover Publications, 1993.

[38] P. R. Drake, D. J. McLaughlin, and C. McCarroll, "Requirements, architecture, and technology for nextgen surveillance and weather radar capability (NSWRC)," in *Integrated Communications, Navigation and Surveillance Conference (ICNS)*. IEEE, 2012, pp. 1–19.

[39] M. Ettus, "USRP user's and developer's guide," *Ettus Research LLC*, 2005.

[40] N. O. S. Facility, "NEXRAD system specification," Tech. Rep. 2810000A, September 1996.

[41] J. A. G. for Phased Array Radar Project (JAG/PARP), "Federal research and development needs and priorities for phased array radar," Office of the Federal Coordinator for Meteorological Services and Supporting Research (OFCM), Tech. Rep. FCM-R25-2006, June 2006.

[42] J. M. Forthofer and S. L. Goodrick, "Review of vortices in wildland fire," *Journal of Combustion*, vol. 2011, 2011.

[43] C. Frush, R. Doviak, M. Sachidananda, and D. Zrnić, "Application of the SZ phase code to mitigate range-velocity ambiguities in weather radars," *Journal of Atmospheric and Oceanic Technology*, vol. 19, no. 4, pp. 413–430, 2002.

[44] G. Galati and G. Pavan, "Design criteria for a multifunction phased array radar integrating weather and air traffic control surveillance," in *Proc. European Radar Conference (EuRAD 2009)*. IEEE, 2009, pp. 294–297.

[45] M. Galletti and D. S. Zrnic, "Bias in copolar correlation coefficient caused by antenna radiation patterns," *IEEE Trans. Geosci. Remote Sens.*, vol. 49, no. 6, pp. 2274–2280, 2011.

[46] K. Ghorbani, T. C. Baum, and L. Thompson, "Properties and radar cross-section of forest fire ash particles at millimeter wave," in *The 42nd European Microwave Conference (EuMC'12)*, 2012, pp. 1335–1338.

[47] S. Giangrande, A. Ryzhkov, V. Melnikov, and J. Krause, "Calibration of the polarimetric NEXRAD radar using meteorological signals," in *Proc. AMS 11th Conf. on Aviation, Range, and Aerospace Meteorology*, vol. 5. American Meteorological Society, 2004.

[48] J. D. Gibbons and S. Chakraborti, *Nonparametric statistical inference*. Springer, 2011.

[49] K. Golestani, T. Chandrasekar, and R. J. Keeler, "Dual polarized staggered PRT scheme for weather radars: Analysis and applications," *IEEE Trans. Geosci. Remote Sens.*, vol. 33, no. 2, pp. 239–246, 1995.

[50] Google, "Google UAS airspace system overview," in *Proc. of the NASA Unmanned Aerial Systems (UAS) Traffic Management Convention.* NASA, July 2015.

[51] R. Gorte, "The rising cost of wildfire protection," Headwaters Economics, Tech. Rep., 2013.

[52] J. J. Gourley, P. Tabary, and J. Parent du Chatelet, "A fuzzy logic algorithm for the separation of precipitating from nonprecipitating echoes using polarimetric radar observations," *Journal of Atmospheric and Oceanic Technology*, vol. 24, no. 8, pp. 1439–1451, 2007.

[53] S. Haykin, "Cognitive radar: a way of the future," *IEEE Signal Process. Mag.*, vol. 23, no. 1, pp. 30–40, 2006.

[54] F. A. Heinsch and P. L. Andrews, *BehavePlus fire modeling system, version 5.0: design and features.* US Department of Agriculture, Forest Service, Rocky Mountain Research Station, 2010.

[55] R. Hodgson, D. Bailey, M. Naylor, A. Ng, and S. McNeill, "Properties, implementations and applications of rank filters," *Image and Vision Computing*, vol. 3, no. 1, pp. 3–14, 1985.

[56] A. P. Hopf, J. L. Salazar, R. Medina, V. Venkatesh, E. J. Knapp, S. J. Frasier, and D. J. McLaughlin, "CASA phased array radar system description, simulation and products," in *Geoscience and Remote Sensing Symposium (IGARSS), 2009 IEEE International*, vol. 2. IEEE, 2009, pp. II–968.

[57] A. P. Hopf, J. Bourgeois, P. Drake, and T. J. Flynn, "Raytheon polarimetric x-band phased array radar: Single and netted radar system," in *Proc. AMS 31st Conference on Environmental Information Processing Technologies.* American Meteorological Society, 2015.

[58] J. Hubbert, M. Dixon, and S. Ellis, "Weather radar ground clutter. part II: Real-time identification and filtering," *Journal of Atmospheric and Oceanic Technology*, vol. 26, no. 7, pp. 1181–1197, 2009.

[59] M. D. Hudlow, R. K. Farnsworth, and P. R. Ahnert, *NEXRAD technical requirements for precipitation estimation and accompanying economic benefits.* US Department of Commerce, National Oceanic and Atmospheric Administration, National Weather Service, Office of Hydrology, Hydrologic Research Laboratory, 1985.

[60] D. P. Hynek, "TDWR scan strategy implementation," MIT Lincoln Laboratory, Tech. Rep. ATC-222, September 1994.

[61] I. R. Ivic, D. Zrnić, and T.-Y. Yu, "The use of coherency to improve signal detection in dual-polarization weather radars," *Journal of Atmospheric and Oceanic Technology*, vol. 26, no. 11, pp. 2474–2487, 2009.

[62] T. Jeffrey, *Phased-Array Radar Design - Application of Radar Fundamentals*. SciTech Publishing, 2009.

[63] J. Johnson, P. L. MacKeen, A. Witt, E. D. W. Mitchell, G. J. Stumpf, M. D. Eilts, and K. W. Thomas, "The storm cell identification and tracking algorithm: An enhanced WSR-88D algorithm," *Weather and Forecasting*, vol. 13, no. 2, pp. 263–276, 1998.

[64] R. C. Johnson, H. A. Ecker, and J. S. Hollis, "Determination of far-field antenna patterns from near-field measurements," *Proc. IEEE*, vol. 61, no. 12, pp. 1668–1694, 1973.

[65] T. Jones and S. A. Christopher, "Satellite and radar remote sensing of southern plains grass fires: a case study," *Journal of Applied Meteorology and Climatology*, vol. 49, no. 10, pp. 2133–2146, October 2010.

[66] J. Keeley, W. Bond, R. Bradstock, J. Pausas, and P. Rundel, *Fire in Mediterranean Ecosystems: Ecology, Evolution and Management*. Cambridge University Press, 2011.

[67] P. H. Kopardekar, "Safely enabling UAS operations in low-altitude airspace," in *Proc. of the NASA Unmanned Aerial Systems (UAS) Traffic Management Convention*. NASA, July 2015.

[68] L. G. Lavdas *et al.*, "Program VSMOKE–users manual," 1996.

[69] A. Leon-Garcia, *Probability and Random Processes for Electrical Engineering*, ser. Addison-Wesley series in electrical and computer engineering. Addison-Wesley, 1994.

[70] L. Liu, V. N. Bringi, V. Chandrasekar, E. A. Mueller, and A. Mudukutore, "Analysis of the copolar correlation coefficient between horizontal and vertical polarizations," *Journal of Atmospheric and Oceanic Technology*, vol. 11, no. 4, pp. 950–963, 1994.

[71] A. Ludwig, "The definition of cross polarization," *IEEE Trans. Antennas Propag.*, vol. 21, no. 1, pp. 116–119, 1973.

[72] P. C. Mahalanobis, "On the generalized distance in statistics," *Proceedings of the National Institute of Sciences (Calcutta)*, vol. 2, pp. 49–55, 1936.

[73] D. McLaughlin, D. Pepyne, B. Philips, J. Kurose, M. Zink, D. Westbrook, E. Lyons, E. Knapp, A. Hopf, A. Defonzo, R. Contreras, T. Djaferis, E. Insanic, S. Frasier, V. Chandrasekar, F. Junyent, N. Bharadwaj, Y. Wang, Y. Liu, B. Dolan, K. Droegemeier, J. Brotzge, M. Xue, K. Kloesel, K. Brewster, F. Carr, S. Cruz-Pol, K. Hondl, and P. Kollias, "Short-wavelength technology and the potential for distributed networks of small radar systems," *Bulletin of the American Meteorological Society*, vol. 90, no. 12, pp. 1797–1817, December 2009.

[74] D. J. McLaughlin, E. Knapp, Y. Wang, and V. Chandrasekar, "Distributed weather radar using x-band active arrays," in *Radar Conference (RadarCon), 2007 IEEE*. IEEE, 2007, pp. 23–27.

[75] V. Melnikov, D. Zrnic, R. Rabin, B. Pierce, and P. Zhang, "Radar polarimetric signatures of fire plumes," in *Proc. AMS 25th Conference on International Interactive Information and Processing Systems*. American Meteorological Society, 2009.

[76] V. M. Melnikov and D. Zrnić, "On the alternate transmission mode for polarimetric phased array weather radar," *Journal of Atmospheric and Oceanic Technology*, vol. 32, no. 2, 2014.

[77] V. Melnikov and D. Zrnić, "Simultaneous transmission mode for the polarimetric WSR-88D: Statistical biases and standard deviations of polarimetric variables," *NOAA/NSSL Rep*, pp. 1–84, 2004.

[78] W. L. Melvin and J. A. Scheer, *Review of Tracking Concepts*. Institution of Engineering and Technology, 2013, ch. 15, pp. 671–674.

[79] J. T. Morisette, L. Giglio, I. Csiszar, A. Setzer, W. Schroeder, D. Morton, and C. O. Justice, "Validation of MODIS active fire detection products derived from two algorithms," *Earth Interactions*, vol. 9, no. 9, pp. 1–25, 2005.

[80] N. R. C. U. C. on Developing Mesoscale Meteorological Observational Capabilities to Meet Multiple National Needs, *Observing Weather and Climate from the Ground Up: A Nationwide Network of Networks*. National Academies Press, 2009".

[81] K. Orzel, "X-band dual polarization phased-array radar for meteorological applications," Ph.D. dissertation, University of Massachusetts Amherst, 2015.

[82] K. Orzel, V. Venkatesh, R. Palumbo, R. Medina, J. Salazar, A. Krishnamurthy, E. Knapp, D. McLaughlin, R. Tessier, and S. Frasier, "Mobile x-band dual polarization phased array radar: System requirements and development," in *Proc. AMS 34th Conference on Radar Meteorology*, 2011.

[83] K. Orzel, V. Venkatesh, T. Hartley, and S. Frasier, "Development and calibration of a x-band dual polarization phased array radar," in *Radar Conference (RadarCon), 2013 IEEE*. IEEE, 2013, pp. 1–4.

[84] R. Palumbo, E. Knapp, K. Wood, D. J. McLaughlin, C. McCarroll, and S. J. Frasier, "Phase-tilt weather radar: Calibration and preliminary results," in *Radar Conference (RadarCon), 2013 IEEE*. IEEE, 2013, pp. 429–433.

[85] R. A. Palumbo, E. Knapp, K. Wood, D. J. McLaughlin, and R. Palumbo, "Deployment considerations and hardware technologies for realizing x-band radar networks," in *Seventh European Conf. on Radar in Meteorology and Hydrology (ERAD 2012)*, 2012.

[86] R. A. Palumbo, W. A. Al-Ashwal, B. Ferguson, C. McCarroll, and D. J. McLaughlin, "Weather and bushfire observation using low cost x-band phased array radars," in *Radar Conference (RadarCon), 2013 IEEE*. IEEE, 2013, pp. 309–314.

[87] R. A. Palumbo, E. J. Knapp, D. J. McLaughlin, W. A. Al-Ashwal, D. Gray, B. Ferguson, and C. McCarroll, "Polarimetric observations of prescribed bushfires in south australia using an x-band phased array radar," in *Proc. AMS 36th Conference on Radar Meteorology*. American Meteorological Society, 2013.

[88] H. S. Park, A. Ryzhkov, D. Zrnić, and K.-E. Kim, "The hydrometeor classification algorithm for the polarimetric WSR-88D: Description and application to an MCS," *Weather and Forecasting*, vol. 24, no. 3, pp. 730–748, 2009.

[89] E. Parzen, "An approach to empirical time series analysis," *Radio Science*, vol. 68, no. 9, pp. 937–951, 1964.

[90] A. L. Pazmany, J. B. Mead, H. B. Bluestein, J. C. Snyder, and J. B. Houser, "A mobile rapid-scanning x-band polarimetric (raxpol) Doppler radar system," *Journal of Atmospheric and Oceanic Technology*, vol. 30, no. 7, pp. 1398–1413, 2013.

[91] D. Pepyne, J. Trabal, F. Lok, P. Drake, T. J. Flynn, J. Clark, and A. P. Hopf, "Raytheon x-band polarimetric phased-array radar: Weather data processing, first look," in *Proc. AMS 31st Conference on Environmental Information Processing Technologies*. American Meteorological Society, 2015.

[92] B. Philips and V. Chandrasekar, "The dallas fort worth urban remote sensing network," in *Geoscience and Remote Sensing Symposium (IGARSS), 2012 IEEE International*. IEEE, 2012, pp. 6911–6913.

[93] W. H. Press, S. A. Teukolsky, W. T. Vetterling, and B. P. Flannery, *Numerical recipes in C*. Cambridge university press Cambridge, 1996, vol. 2.

[94] L. F. Radke, D. A. Hegg, P. V. Hobbs, J. D. Nance, J. H. Lyons, K. K. Laursen, R. E. Weiss, P. J. Riggan, and D. E. Ward, "Particulate and trace gas emissions from large biomass fires in north america," *Global Biomass Burning: Atmospheric Climatic and Biospheric Implications*, pp. 209–224, 1991.

[95] F. D. R. Rep. Lucas, "Weather research and forecasting innovation act of 2015," House - Science, Space, and Technology | Senate - Commerce, Science, and Transportation, Tech. Rep. HR1561, 2015.

[96] R. Rew and G. Davis, "NetCDF: an interface for scientific data access," *IEEE Comput. Graph. Appl.*, vol. 10, no. 4, pp. 76–82, 1990.

[97] M. Richards, *Fundamentals of Radar Signal Processing*, ser. Professional Engineering. Mcgraw-Hill, 2005.

[98] M. A. Richards, J. A. Scheer, and W. A. Holm, *Radar Tracking Algorithms*. SciTech Publishing, 2010, vol. 1, ch. 19.

[99] M. A. Richards, J. Scheer, W. A. Holm *et al.*, *Threshold Detection of Radar Targets*. SciTech Publishing, 2010, vol. 1, ch. 15.

[100] M. Sachidananda and D. Zrnić, "Efficient processing of alternately polarized radar signals," *Journal of Atmospheric and Oceanic Technology*, vol. 6, no. 1, pp. 173–181, 1989.

[101] J. L. Salazar, R. Medina, E. J. Knapp, and D. J. McLaughlin, "Phase-tilt array antenna design for dense distributed radar networks for weather sensing," in *Geoscience and Remote Sensing Symposium (IGARSS), 2008 IEEE International*, vol. 5. IEEE, 2008, pp. V–318.

[102] L. Sankey, *FRF-166 User's Guide*, 3rd ed., FIRST RF Corporation, Boulder, CO, December 2012.

[103] J. D. Scargle, "Studies in astronomical time series analysis. III-fourier transforms, autocorrelation functions, and cross-correlation functions of unevenly spaced data," *The Astrophysical Journal*, vol. 343, pp. 874–887, 1989.

[104] U. F. Service, "The rising cost of fire operations: Effects on the forest service's non-fire work," US Forest Service, Tech. Rep., August 2014.

[105] ——, "Federal firefighting costs (suppression only)," National Interagency Fire Center, Tech. Rep., 2015.

[106] M. Sestak and A. Riebau, *SASEM: Simple Approach Smoke Estimation Model*. United States Department of the Interior, 1988.

[107] A. Siggia and R. Passarelli Jr, "Gaussian model adaptive processing (GMAP) for improved ground clutter cancellation and moment calculation," in *Proc. of the 2nd European Conf. on Radar in Meteorology and Hydrology (ERAD)*, vol. 2, 2004, pp. 421–424.

[108] M. Skolnik, *Radar Handbook*, ser. Electronics electrical engineering. McGraw-Hill, 2008.

[109] S. M. Sowelam and A. H. Tewfik, "Waveform selection in radar target classification," *IEEE Trans. Inf. Theory*, vol. 46, no. 3, pp. 1014–1029, 2000.

[110] N. Surveillance and W. R. Capability, "Multifunction phased array radar (MPAR) notional functional requirements document," Federal Aviation Administration, Tech. Rep. 2.2, April 2013.

[111] J. Taylor Jr and G. Brunins, "Design of a new airport surveillance radar (ASR-9)," *Proc. IEEE*, vol. 73, no. 2, pp. 284–289, 1985.

[112] S. M. Torres and C. Curtis, "New weather-surveillance capabilities for NSSL's phased-array radar," in *Proc. AMS 32nd Conference on Radar Meteorology*. American Meteorological Society, 2013.

[113] S. M. Torres, Y. F. Dubel, and D. Zrnić, "Design, implementation, and demonstration of a staggered prt algorithm for the WSR-88D," *Journal of Atmospheric and Oceanic Technology*, vol. 21, no. 9, pp. 1389–1399, 2004.

[114] D. B. Turner, *Workbook of atmospheric dispersion estimates*. US Government Printing Office, 1973.

[115] J. Wang, E. Brookner, P. Cornwell, M. Gerecke, and J. Farr, "Modernization of en route air surveillance radar," *IEEE Trans. Aerosp. Electron. Syst.*, vol. 48, no. 1, pp. 103–115, 2012.

[116] Y. Wang and V. Chandrasekar, "Algorithm for estimation of the specific differential phase," *Journal of Atmospheric and Oceanic Technology*, vol. 26, no. 12, pp. 2565–2578, 2009.

[117] ——, "Polarization isolation requirements for linear dual-polarization weather radar in simultaneous transmission mode of operation," *IEEE Trans. Geosci. Remote Sens.*, vol. 44, no. 8, pp. 2019–2028, 2006.

[118] C. A. Wolff, M. Bell, and W. Lee, "Automatic quality control of airborne Doppler radar data," in *Proc. AMS 36th Conference on Radar Meteorology*, vol. 9. American Meteorological Society, 2009.

[119] T.-Y. Yu, M. B. Orescanin, C. D. Curtis, D. S. Zrnic, and D. E. Forsyth, "Beam multiplexing using the phased-array weather radar," *Journal of Atmospheric and Oceanic Technology*, vol. 24, no. 4, pp. 616–626, 2007.

[120] A. Zahrai and D. Zrnić, "Implementation of polarimetric capability for the wsr-88d (nexrad) radar," in *Proc. of the National Aerospace and Electronics Conference (NAECON)*, vol. 1. IEEE, 1997, pp. 346–352.

[121] M. Zink, E. Lyons, D. Westbrook, J. Kurose, and D. L. Pepyne, "Closed-loop architecture for distributed collaborative adaptive sensing of the atmosphere: meteorological command and control," *International Journal of Sensor Networks*, vol. 7, no. 1-2, pp. 4–18, 2010.

[122] D. Zrnic, V. Melnikov, and R. Doviak, "Issues and challenges for polarimetric measurement of weather with an agile beam phased array radar," *NOAA/NSSL Report*, 2012.

[123] D. Zrnic, V. Melnikov, R. Doviak, and R. Palmer, "Scanning strategy for the multifunction phased-array radar to satisfy aviation and meteorological needs," *IEEE Geosci. Remote Sens. Lett.*, vol. 12, no. 6, pp. 1204–1208, 2015.